Refractive devices for acoustical and flexual waves

ALFONSO CLIMENTE ALARCÓN

EDITORIAL
UNIVERSITAT POLITÈCNICA DE VALÈNCIA

UNIVERSITAT POLITÈCNICA DE VALÈNCIA

Departamento de Ingeniería Electrónica

Refractive Devices for Acoustical and Flexural Waves

Por Alfonso Climente Alarcón

Dirigida por
José Sánchez-Dehesa Moreno-Cid
Daniel Torrent Martí

May 29, 2015

Collection Doctoral Thesis

Telf.: 963 877 012 / www.lalibreria.upv.es

ISBN: 978-84-9048-326-8 (printed version)

Este manuscrito de tesis ha sido valorado y calificado Excelente por el siguiente tribunal de evaluación:

1. Dr. Wim Desmet
   Full Professor
   Department of Mechanical Engineering
   KU Leuven - Belgium

2. Dr. Massimo Ruzzene
   Full Professor
   Department of Mechanical Engineering
   Georgia Institute of Technology - USA

3. Dr. Gengkai Hu
   Full Professor and Dean
   School of Aerospace Engineering
   Beijing Institute of Technology - China

En Valencia, a 24 de Enero de 2015

Esta tesis ha sido valorada y calificada Cum Laude por el siguiente tribunal de defensa:

1. Dr. Wim Desmet
   Full Professor
   Department of Mechanical Engineering
   KU Leuven - Belgium

2. Dr. Vicente Romero García
   Junior Researcher
   Laboratoire d'Acoustique de l'Université du Maine
   Centre National de Recherche Scientifique - France

3. Dr. Yolanda Jimenez Jimenez
   Profesor Titular de Universidad
   Departamento de Ingeniería Electrónica
   Universitat Politèctica de Vàlencia - Spain

En Valencia, a 20 de Febrero de 2015

I would like to acknowledge the PhD grant provided by the U.S.A Office of Naval Research under Contract No. N000141210216

and the financial support by the Spanish MINECO under Contract No. TEC 2010-19751

Agradecimientos

En primer lugar me gustaría agradecer a mis directores de tesis, José Sánchez-Dehesa y Daniel Torrent Martí, todo el esfuerzo, paciencia y dedicación que han invertido en enseñarme, guiarme por el camino de la investigación y ayudarme en el desarrollo de la tesis doctoral. Sin duda, sin ellos este trabajo no habría sido posible.

Gracias a mis compañeros de trabajo Victor García, Rogelio Gracía y Ana Díaz, así como al resto de los miembros del GFO, Francisco Cervera, Hector García, Jorge Carbonell, Matthew Guild, Edgar Reyes y WeiWei Kan. Gracias por las incontables conversaciones delante de un pizarra o yendo a comer que me ayudaron sobre tantos y tantos temas.

Gracias a Andrew Norris por acogerme en su grupo durante la estancia, y por todo lo que me enseñó durante ese periodo. También quiero agradecer a Alexey Titovich, XiaoShi Su y Adam Nagy, como me hicieron sentir como uno más desde el mismo momento que llegue a Nueva Jersey.

A nivel personal, quiero agradecer especialmente a mis padres todo el cariño y el apoyo durante toda mi carrera académica. Han estado allí en todo momento, no solo para guiarme, sino también para levantarme cuando era necesario. Nunca podré agradecerles el esfuerzo que han hecho por mí. De igual manera, quiero agradecer a mis hermanos, Vicente y Ana, todo lo que me han enseñado. Como dice un proverbio japonés, un hombre crece mirando la espalda del que tiene delante, y no he podido tener mejor ejemplo a seguir.

No pueden faltar tampoco los agradecimientos a mis amigos Meli, Diego y Javi. Todos los incontables momentos que hemos pasado juntos han hecho surgir anécdotas que recordaremos alegremente a lo largo de nuestras vidas. Esas incontables charlas hasta las tantas no tienen precio, gracias. También quiero agradecer a Flavio y Néstor el haberme guiado, desde la experiencia, por el camino de la investigación. Vuestros consejos fueron muy útiles.

Y, por su puesto, gracias a Clara, a quien va dedicada esta tesis. Desde que nos conocimos, ella ha sido para mi lo que me ha impulsado

a continuar cada día. Empezaste siendo mi mejor amiga, te convertiste en mi novia y, finalmente, en mi mujer. Por todos los momentos en los que decaía y tú estabas allí. Muchas gracias por todo.

A Clara

Resumen de la tesis doctoral

Dispositivos refractivos para ondas acústicas y flexurales

de

Alfonso Climente Alarcón
Doctor en Ciencias por el Departamento de Ingeniería Electrónica
Universitat Politècnica de València, Valencia, Diciembre 2014

El objetivo de esta tesis doctoral ha sido el diseño y demostración de dispositivos refractivos, no sólo para las ondas acústicas, sino también para ondas flexurales en placas delgadas.

Matemáticamente estos problemas han sido tratados por medio de la teoría de la dispersión mltiple. Esta teoría es adecuada para los casos aquí tratados ya que las geometrías de los problemas son principalmente circulares. En este manuscrito, describimos la teoría de dispersión múltiple ya empleada en trabajos anteriores. Asimismo, desarrollamos un análogo de la teoría para ondas flexurales en sistemas multicapa. El algoritmo queda aquí detallado y ha sido utilizado con éxito para simular numéricamente el comportamiento de distintos dispositivos. Por lo tanto, este manuscrito está divido en dos partes.

La primera parte se centra en dos dispositivos acsticos refractivos: una lente de índice de gradiente y un absorbente acústico omnidireccional de banda ancha, o " agujero negro acústico ". Ambos se basan en cristales sónicos compuestos de cilindros rígidos sumergidos en aire. Como establece el método de homogeneización, el índice de refracción deseado puede obtenerse mediante la variación de los radios de los cilindros. Una vez diseñados los dispositivos, se llevaron a cabo simulaciones numéricas y mediciones para probar el comportamiento de cada uno de ellos. Para este propósito, se desarrollaron dos sistemas de medición específicos, la cámara bidimensional y la cámara de impedancias, ambas

quedan explicadas en detalle en esta tesis.

La segunda parte describe el diseño de dispositivos refractivos para ondas flexurales. En lugar de usar "cristales platónicos", se ha hecho uso de la relación de dispersión peculiar de este tipo de ondas. Como establece la ecuación de propagación, la velocidad de onda se ve modificada, no sólo por las propiedades elásticas de la placa, sino también por su espesor. El uso de este último enfoque nos ha permitido simular numéricamente una serie de lentes de gradiente de índice radialmente simétricas ya conocidas en la literatura. Asimismo, se ha diseñado un dispositivo omnidireccional de banda ancha para aislar de las ondas flexurales una región de una placa delgada. Costa de una región anular con un perfil de espesor que imita la combinación de un potencial atractivo y otro repulsivo. Las ondas se concentran en su parte inferior y se disipan por medio de una capa absorbente colocada sobre la placa. Tras presentar simulaciones numéricas, los resultados son discutidos.

Por último, presentamos un resonador en el plano para ondas flexurales consistente en un agujero atravesado por una varilla rectangular. Para resolver el problema, se acoplan las ecuaciones de movimiento de Kirchhoff-Love y Euler-Bernoulli, y se introduce una forma compacta de la matriz de transferencia. Para demostrar su validez, las simulaciones numéricas obtenidas mediante este algoritmo son contrastadas contra un simulador comercial basado en elementos finitos.

Resum de la tesi doctoral

Dispositius refractius per a ones acústiques i flexurales

de

Alfonso Climente Alarcón
Doctor en Ciències pel Departament d'Enginyeria Electrònica
Universitat Politècnica de València, Decembre 2014

L'objectiu d'aquesta tesi doctoral ha estat el disseny i demostració de dispositius refractius, no només per les ones acústiques, sinó també per ones flexurales en plaques primes.

Matemàticament aquests problemes han estat tractats per mitjà de la teoria de la dispersió múltiple. Aquesta teoria és adequada per als casos aquí tractats ja que les geometries dels problemes són principalment circulars. En aquest manuscrit, descrivim la teoria de dispersió múltiple ja emprada en treballs anteriors. Així mateix, desenvolupem un anàleg de la teoria per ones flexurales en sistemes multicapa. L'algorisme queda aquí detallat i ha estat utilitzat amb èxit per simular numèricament el comportament de diferents dispositius. Per tant, aquest manuscrit està dividit en dues parts.

La primera part se centra en dos dispositius acústics refractius: una lent d'índex de gradient i un absorbent acústic omnidireccional de banda ampla, o "forat negre acústic". Tots dos es basen en cristalls sònics compostos de cilindres rígids submergits en aire. Com estableix el mètode d'homogeneïtzació, l'índex de refracció desitjat es pot obtenir mitjanant la variació dels radis dels cilindres. Un cop dissenyats els dispositius, es van dur a terme simulacions numèriques i mesuraments per provar el comportament de cada un d'ells. Per a aquest propòsit, es van desenvolupar dos sistemes de mesura específics, la càmera bidimensional i la càmera d'impedàncies, ambdues queden explicades en detall en aquesta

tesi.

La segona part descriu el disseny de dispositius refractius per ones flexurales. En lloc d'usar "vidres platònics", s'ha fet ús de la relació de dispersió peculiar d'aquest tipus d'ones. Com estableix l'equació de propagació, la velocitat d'ona es veu modificada, no noms per les propietats elàstiques de la placa, sinó tamb per la seva espessor. L'ús d'aquest últim enfocament ens ha permès simular numèricament una sèrie de lents de gradient d'índex radialment simètriques ja conegudes en la literatura. Així mateix, s'ha dissenyat un dispositiu omnidireccional de banda ampla per aïllar de les ones flexurales una regió d'una placa prima. Costa d'una regió anullar amb un perfil de gruix que imita la combinació d'un potencial atractiu i un altre repulsiu. Les ones es concentren a la part inferior i es dissipen per mitjà d'una capa absorbent collocada sobre la placa. Després de presentar simulacions numèriques, els resultats són discutits.

Finalment, presentem un ressonador en el pla per ones flexurales consistent en un forat travessat per una vareta rectangular. Per resoldre el problema, s'acoblen les equacions de moviment de Kirchhoff-Love i Euler-Bernoulli, i s'introdueix una forma compacta de la matriu de transferència. Per demostrar la seva validesa, les simulacions numèriques obtingudes mitjanant aquest algorisme són contrastades contra un simulador comercial basat en elements finits.

Abstract of the doctor thesis

Refractive devices for acoustical and flexural waves

by

Alfonso Climente Alarcón
Doctor of Science in the Ingeniería Electrónica department
Universitat Politècnica de València, Valencia, December 2014

The aim of this work has been the design and demonstration of refractive devices, not only for acoustic waves, but also for flexural waves in thin plates.

Mathematically these problems have been treated by means of the multiple scattering theory, because the geometries of the problems were mainly circular and such theory is the best one in these cases. The multiple scattering theory, previously stated, is here explained. Additionally, a multilayer scattering theory for flexural waves is here introduced and successfully used to numerically simulate their behavior. Therefore, this PhD thesis is divided in two parts.

The first part is devoted to describe two acoustic refractive devices: a gradient index lens and an omnidirectional broadband acoustic absorber, or "acoustic black hole". Both are based on sonic crystals consisting of of rigid cylinders immersed in a fluid background. As the homogenization method states, the desired refractive index can be obtained by tailoring the radii of the cylinders. Thereafter, numerical simulations and measurements were conducted to test the behavior of each device. For this purpose, two specific measuring systems were developed: the two-dimensional chamber and the impedance chamber. Both are here explained in detail.

The second part describes the design of refractive devices for flexural waves. Instead of using "platonic crystals", we made use of the pecu-

liar dispersion relationship of flexural waves. As the equation states, the wave speed is modified not only by the elastic properties of the plate, but also from its thickness. Using the latest approach a set of numerical simulations of known circularly symmetrical gradient index lenses have been performed. Additionally, an omnidirectional broadband insulating device for flexural waves has been designed. It consist of a well-like thickness profile in an annular region of the plate, that mimics the combination of an attractive and repulsive potentials. The waves are focused at its bottom and dissipated by means of an absorptive layer placed on top. Numerical simulations are here presented and discussed.

Finally, we present an in-plane flexural resonator, consisting of a hole in a thin plate traversed by a beam. Here, a closed form of the transfer matrix is obtained by coupling the Kirchhoff-Love and the Euler-Bernoulli motion equations. Numerical simulations, tested against a commercial finite element simulator, prove its efficiency.

Contents

List of Figures

List of Tables

Introduction

State of the Art

Music has been a part of every known culture, past and present. Since all people of the world, including the most isolated tribal groups, have a form of music, it may be concluded that music is likely to have been present in the ancestral population prior to the dispersal of humans around the world. Consequently music may have been with us for at least 50,000 years, varying widely between times and places. But, from a scientific point of view, music is a compilation of sound waves generated by the vibration of materials.

Since the time of Pythagoras, in the ancient Greek (6th century BC) the propagation of sound waves, and the reason explaining why some combinations of musical sounds seemed more beautiful than others has driven the research on acoustics. Later on, in about 20 BC, the Roman architect and engineer Vitruvius wrote a treatise on the acoustic properties of theaters including discussion of interference, echoes, and reverberation. Also Galileo Galilei, in the 16th century contributed to this field. But it was not until the 19th century where Lord Rayleigh combined, in his monumental work The Theory of Sound (1877), his own copious contributions to the field of acoustics with the work of another major figure of mathematical acoustics, Hermann von Helmholtz. One year later, in 1888, Augustus Edward Hough Love, using assumptions proposed by Gustav Kirchhoff, expanded the one-dimensional beam theory developed by Leonhard Euler and Daniel Bernoulli to create a two-dimensional mathematical model used to determine the stresses and deformations of thin plates. From that point on, the acoustics and vibrations fields saw an increasing number of research lines in the 20th century. In this manuscript we will focus on two main topics: acoustic and flexural metamaterials.

Acoustic metamaterials

Acoustic metamaterials were developed in parallel with the study of electromagnetic metamaterials introduced by John Pendry during the

90's [60]. The boost in the study of acoustic metamaterials began with the fabrication and demonstration of sonic crystals [67]. A sonic crystal consists of a periodic distribution of inclusions immersed in a fluid background. Commonly, these structures present, for frequencies of the order of the lattice separation, a band of frequencies (band gap) in which the sound propagation is forbidden because of Bragg reflection. For the case of two-dimensional (2D) sonic crystals (SC), this behavior has been already analyzed in a broad range of frequencies [67]. However, these 2D metamaterials usually gain special properties from structure rather than composition, using the inclusion of small inhomogeneities to enact effective macroscopic behavior [17, 42]. Therefore, in the range of low frequencies (homogenization limit) they behave like homogeneous media whose effective acoustic parameters, dynamical mass density, and bulk modulus, basically depend on the lattice filling fraction [32, 48, 74, 76].

The homogenization properties of sonic crystals have been employed to design refractive devices like, for example, acoustic lenses whose focusing properties are based on their external curved surfaces [11, 25, 49], flat surface lenses [3] or FabryPerot type acoustic interferometers [68]. Additionally, other type of flat lenses, like the gradient index ones (GRIN) have also been designed as sonic crystals (SC). Like their optical counterparts, the proposed 2D GRIN SC lenses have flat surfaces and are of easier fabrication than curved SC lenses. The propagation of sound through the medium is obtained by tuning the local refractive index of the lens. Theoretical demonstrations have been proposed were the index gradient was obtained by changing the SC filling fraction, which is directly related to the local refraction index, [77]; or by changing the material composition of the cylinder along the lens [39]. More recently, a GRIN SC lens based on a different approach has been proposed and experimentally demonstrated [61]; it is designed for a frequency within the first acoustic band with negative slope. This type of GRIN lenses, working with wavelengths of the order of the lattice parameter, tend to have a very small working bandwidth centered on the single operational frequency at which they have been designed. Experimental demonstrations

of acoustic lenses were then reported for airborne [90], and underwater [46] sound propagation.

Other interesting proposals with electromagnetic metamaterials have also influenced new research lines in acoustics. This is the case of the "optical black-hole" introduced by Narimanov and Kildishev [30, 52]. This work inspired several theoretical proposals for EM waves [21, 56, 81], as well as numerical realizations based on photonic crystals [40, 43] and an experimental demonstration [13,89]. Following these results with electromagnetic metamaterials, "acoustic black holes" based on sonic crystals were also theoretically proposed [38] with a performance similar to that for electromagnetic waves. Experimental results were then conducted for airborne sound [79] and underwater waves [51].

Flexural metamaterials

Elastic metamaterials have been a hot topic in the last years. However, in this work we focus on the propagation of flexural waves through thin plates [24, 37, 72]. One type of elastic metamaterials are the so called *platonic crystals*, which were developed also as the counterpart of electromagnetic metamaterials. They consist on periodic arrangements of scatterers or inclusions. The simplest form is obtained by drilling holes whose radii is changed according to a specific relationship hole radius-refractive index. The scattering by holes in plates has been analyzed [36, 50, 54, 59, 70] and the resulting band structures have been obtained [26, 27, 47]. Moreover, by introducing anisotropy in the system, more complicated structures were designed in order to obtain novel elastic devices [12, 53].

As in the case of sonic crystals, the control of the propagation of flexural waves by gradient index devices has been studied. Results were reported for positive [18, 82], negative [9, 19, 63] and double negative [41] refractive devices. These lenses also have proved to be useful for structural testing [20, 80]. Although the frequency response of the refractive devices described above is known to be broadband, the major drawback

is that a gradient index device requires a continuous variation of the refractive index, which obviously cannot be done with discrete lattices of holes, since the result will always be a stepped profile [71].

However, the local dependence of the elastic properties can also be obtained by means of thickness variation. Known as wedges, these structures produce a gradual reduction in the velocity of the wave by changing the plate's local thickness. This approach has been employed by Krylov and Tillman in 2004 [34]. It is based on the peculiar dispersion relationship of flexural waves, which depends not only on the material of the plate but also on its thickness, which is a parameter that can be easily controlled at almost every scale. The approach has been extensively applied to carry out experimental investigations to achieve efficient damping of flexural waves; first, at the edge of plates [55] and then at the plate center [22, 35] which consists of designed pits with a layer of absorbing materials attached in the middle. For more information on these topics, see Ref. [33].

In addition to the phenomena described above, embedding local resonances in a thin plate has expanded the control over the propagation of flexural waves. [87, 88]. The elastic properties were adjusted to open band gaps in regions associated with the frequency of the resonance, instead of opening in the wavelength region of the order of the structural period, were they usually generate.

The local resonances have been achieved by introducing surface "inclusions" on top of semi-infinite mediums [29] or thin plates, such as hollow spheres or cylinders [65], spring-masses [85, 86], simple pillars [62], composite pillars [57] or in-plane resonator [2]. Experiments have been reported proving the existence of tunable band gaps by using stubs [58,84] or piezoelectric shunts [10] on plates. Examples of potential applications of this local resonators range from vibration absorption [5] to an elastic analoge of graphene [75] or decreasing the vibrational response of panels [14,15]. For more information on this topic the reader is addressed to the reviews [28, 45, 83] and references therein.

Outline of the PhD manuscript

Apart from the introduction, the concluding remarks and the appendix, the manuscript is divided in two main parts. These cover the main topics of the PhD Thesis, sound waves and vibrations, and are likewise separated into many chapters.

Part I: Sound Waves Here we cover the refractive devices for acoustic waves. Next, the content of each chapter inside this part is detailed.

Chapter 1 presents the theoretical introduction needed to understand the next two chapters of this part. Here Helmholtz equation, Multiple Scattering theory and the Homogenization method are explained in detail among others. Other quantities used to analyze the results, as the acoustic intensity and the scattering cross section, are also explained.

Chapter 2 describes the design, implementation and measurement of a gradient index sonic lens. A ray model is developed from Fermat's principle to predict the position of the focal spot. The experimental setup, named as 2D chamber, is explained and, afterward, numerical simulations are compared against the experimental results.

Chapter 3 describes the design, implementation and measurement of an omnidirectional broadband acoustic black hole based on sonic crystals. Different absorbing materials are introduced and characterized in an impedance tube. These materials are later used as the absorbing core of the black hole. Finally, a metamaterial core based also on sonic crystals is designed to be the optimal absorber. The whole structure is measured in a new experimental setup, named as 2D impedance chamber, which is also explained in detail. Finally, the experimental results are given and fully analyzed.

Part II: Vibrations Here we cover the refractive devices for flexural waves. Next, the content of each chapter is detailed.

Chapter 1 presents the theoretical introduction needed to understand the next three chapters. Here the Euler-Bernoulli and the Kirchhoff-Love motion equations are derived. Furthermore, the multilayer scattering theory is explained in detail. Other quantities used to analyze the re-

sults, as the flexural energy flux and the scattering cross section, are also explained.

Chapter 2 describes the method to design any type of gradient index device in thin plate by tailoring the plate's thickness. Different lenses known in optics are numerically simulated and the results are presented. The broadband performance is analyzed by means of the scattering cross section.

Chapter 3 further extends the previous chapter by designing and implementing an omnidirectional broadband insulating device for flexural waves. The Ross-Kerwin-Ungar model is here explained and analyzed. Finally, numerical simulations of the insulating device are presented and discussed.

Chapter 4 describes the process to obtain the transfer matrix of a flexural resonator. The resonator consists of a hole in a thin plate crossed by a beam. The approach to obtain the transfer matrix is based on an analoge of the acoustic impedance method, also explained. Finally, finite element simulation are compared against the analytical model to test it.

Concluding Remarks Here the concluding remarks on each chapter of the PhD manuscript are given. Also, the future work is introduced and all the publications generated throughout this work are listed.

Appendix Finally, in the *Appendix*, Bessel's functions and their properties are given, paying attention to Graf's addition theorem. Additionally, the measurement method used in the impedance tube is explained.

Part I

Sound waves

Chapter 1

Theoretical introduction

In this chapter, the acoustic theory needed for the next chapter is introduced. Concepts like bulk modulus and mass density and the relationship they have with the speed of sound will be explained. Additionally, the Helmholtz equation is derived, an example of solution is given and the boundary conditions for different systems will be explained.

1.1 Fluid Physics

The systems researched throughout this work are comprised of two dimensional (2D) homogeneous isotropic materials and only linear wave phenomena are considered. Therefore, non-linear elements will be neglected.

1.1.1 Equation of motion

The equation of motion of a fluid describes how the pressure $P(\mathbf{r}, t)$ inside a differential volume located at $\mathbf{r}$ changes with time. The pressure P is defined as the amount of force F acting on a surface dA as

$$P = -\frac{dF}{dA} \tag{1.1.1}$$

where the minus sign comes from the fact that the force is acting on the surface and the pressure is reacting outwards. Let us consider that a pressure wave propagates through an homogeneous and isotropic fluid. Then, to obtain the equation of motion it's necessary to consider three equations previously, which are the force equilibrium, the mass conservation law and the state equation.

Force equilibrium

Figure 1.1 shows a differential element of dimensions $dx \times dy \times dz$ an mass dm on which forces F_{x_i} are acting on each of its faces. From the definition of pressure and Newton's second law we obtain

$$\sum F_x = -\frac{\partial P}{\partial x} dV = a_x dm, \tag{1.1.2}$$

$$\sum F_y = -\frac{\partial P}{\partial y} dV = a_y dm, \tag{1.1.3}$$

$$\sum F_z = -\frac{\partial P}{\partial z} dV = a_z dm, \tag{1.1.4}$$

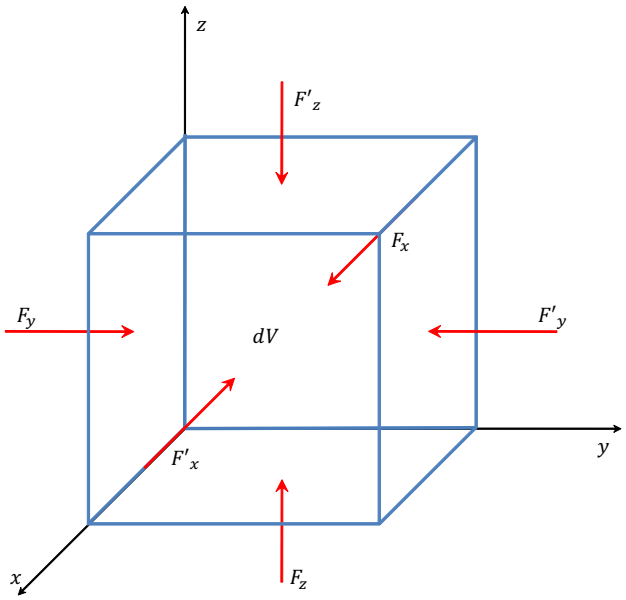

Figure 1.1: Differential element of a fluid with forces acting perpendicular to each face of the volume dV.

where a_{x_i} is the acceleration in the x_i-direction. Taking into account the definition of mass density $\rho = dm/dV$ both the three equations can be combined as

$$-\nabla P = \rho a = \rho \frac{\partial \mathbf{v}}{\partial t}, \tag{1.1.5}$$

being $\mathbf{v} = d\mathbf{r}/dt$ the particle velocity vector.

Mass conservation Law

The mass conservation law states that the decreasing mass in a given volume equals the mass flux through the surface boundary S of such volume, i.e.

$$\frac{\partial}{\partial t} \iiint_V \rho dV = - \iint_S \rho \mathbf{v} \cdot d\mathbf{S}, \tag{1.1.6}$$

where the right hand side can be converted into a volume integral applying Gauss' theorem

$$\frac{\partial}{\partial t}\iiint_V \rho dV = -\iiint_V \nabla(\rho\mathbf{v})dV, \tag{1.1.7}$$

therefore, the continuity equation is

$$\nabla(\rho\mathbf{v}) + \frac{\partial\rho}{\partial t} = 0. \tag{1.1.8}$$

State equation

The state equation is derived from the Bulk modulus, which is defined as the ratio of the infinitesimal pressure increase to the resulting relative decrease of the volume.

$$B = -V\frac{dP}{dV} = \rho\frac{dP}{d\rho} \rightarrow dP = \frac{B}{\rho}d\rho. \tag{1.1.9}$$

Taking into account Eq. (1.1.1) and applying the chain rule to differentiate Eq. (1.1.9) with respect to space $\mathbf{r}$ and time t we can obtain the following equation

$$\frac{\partial P}{\partial t}dt + d\mathbf{r}\cdot\nabla P = \frac{B}{\rho}\left(\frac{\partial\rho}{\partial t}dt + d\mathbf{r}\cdot\nabla\rho\right), \tag{1.1.10}$$

then dividing by dt we obtain the state equation

$$\frac{\partial P}{\partial t} + \mathbf{v}\cdot\nabla P = \frac{B}{\rho}\left(\frac{\partial\rho}{\partial t} + \mathbf{v}\cdot\nabla\rho\right). \tag{1.1.11}$$

Helmholtz equation

Once the three equations are obtained, by neglecting non-linear terms, they can be rewritten as

$$\nabla P + \rho \frac{\partial \mathbf{v}}{\partial t} = 0, \qquad \text{((1.1.5) revisited)}$$

$$\frac{\partial \rho}{\partial t} + \mathbf{v} \cdot \nabla \rho = -\rho \nabla \cdot \mathbf{v}, \qquad \text{((1.1.8) revisited)}$$

$$\frac{\partial P}{\partial t} - \frac{B}{\rho}\left(\frac{\partial \rho}{\partial t} + \mathbf{v} \cdot \nabla \rho\right) = 0. \qquad \text{((1.1.11) revisited)}$$

By combining Eq. (1.1.8) and (1.1.11) we obtain

$$\frac{\partial P}{\partial t} + B \nabla \cdot \mathbf{v} = 0. \tag{1.1.12}$$

Taking the derivative of Eq. (1.1.5) with respect to space and the derivative of Eq. (1.1.12) with respect to time and combining them we arrive to the well known Helmholtz equation

$$\nabla^2 P + \frac{\rho}{B} \frac{\partial^2 P}{\partial t^2} = 0. \tag{1.1.13}$$

Equation (1.1.13) shows, that the Bulk modulus B and the mass density ρ define the acoustic properties of an isotropic fluid. Sometimes these parameters are given in terms of the sound speed c or the characteristic acoustic impedance Z, which are defined as

$$c = \sqrt{\frac{B}{\rho}}, \tag{1.1.14}$$

$$Z = \rho c. \tag{1.1.15}$$

1.1.2 Solutions to the Helmholtz equation

To show an example of the solution of Equation (1.1.13), let's consider an homogeneous 2D fluid media with Bulk modulus B and mass density ρ. Considering time harmonic solutions of the form $e^{-i\omega t}$, then the solution of the Eq. (1.1.13) for Cartesian coordinates has the following form

$$P(x, y) = \left[C_1^{(x)} e^{ik_x x} + C_2^{(x)} e^{-ik_x x}\right]\left[C_1^{(y)} e^{ik_y y} + C_2^{(y)} e^{-ik_y y}\right], \tag{1.1.16}$$

where the $C_i^{(x)}$ and $C_i^{(y)}$ are coefficients to be determined with the boundary conditions and k_i are the wave number components, such that

$$k^2 = k_x^2 + k_y^2 = \frac{\rho\omega^2}{B}. \tag{1.1.17}$$

In a similar way, the solution of Eq. (1.1.13) (polar coordinates) is an expansion in q-terms of Bessel functions (see Appendix A). The incoming and outgoing waves are expressed as a combination of regular Bessel functions $J_q(x)$ and first kind Hankel functions $H_q(x) = J_q(x) + iY_q(x)$, respectively, i.e.

$$P(r,\theta) = \sum_q \left[A_q J_q(k_r r) + B_q H_q(k_r r)\right] e^{iq\theta}, \tag{1.1.18}$$

where the A_q and B_q are coefficients to be determined using the boundary conditions. In addition, k_r is the wave number obtained from

$$k_r^2 = \frac{\rho\omega^2}{B}. \tag{1.1.19}$$

1.1.3 Boundary conditions

To couple the solution of the equation of motion of two different media, the boundary conditions have to applied at the interface between the two media Ω. For the case of two fluid media, continuity of the pressure and the normal speed has to be accomplished.

$$P^-\big|_\Omega = P^+\big|_\Omega\,, \tag{1.1.20a}$$
$$\mathbf{v}_\perp^-\big|_\Omega = \mathbf{v}_\perp^+\big|_\Omega\,. \tag{1.1.20b}$$

Notice that the particle velocity $\mathbf{v}$ can be defined in terms of the pressure P using Eq. (1.1.5).

From the equations above every other boundary condition can be specified. The most common are the rigidly condition, when the wave impinges a rigid object in which the particles cannot be displaced, so that

$$\mathbf{v}_{\perp}^{-}\big|_{\Omega} = 0, \tag{1.1.21}$$

and the vacuum condition, where the lack of particles makes it impossible to have a pressure, so

$$P^{-}\big|_{\Omega} = 0. \tag{1.1.22}$$

1.2 Single scatterer

When an external field impinges a close region Ω with different acoustic parameters than the background, a scattering phenomenon occurs. In the present work, the close region is considered an infinite long cylinder and therefore the problem will be solved using Polar coordinates in 2D.

Let us consider a fluid cylinder with radius R_a and acoustic parameters (B_a, ρ_a) immersed in a fluid background with acoustic parameters (B_b, ρ_b) as schematically depicted in Fig 1.2. The solution of the Helmholtz equation in each medium (in polar coordinates) takes the form

$$P^{(inc)} + P^{(scat)} = \sum_q A_q J_q(k_b r) e^{iq\theta} + \sum_q B_q H_q(k_b r) e^{iq\theta} \qquad r > R_a, \tag{1.2.1a}$$

$$P^{(int)} = \sum_q C_q J_q(k_a r) e^{iq\theta} \qquad r \leq R_a, \tag{1.2.1b}$$

where

$$k_b = \sqrt{\frac{\rho_b}{B_b}}\omega, \tag{1.2.2a}$$

$$k_a = \sqrt{\frac{\rho_a}{B_a}}\omega, \tag{1.2.2b}$$

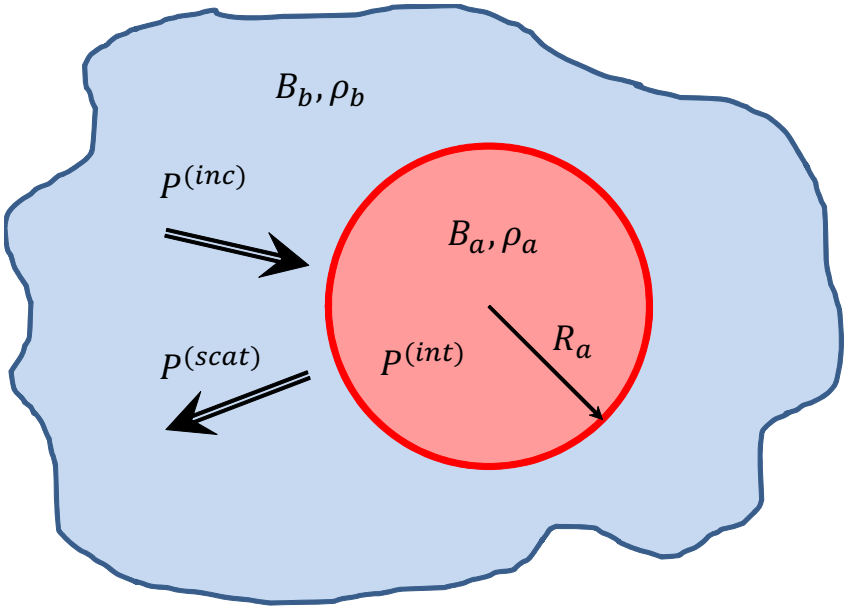

Figure 1.2: Single scatter with radius R_a and acoustic parameters (B_a, ρ_a) immersed in a fluid background with acoustic parameters (B_b, ρ_b). An incoming wave P_{inc} impinges the cylinder and generates a scattering wave P_{scat} and an internal wave P_{int}.

and $P^{(inc)}$, $P^{(scat)}$ and $P^{(int)}$ defines the incoming, scattered and internal wave, respectively. Notice that the field inside of the cylinder does not have an outgoing wave, since there is no source inside.

In the general problem, the incoming coefficients A_q are the inputs and the scattered coefficients B_q are the outputs. Therefore, both of them can be related through a infinite matrix called the transfer matrix or T-matrix as

$$\begin{bmatrix} \vdots \\ B_q \\ \vdots \end{bmatrix} = \begin{bmatrix} \ddots & \vdots & \\ \cdots & T_{qs} & \cdots \\ & \vdots & \ddots \end{bmatrix} \begin{bmatrix} \vdots \\ A_s \\ \vdots \end{bmatrix} \tag{1.2.3}$$

To obtain the T-matrix it is necessary to apply the boundary conditions of a circular interface [Eq. (1.1.20)] to our system

$$\left(P^{(inc)} + P^{(scat)}\right)\Big|_{r=R_a} = P^{(int)}\Big|_{r=R_a}, \tag{1.2.4a}$$

$$\frac{1}{\rho_b}\left(\frac{\partial P^{(inc)}}{\partial r} + \frac{\partial P^{(scat)}}{\partial r}\right)\Bigg|_{r=R_a} = \frac{1}{\rho_a}\frac{\partial P^{(int)}}{\partial r}\Bigg|_{r=R_a}, \tag{1.2.4b}$$

leading to the following system of equations

$$\sum_q A_q J_q(k_b R_a)e^{iq\theta} + \sum_q B_q H_q(k_b R_a)e^{iq\theta} = \sum_q C_q J_q(k_a R_a)e^{iq\theta}, \tag{1.2.5a}$$

$$\frac{k_b}{\rho_b}\sum_q A_q J'_q(k_b R_a)e^{iq\theta} + \sum_q B_q H'_q(k_b R_a)e^{iq\theta} = \frac{k_a}{\rho_a}\sum_q C_q J'_q(k_a R_a)e^{iq\theta}. \tag{1.2.5b}$$

The sums in q can be eliminated multiplying by $e^{is\theta}$ and integrating from 0 to 2π. In this case only the terms $s = q$ are different than zero and the equations become

$$A_q J_q(k_b R_a) + B_q H_q(k_b R_a) = C_q J_q(k_a R_a), \tag{1.2.6a}$$

$$\frac{k_b}{\rho_b} A_q J'_q(k_b R_a) + B_q H'_q(k_b R_a) = \frac{k_a}{\rho_a} C_q J'_q(k_a R_a). \tag{1.2.6b}$$

Solving this system of equations we obtain the relationship between the coefficients as

$$T_q = \frac{B_q}{A_q} = -\frac{\rho_q J'_q(k_b R_a) - J_q(k_b R_a)}{\rho_q H'_q(k_b R_a) - H_q(k_b R_a)}, \tag{1.2.7a}$$

$$\frac{C_q}{A_q} = \frac{J_q(k_b R_a) + T_q H_q(k_b R_a)}{J_q(k_a R_a)}, \tag{1.2.7b}$$

where

$$\rho_q = \frac{\rho_a k_b}{\rho_b k_a} \frac{J_q(k_a R_a)}{J'_q(k_a R_a)}. \tag{1.2.8}$$

For the cylinder case, the T-matrix is diagonal and note that these equations are only valid when the center of the coordinate system coincides with the center of the cylinder.

1.2.1 Types of incoming waves

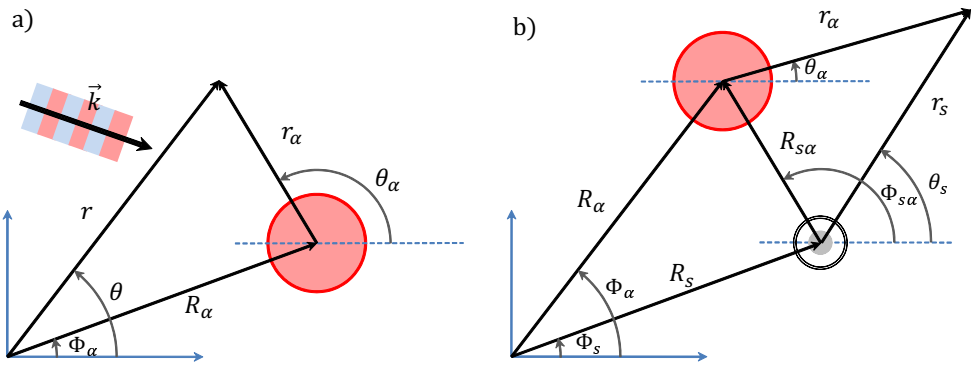

Figure 1.3: Source types: (a) Plane wave with wavenumber $\vec{k}$ and (b) cylindrical point source at (R_s, Φ_s) impinging a cylinder at (R_α, Φ_α).

As shown previously, to obtain the scattering coefficients, the incoming field impinging the system has to be expressed as a combination of Bessel functions with arguments given in polar coordinates $\mathbf{r} = (r, \theta)$. Additionally, if the cylinder is not centered at the origin of coordinates, the reference frame of the incoming field has to be shifted to coincide with the one of the cylinder. The most common incoming waves are the plane wave and the cylindrical point source.

Plane Wave

The plane wave is a constant-frequency wave whose wavefronts (surfaces of constant phase) are infinite parallel planes of constant peak-to-peak

amplitude normal to the phase velocity vector. This incoming field is defined by the wavenumber $\vec{k} = \mathbf{k} = k(\cos(\theta_s), \sin(\theta_s))$ and is represented by

$$P_s(\mathbf{r}) = e^{i\mathbf{k}\cdot\mathbf{r}}. \tag{1.2.9}$$

By using the integral definition of the Bessel function [1] it can be given as

$$P_s(\mathbf{r}) = \sum_q \left[i^q e^{-iq\theta_s}\right] J_q(kr) e^{iq\theta} = \sum_q A_q J_q(kr) e^{iq\theta}. \tag{1.2.10}$$

When the scatter is not placed at the center of the coordinates, the incoming wave can be expressed in a different reference frame α, shown in Fig. 1.3(a), as

$$\begin{aligned} P_s(\mathbf{r}_\alpha) = e^{i\mathbf{k}\cdot\mathbf{R}_\alpha} e^{i\mathbf{k}\cdot\mathbf{r}_\alpha} &= \sum_q \left[i^q e^{\mathbf{k}\cdot\mathbf{R}_\alpha} e^{-iq\theta_s}\right] J_q(kr_\alpha) e^{iq\theta_\alpha} \\ &= \sum_q (A_q)_\alpha J_q(kr_\alpha) e^{iq\theta_\alpha}, \end{aligned} \tag{1.2.11}$$

where $\mathbf{r}_\alpha = \mathbf{r} - \mathbf{R}_\alpha$

Cylindrical point source

The point source is defined as a Hankel function of the same order ξ. Let us consider a cylindrical point source $\xi = 0$ with wavenumber $\mathbf{k}$ located at $\mathbf{R}_s = (R_s, \Phi_s)$ as shown in Fig. 1.3(b), then the incoming pressure pressure field is defined as

$$P_s(\mathbf{r}) = H_\xi(kr_s) e^{i\xi\theta_s}, \tag{1.2.12}$$

where $\mathbf{r}_s = \mathbf{r} - \mathbf{R}_s = (r_s, \theta_s)$. Using Graph's Addition Theorem (see Appendix A.3), the previous equation can be expanded in regular Bessel functions and expressed in a different frame α, shown in 1.3(b), as

$$P_s(\mathbf{r}_\alpha) = \sum_q \left[H_{q-\xi}(kR_{\alpha s})e^{i(\xi-q)\Psi_{\alpha s}}\right] J_q(kr_\alpha)e^{iq\theta_\alpha} = \sum_q (A_q)_\alpha J_q(kr_\alpha)e^{iq\theta_\alpha}, \tag{1.2.13}$$

where $\mathbf{r}_\alpha = \mathbf{r} - \mathbf{R}_\alpha$.

1.3 Multiple scattering

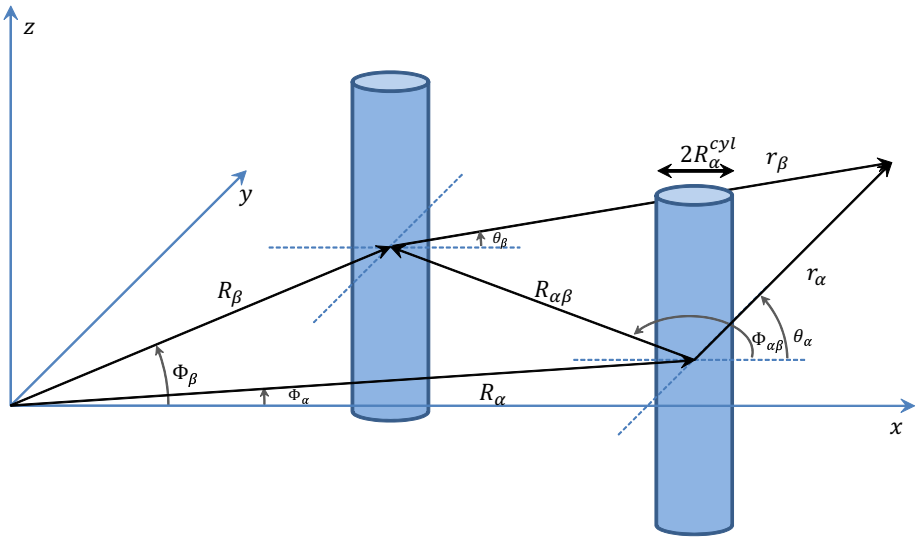

Figure 1.4: Cluster of N=2 cylinders located at (R_α, Φ_α) and (R_β, Φ_β).

Consider a cluster of N cylinders with arbitrary position located at (R_α, Φ_α) and radius R_α^{cyl} with $\alpha = 1, 2, \ldots, N$ as shown if Fig. 1.4. If an external field interacts with the cluster, the total field incoming on the α-cylinder will be a combination of the incident field and the scattered field of all the other cylinders. Therefore the system is completely coupled as the wave "bounces" back and forth through the cluster.

Let us define the total incoming field as $P_\alpha^{(inc)}$, which takes into account all the incoming waves arriving to the α-cylinder; and the total

scattered field as $P_\alpha^{(scat)}$. Their expressions have the form

$$P_\alpha^{(inc)} = \sum_s (A_s^{(T)})_\alpha J_s(k_b r) e^{is\theta}, \tag{1.3.1a}$$

$$P_\alpha^{(scat)} = \sum_q (B_q^{(T)})_\alpha H_q(k_b r) e^{iq\theta}, \tag{1.3.1b}$$

where $(A_s^{(T)})_\alpha$ and $(B_q^{(T)})_\alpha$ are the total incoming and scattered coefficients, which are related by

$$(B_q^{(T)})_\alpha = \sum_s (T_{qs})_\alpha (A_s^{(T)})_\alpha. \tag{1.3.2}$$

As was explained in the previous chapter, the T-matrix relates the incoming and the scattered wave, but only when the center of the coordinate system and the cylinder coincide. To change the position of the origin of coordinates, Graph's Theorem (see Appendix A.3) can be applied, such that the total scattering field created by the β-cylinder described as

$$P_\beta^{(scat)}(r_\beta, \theta_\beta) = \sum_r (B_r^{(T)})_\beta H_r(k_b r_\beta) e^{ir\theta_\beta}, \tag{1.3.3}$$

can be rewritten in the system of coordinates centered at α as

$$P_\beta^{(scat)}(r_\alpha, \theta_\alpha) = \sum_r (B_r^{(T)})_\beta \sum_s \left[H_{s-r}(k_b R_{\alpha\beta}) e^{i(r-s)\Phi_{\alpha\beta}} \right] J_s(k_b r_\alpha) e^{is\theta_\alpha}. \tag{1.3.4}$$

Then the total incident field on the α-cylinder is written as

$$P_\alpha^{(inc)} = \sum_s (A_s)_\alpha J_s(k_b r_\alpha) e^{is\theta_\alpha} + \sum_{\beta \neq \alpha} P_\beta^{(scat)}(r_\alpha, \theta_\alpha), \tag{1.3.5}$$

where $(A_s)_\alpha$ are the incoming coefficients of the external field expressed in the α frame. Notice that both fields are now expressed in the α frame. Combining Eq. (1.3.1a) with (1.3.5) and rearranging terms we obtain

$$(A_s^{(T)})_\alpha = (A_s)_\alpha + \sum_{\beta\neq\alpha}\sum_r (B_r^{(T)})_\beta H_{s-r}(k_b R_{\alpha\beta}) e^{i(r-s)\Phi_{\alpha\beta}}. \tag{1.3.6}$$

Multiplying this equation by $(T_{qs})_\alpha$ and adding for all s we get

$$(B_q^{(T)})_\alpha = \sum_s (T_{qs})_\alpha (A_s)_\alpha + \sum_{\beta\neq\alpha}\sum_s (T_{qs})_\alpha \sum_r (B_r^{(T)})_\beta H_{s-r}(k_b R_{\alpha\beta}) e^{i(r-s)\Phi_{\alpha\beta}}. \tag{1.3.7}$$

By introducing the Kronecker delta function ($\delta_{ij} = 1$ only if $i = j$) and rearranging terms we arrive to the following equation

$$\sum_\beta \sum_r (M_{qr})_{\alpha\beta} (B_r^{(T)})_\beta = (N_q)_\alpha, \tag{1.3.8}$$

where

$$(M_{qr})_{\alpha\beta} = \delta_{\alpha\beta}\delta_{qr} - \sum_s (1-\delta_{\alpha\beta})(T_{qs})_\alpha H_{s-r}(k_b R_{\alpha\beta}) e^{i(r-s)\Phi_{\alpha\beta}}, \tag{1.3.9a}$$

$$(N_q)_\alpha = \sum_s (T_{qs})_\alpha (A_s)_\alpha. \tag{1.3.9b}$$

More specifically, equation (1.3.8) can be written in matrix form as

$$\begin{bmatrix} \vdots & \vdots & \vdots \\ \cdots\ [\mathbf{M}_{qr}]_{\alpha-1\beta-1} & [\mathbf{M}_{qr}]_{\alpha-1\beta} & [\mathbf{M}_{qr}]_{\alpha-1\beta+1}\ \cdots \\ \cdots\ [\mathbf{M}_{qr}]_{\alpha\ \ \beta-1} & [\mathbf{M}_{qr}]_{\alpha\ \ \beta} & [\mathbf{M}_{qr}]_{\alpha\ \ \beta+1}\ \cdots \\ \cdots\ [\mathbf{M}_{qr}]_{\alpha+1\beta-1} & [\mathbf{M}_{qr}]_{\alpha+1\beta} & [\mathbf{M}_{qr}]_{\alpha+1\beta+1}\ \cdots \\ \vdots & \vdots & \vdots \end{bmatrix} \begin{bmatrix} \vdots \\ [\mathbf{B}_r^{(T)}]_{\beta-1} \\ [\mathbf{B}_r^{(T)}]_{\beta} \\ [\mathbf{B}_r^{(T)}]_{\beta+1} \\ \vdots \end{bmatrix} = \begin{bmatrix} \vdots \\ [\mathbf{N}_q]_{\alpha-1} \\ [\mathbf{N}_q]_{\alpha} \\ [\mathbf{N}_q]_{\alpha+1} \\ \vdots \end{bmatrix}, \tag{1.3.10}$$

where $[\mathbf{M}_{qr}]_{\alpha\beta}$ is a $(q \times r)$ matrix, $[\mathbf{B}_r^{(T)}]_\beta$ is a r-length vector and $[\mathbf{N}_q]_\alpha$ is a q-length vector defined as

$$[\mathbf{M}_{qr}]_{\alpha\beta} = \begin{bmatrix} & \vdots & \vdots & \vdots & \\ \cdots & (M_{q-1r-1})_{\alpha\beta} & (M_{q-1r})_{\alpha\beta} & (M_{q-1r+1})_{\alpha\beta} & \cdots \\ \cdots & (M_{q\quad r-1})_{\alpha\beta} & (M_{q\quad r})_{\alpha\beta} & (M_{q\quad r+1})_{\alpha\beta} & \cdots \\ \cdots & (M_{q+1r-1})_{\alpha\beta} & (M_{q+1r})_{\alpha\beta} & (M_{q+1r+1})_{\alpha\beta} & \cdots \\ & \vdots & \vdots & \vdots & \end{bmatrix}, \tag{1.3.11a}$$

$$[\mathbf{B}_r^{(T)}]_\beta = \begin{bmatrix} \vdots \\ (B_{r-1}^{(T)})_\beta \\ (B_r^{(T)})_\beta \\ (B_{r+1}^{(T)})_\beta \\ \vdots \end{bmatrix} \quad ; \quad [\mathbf{N}_q]_\alpha = \begin{bmatrix} \vdots \\ (N_{q-1})_\alpha \\ (N_q\quad)_\alpha \\ (N_{q+1})_\alpha \\ \vdots \end{bmatrix}. \tag{1.3.11b}$$

To solve the infinite linear systems described in Eq. (1.3.10) it is truncated so that $\max|q| = \max|r| = \max|s| < Q$. Then the total scattering coefficients $(B_r^{(T)})_\alpha$ are obtained and the total pressure field P in the background medium is calculated as

$$P(\mathbf{r}) = \sum_q A_q J_q(k_b r) e^{iq\theta} + \sum_\alpha \sum_q (B_q^{(T)})_\alpha H_q(k_b r_\alpha) e^{iq\theta_\alpha}, \tag{1.3.12}$$

with $\mathbf{r}_\alpha = \mathbf{r} - \mathbf{R}_\alpha$ being the distance from the center of the α-cylinder to an arbitrary position $\mathbf{r}$ in the background medium.

To calculate the internal field of each cylinder, the internal coefficients of each cylinder $(C_q)_\alpha$ are needed. These are obtained by inserting the total incoming coefficients of the α-cylinder [see Eq. (1.3.6)] into Eq. (1.2.7b).

1.4 Effective transfer matrix

The effective transfer matrix T^{eff} describes the effective scattering properties of a cluster of N cylinders. With this matrix is possible to calculate

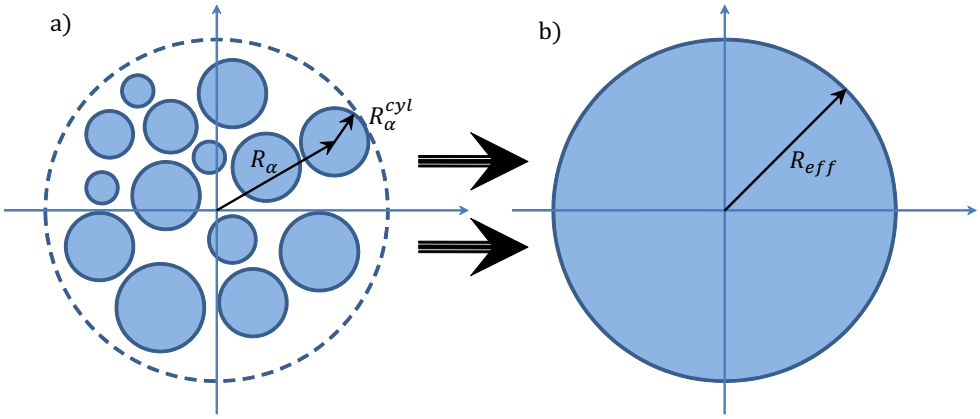

Figure 1.5: Schematic view of (a) a cluster of cylinders located at R_α with radius R_α^{cyl} and (b) effective cylinder of radius R_{eff}.

the total scattering field outside the cluster, expressed as the scattering field from an effective cylinder with radius $R_{eff} = \max(R_\alpha + R_\alpha^{cyl})$ (dashed line in Fig. 1.5). This will be important later on to obtain the effective medium properties of the cluster in the low frequency limit.

The total scattering field produced by a cluster of cylinder can be obtained from the second term of Eq. (1.3.12) (changing the notation) as

$$P^{(scat)}(\mathbf{r}) = \sum_\beta \sum_r (B_r^{(T)})_\beta H_r(k_b r_\beta) e^{ir\theta_\beta}. \tag{1.4.1}$$

By applying Graf's addition theorem, as described in Appendix A.3, it can be cast as

$$P^{(scat)}\mathbf{r} = \sum_p B_p^{eff} H_p(k_b r) e^{ip\theta}, \qquad \mathbf{r} > R_{eff} \tag{1.4.2}$$

where B_p^{eff} are the effective scattering coefficients of the introduced effective cylinder

$$B_p^{eff} = \sum_\beta \sum_r J_{p-r}(k_b R_\beta) e^{i(r-p)\Phi_\beta} (B_r^T)_\beta. \tag{1.4.3}$$

Combining this equation with Eq. (1.3.8) , the relationship between the incoming wave coefficients in the α-frame and the effective scattering coefficients are obtained as

$$B_p^{eff} = \sum_{\alpha,\beta} \sum_{q,r,s} J_{p-r}(k_b R_\beta) e^{i(r-p)\Phi_\beta} (M_{qr}^{-1})_{\alpha\beta} (T_{qs})_\alpha (A_s)_\alpha. \tag{1.4.4}$$

Notice that the M matrix has been inverted. Now, the coefficients $(A_s)_\alpha$ have to be expressed in the origin of coordinates. Thus, by applying Graf's addition theorem (Appendix A.3), the effective T-matrix is finally obtained as

$$T_{pt}^{eff} = \frac{B_p^{eff}}{A_t} = \sum_{\alpha,\beta} \sum_{q,r,s,t} J_{p-r}(k_b R_\beta) e^{i(r-p)\Phi_\beta} (M_{qr}^{-1})_{\alpha\beta} (T_{qs})_\alpha J_{t-s}(k_b R_\alpha) e^{i(t-s)\Phi_\alpha}. \tag{1.4.5}$$

1.5 Scattering cross section

Once the scattering field of a cylinder or cluster is obtained it is possible to plot the resulting two dimensional pressure maps. This is a useful technique, but in order to compare the effects produced by two different systems, two dimensional plots are not enough. Line plots are more suitable to do it. The most useful scalar quantity is the scattering cross section (SCS).

The SCS is defined in optics as a hypothetical area describing the likelihood of light particles being scattered by a scattering center. It is a measure of the strength of the interaction between the scattered particles and one or several scattering centers. In our case, the SCS also describes the shape of the scattered pressure at the far field produced by a single cylinder or cluster. It is defined as

$$\sigma_{scat}(k,\theta) = \lim_{r\to\infty} \left| \sqrt{r} P^{scat}(r,\theta) \right|, \tag{1.5.1}$$

where P^{scat} is the scattered field produced by the cylinder or the cluster. As explained before, both are combination of Hankel functions, so the asymptotic expression detailed in Appendix A can be used.

Combining Eq. (1.2.1a), (1.5.1) and (A.1.10) the SCS of a single cylinder centered in the origin of coordinates is

$$\sigma_{scat}(k,\theta) = \left| \sqrt{\frac{2}{\pi k}} \sum_q (-i)^q B_q e^{iq\theta} \right| . \tag{1.5.2}$$

This equation is also valid to calculate the scattering by a cluster if the effective scattering coefficients are known. Instead of using B_q, we should use the coefficients B_q^{eff}.

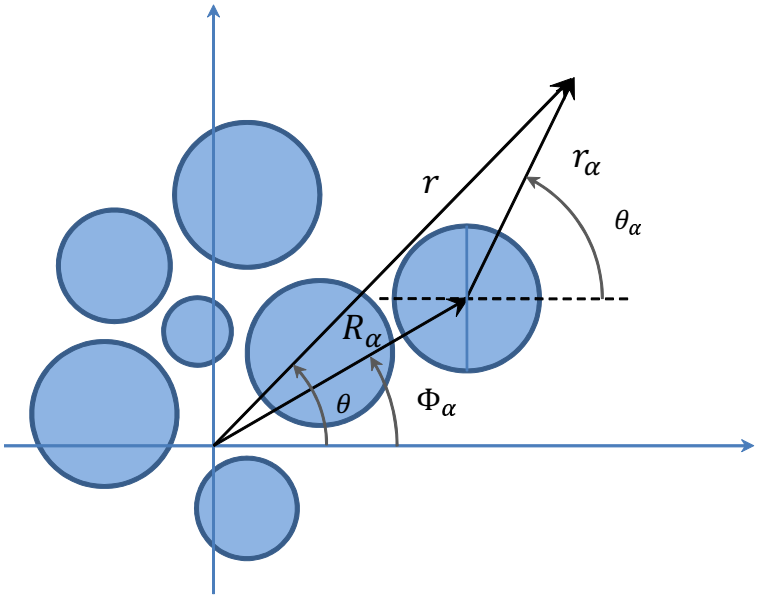

Figure 1.6: Variables needed to calculate the scattering cross section.

Another way to calculate the SCS of a cylinder is through the $(B_q^{(T)})_\alpha$ coefficients [see Eq. (1.3.12)]. The calculation is more complex and some of the steps will be below. Let's consider the cluster shown in Fig 1.6. From the right hand side of Eq. (1.3.12) we know that

$$P^{scat}(r,\theta) = \sum_{\alpha}\sum_{q}(B_q^{(T)})_\alpha H_q(kr_\alpha)e^{iq\theta_\alpha}. \tag{1.5.3}$$

When $r \to \infty$ we can apply the asymptotic expression of the Hankel function [Eq. (A.1.10)]. Then the previous equation is rewritten as

$$\lim_{r\to\infty} P^{scat}(r,\theta) \approx \sum_{\alpha}\sum_{q}(B_q^{(T)})_\alpha \sqrt{\frac{2}{\pi kr}}(-i)^q e^{-i\pi/4} e^{ik(r_\alpha - R_\alpha\cos(\theta-\Phi_\alpha))} e^{iq\theta}, \tag{1.5.4}$$

where the following simplifications have been performed

$$\lim_{r\to\infty} r_\alpha \approx \begin{cases} r - R_\alpha\cos(\theta-\Phi_\alpha) & \text{For the exponentials} \\ r & \text{For the rest} \end{cases} \tag{1.5.5}$$

$$\lim_{r\to\infty} \theta_\alpha \approx \theta \tag{1.5.6}$$

Finally, the SCS of a cluster of cylinders is

$$\sigma_{scat}(k,\theta) = \left| \sqrt{\frac{2}{\pi k}} \sum_{q}\sum_{\alpha}(-i)^q (B_q^{(T)})_\alpha e^{-ikR_\alpha\cos(\theta-\Phi_\alpha)} e^{iq\theta} \right|. \tag{1.5.7}$$

1.6 Energy flux

In a two dimensional system, the energy flux (Φ) is the rate of energy transfer through a boundary and is mathematically defined as the integral of the intensity vector $\mathbf{I}$ normal to the contour Ω

$$\Phi = \int_{\Omega} (\mathbf{I}\cdot\mathbf{n})\, d\Omega, \tag{1.6.1}$$

where $\mathbf{I}$ is defined as the pressure P times the complex conjugate of the particle velocity $\mathbf{v}$. Applying Eq. (1.1.5) the final form of the intensity is

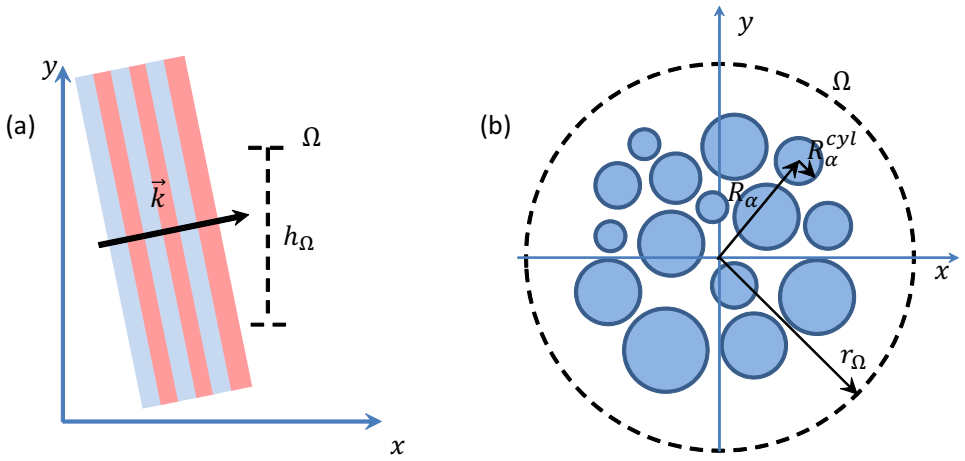

Figure 1.7: Variables used to calculate the intensity of (a) a plane wave and (b)a cluster .

$$\mathbf{I} = \frac{1}{2}\Re\left[P\mathbf{v}^*\right] = \frac{1}{2\omega\rho}\Re\left[iP\nabla P^*\right]. \tag{1.6.2}$$

In the following paragraphs, we calculate the energy flux of the two main fields used during this work: A plane wave and the field produced by the interaction of an external wave impinging a cylinder or a cluster.

Plane wave

In the case of a plane wave, it is common to calculate the energy flux of a line segment Ω of length h_Ω (see Fig. 1.7a) . Taking into account that the wavenumber is defined as $\vec{k} = \mathbf{k} = (k_x, k_y)$ and the vector normal to Ω is $\mathbf{n} \equiv \hat{x}$, then the energy flux is

$$\Phi = \int_{-h_\Omega/2}^{h_\Omega/2} I_x dy. \tag{1.6.3}$$

Since the x-component is needed, combining Eq. (1.2.9) and (1.6.2) gives the intensity as

$$I_x = \frac{k_x}{2\omega\rho}, \tag{1.6.4}$$

and the energy flux is

$$\Phi = \frac{k_x h_\Omega}{2\omega\rho}. \tag{1.6.5}$$

Single cylinder or cluster

To calculate the energy flux of a cylinder or cluster it is common to define the contour Ω as the boundary of a circle of radius

$$r_\Omega > \max(R_\alpha + R_\alpha^{cyl}), \tag{1.6.6}$$

R_α being the radial position of the cylinder and R_α^{cyl} the radius of the cylinder (see Fig. 1.7b). In this case, the normal vector to the contour coincides with the radial vector and only the radial component of the intensity I_r is needed. Then the energy flux is defined as

$$\Phi = \oint_0^{2\pi} I_r d\theta. \tag{1.6.7}$$

From Eq. (1.2.1a) we know that the background field produced by a single scattered is

$$P(r,\theta) = \sum_q \left[A_q J_q(kr) + \left(\sum_s T_{qs} A_s \right) H_q(kr) \right] e^{iq\theta}, \tag{1.6.8}$$

where the definition of the T-Matrix [Eq. (1.2.3)] was used. Then,

$$I_r = \frac{1}{2\omega\rho} \Re \left[iP\nabla P_r^* \right], \tag{1.6.9}$$

with

$$P\nabla P_r^* = \sum_q \sum_r k e^{i(q-r)\theta} \left[A_q J_q(kr) + \left(\sum_s T_{qs} A_s \right) H_q(kr) \right] \times \left[A_r^* J_r'^*(kr) + \left(\sum_t T_{rt}^* A_t^* \right) H_r'^*(kr) \right]. \tag{1.6.10}$$

Note the change in the sub-indexes. To further simplify this equation a few points have to be stressed

1. To obtain the energy flux [Eq. (1.6.7)], the radial intensity is integrated from 0 to 2π. In this case, only the terms $r = q$ are different from zero.

2. If the arguments J and H are real, then the complex conjugate of the radial functions can be eliminated by expanding $H = J + iY$. Additionally, the Wronskian identity defined in Appendix A can be used.

3. Notice also from Eq. (1.6.9) that only the pure imaginary terms are needed.

4. The following properties apply to complex numbers $ZZ^* = |Z|$, $Z + Z^* = 2\Re[Z]$ and $Z - Z^* = 2\Im[Z]$.

By considering the points above and rearranging terms the final form of the energy flux is

$$\Phi = \frac{2}{\omega\rho} \sum_q \sum_s \sum_t \Re\left[A_s A_t^* (\delta_{qs} T_{qt}^* + T_{qs} T_{qt}^*)\right]. \tag{1.6.11}$$

For the case of a cluster instead of using the matrix elements T_{qs}, we use the elements T_{pt}^{eff} described in Eq. (1.4.5), changing the sub-indexes accordingly.

As stated previously, the normal to the surface coincides with the radial vector (towards infinity). As a consequence, if $\Phi > 0$ then inside the region there is a source of energy. When $\Phi < 0$ the inside the region is absorptive. Finally, if $\Phi = 0$ then the same amount of energy that enters, leaves the region enclosed by Ω. This method has been used through out this work to test if the T-matrix has been calculated correctly.

1.7 Homogenization method

The homogenization defines the procedure of retrieving the effective parameters from the properties of a metamaterial sample. To fully understand the process of obtaining these effective properties, the reader is addressed to the work of Torrent et al. [76]. Here only a brief explanation and the final results are given. The homogenization method states that, for wavelengths larger than a certain cut-off given approximately by $\lambda > 4a$, where a is the lattice separation, a composite material behaves as an homogeneous one with effective acoustic and geometric properties. In our case, the metamaterial consists of a lattice of sound scatters, named sonic crystals.

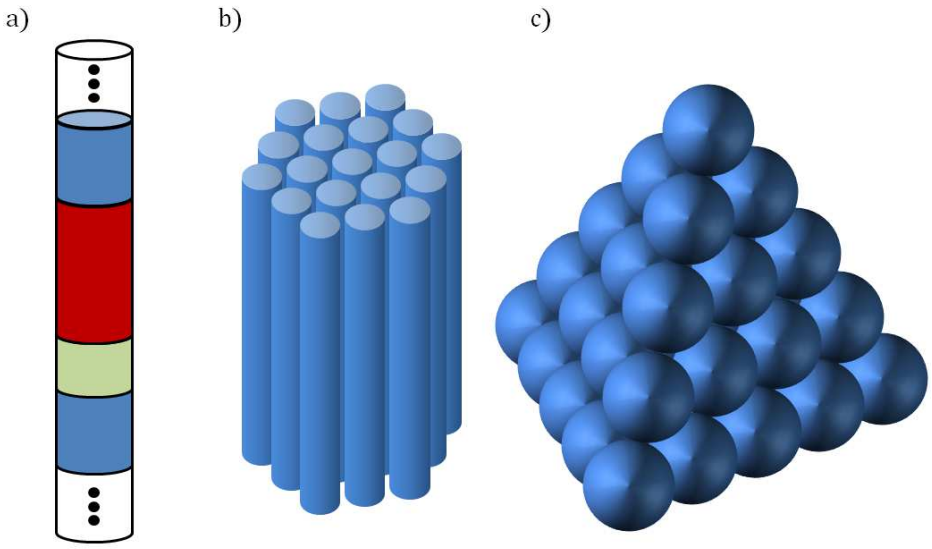

Figure 1.8: Types of sonic crystals (SC): (a) 1D-SC as a combination of different materials, (b) 2D-SC as a hexagonal cluster of cylinders and (c) 3D-SC as a cluster of spheres.

Sonic crystals (SC) are periodic arrangements of inclusion inside an homogeneous background. As figure 1.8 shows, SC can be one, two and three dimensional system. The 1D-SC consist mainly of alternate binary structures, being the 2D-SC and 3D-SC commonly formed by inclusions

of infinite long cylinders or spheres, respectively, embedded in a background.

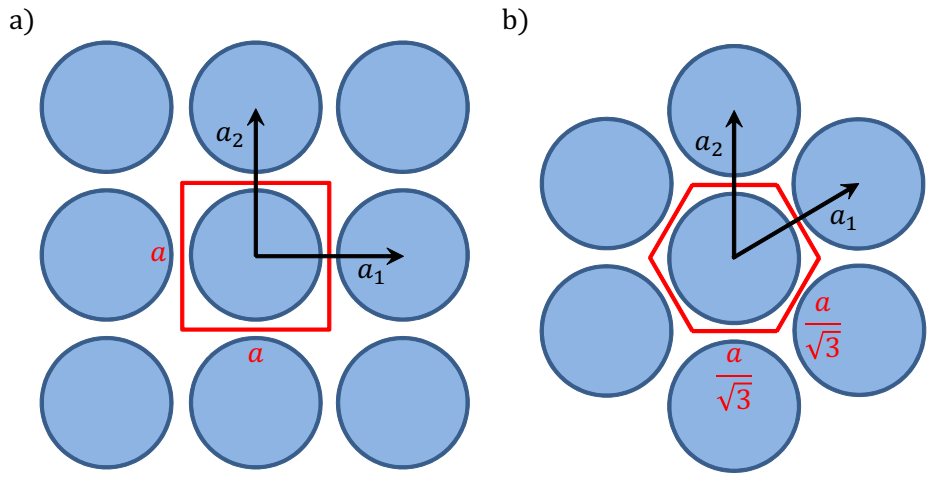

Figure 1.9: Types of sonic crystal structures:(a) Square and (b) Hexagonal Lattices.

For the whole extent of this manuscript, let us focus in 2D-SC. As explained, they consist of infinite long cylinders arranged in many different crystal structures. The most common are shown in figure 1.9: the square (a) and the hexagonal (b) lattices. From solid state physics it is known that a crystal structures is comprised of unit cells (red areas). Inside each one, a scattering unit is placed. The 2D-SC is represented in terms of its the Bravais lattice $\mathbf{R} = n_1\mathbf{a}_1 + n_2\mathbf{a}_2$, where n_1 and n_2 are real numbers and $\mathbf{a}_1$ and $\mathbf{a}_2$ are the primitive vectors

$$\mathbf{a}_1 = (a, 0) \quad ; \quad \mathbf{a}_2 = (0, a) \qquad \text{Square Lattice} \qquad (1.7.1)$$

$$\mathbf{a}_1 = (\frac{\sqrt{3}}{2}a, \frac{1}{2}a) \quad ; \quad \mathbf{a}_2 = (0, a) \qquad \text{Hexagonal Lattice} \qquad (1.7.2)$$

The filling fraction ff is defined as the ratio between the total area occupied by the scatters inside the unit cell and the area of the unit cell itself.

$$ff_{sq} = \frac{\pi R_\alpha^2}{a^2} = \pi \left(\frac{R_\alpha}{a}\right)^2 \tag{1.7.3}$$

$$ff_{hex} = \frac{\pi R_\alpha^2}{\sqrt{3}a^2/2} = \frac{2\pi}{\sqrt{3}} \left(\frac{R_\alpha}{a}\right)^2 \tag{1.7.4}$$

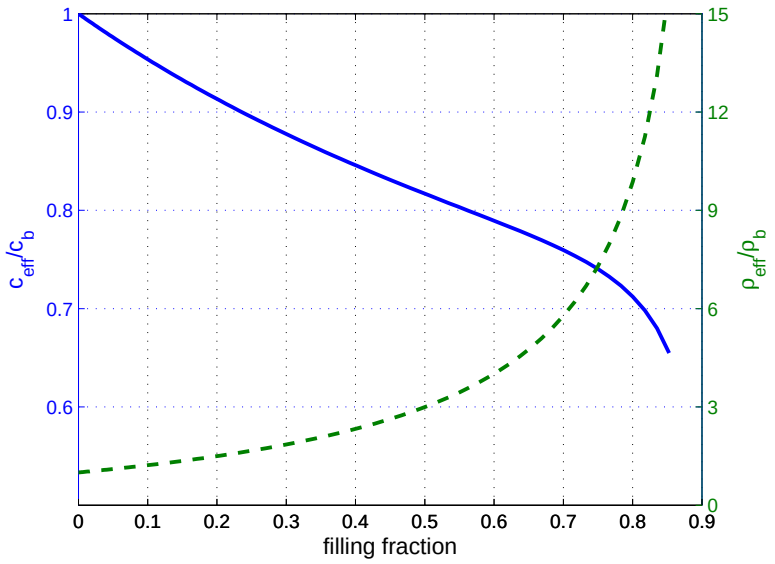

Figure 1.10: Effective sound speed (blue continuous line) and effective mass density (green dashed line) as a function of the filling fraction.

Once the sonic crystals are introduced, the process for obtaining their effective properties can be described. As explained, the scattered field produced from a cluster can be expressed in terms of the effective T-matrix T_{qs}^{eff} [Eq. (1.4.5)]. If the external shape of the cluster is nearly circular, it is expected that the cluster can be homogenized to a single scattered with effective acoustic and geometric properties. Then, its matrix elements T_{qs}^{cyl} can also be calculated. In the low frequency limit we propose the condition

$$\lim_{\lambda \to \infty} \frac{T_{qs}^{eff}}{T_{qs}^{cyl}} \qquad \forall q, s \tag{1.7.5}$$

and through a process that applies the asymptotic form of the Bessel and Hankel equations, the effective properties of the cluster are obtained as

$$\frac{1}{B_{eff}} = \frac{1-ff}{B_b} + \frac{ff}{B_a} \tag{1.7.6}$$

$$\rho_{eff} = \frac{\rho_a(\Delta+ff)+\rho_b(\Delta-ff)}{\rho_a(\Delta-ff)+\rho_b(\Delta+ff)}\rho_b \tag{1.7.7}$$

$$c_{eff} = \sqrt{\frac{B_{eff}}{\rho_{eff}}} \tag{1.7.8}$$

where the factor Δ is a function of ff and the acoustic parameters of the cylinders. B_i and ρ_i are the Bulk modulus and the mass density, respectively. The sub-index b makes reference to the background and the sub-index a makes reference to the cylinders. The reader is addressed to the work of Torrent et al. to find a comprehensive account of the homogenization method. For the purpose of this manuscript, the factor is tabulated in the Appendix C for the case of rigid cylinders. As a demonstration, Fig. 1.10 shows the behavior of the effective properties of a cluster of rigid cylinders ($\rho_a \to \infty$) for different filling fractions.

Another important parameter used throughout this work is the effective refractive index n_{eff} of the sonic crystals in the homogenization limit. n_{eff} is a dimensionless number that describes how the waves propagates through the medium. It is defined as

$$n_{eff} \equiv \frac{c_b}{c_{eff}}, \tag{1.7.9}$$

where c_b is wave speed in the background. For example, a value of $n_{eff} = 1.33$, means that light travels 1.33 times slower in the metamaterial than in the background fluid. Typically, in optics, the refractive index determines how much light is bent, or refracted, when entering a material. The refractive index was described by Snell's law of refraction, $n_1 \sin\theta_1 = n_2 \sin\theta_2$, where θ_1 and θ_2 are the angles of incidence and refraction, respectively, of a ray crossing the interface between two media with refractive indices n_1 and n_2. The refractive indices also determine

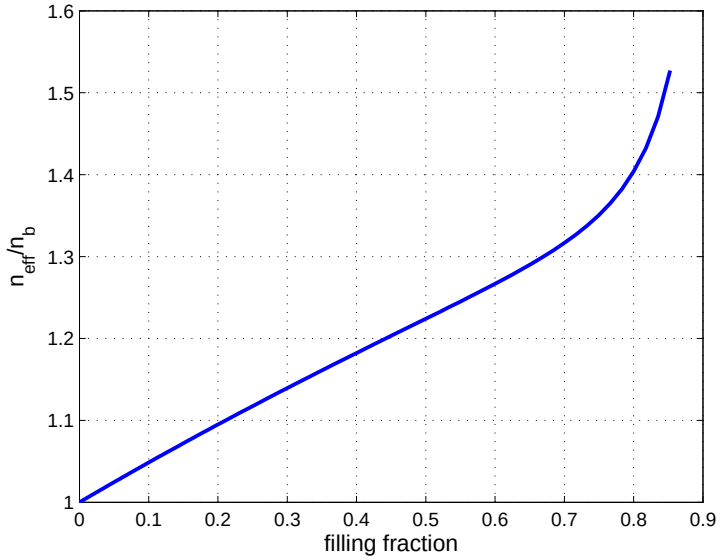

Figure 1.11: Effective refractive index as a function of the filling fraction

the amount of light that is reflected when reaching the interface, as well as the critical angle for total internal reflection. Fig. 1.11 shows how the effective refractive index changes with the filling faction. Notice that for values over $n_{eff} > 1.4$ it changes rapidly with ff, so it will be difficult to control.

Small disturbances in the position or the radius of the cylinders, also known as "'weakly distortion"' and "'structural disorder"', respectively, where studied by Torrent et al. who concluded that both produce little deviations on the effective parameters for very high filling fractions.

Finally, the effective geometry depends on the original shape of the cluster, but two main cases can be differentiated: the circular and the rectangular shape.

For the first case, let's consider the cluster of N cylinders. Then, the effective radius R_{eff} of the homogenized cylinder is defined as

$$R_{eff} = \sqrt{\frac{NA_{uc}}{\pi}}, \tag{1.7.10}$$

where A_{uc} is the area of the unit cell.

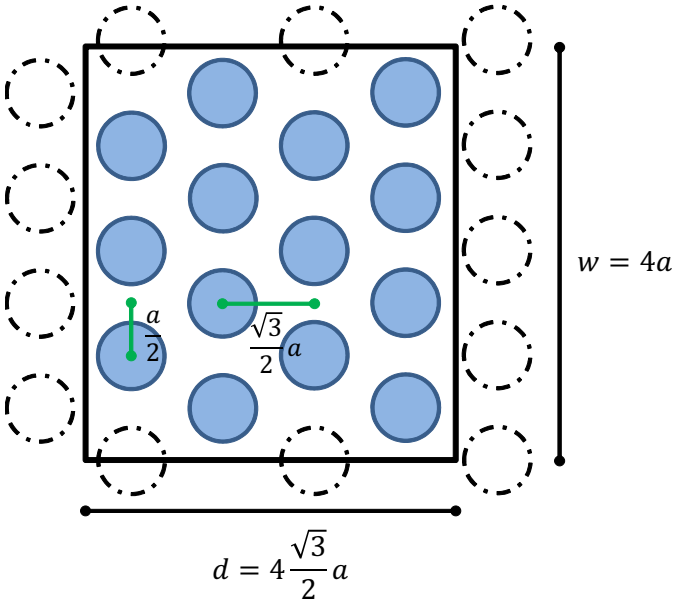

Figure 1.12: Rectangular cluster (7 rows and 5 columns) of width w and length d. The scatters are arranged in a hexagonal lattice with lattice parameter a. The separation between rows and columns of cylinders is $a/2$ and $\sqrt{3/2}a$, respectively.

The rectangular case is shown in Fig. 1.12. It consist of a rectangular hexagonal lattice SC with M rows and N columns. Following the standard solid state physics, the surface position is taken at a distance above the atoms equal to a half of the lattice vector. Then the width w and the length d are defined as

$$w = (M-1)\frac{a}{2} + 2\frac{a}{4} \tag{1.7.11}$$

$$d = (N-1)a + 2\frac{a}{2} \tag{1.7.12}$$

where a_i are the lattice vector defined in Eq. (1.7.1). Notice that it is important to take the orientation of the hexagonal lattice crystal into account, as the components of the lattice vector are different.

Chapter 2

Gradient index lens

This chapter is devoted to the theoretical definition of a gradient index (GRIN) lens. A model based in ray theory is used to derive the focal position. The GRIN lens sample is designed and its implementation using a 2D sonic crystal is explained. Additionally, the experimental setup employed to characterize the sample is explained. Finally, numerical simulations and experimental data are presented and discussed.

2.1 Introduction

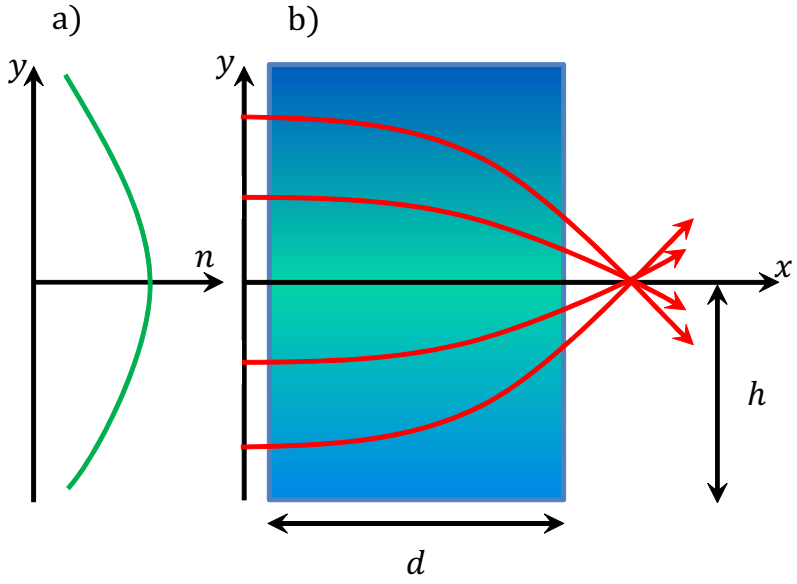

Figure 2.1: Schemes of gradient index lens with length d and width $2h$: (a) Refractive index values and (b) ray trajectory in function of the y-position, respectively

An acoustic gradient index lens is an acoustic lens in which the refractive index n varies gradual along the axis transverse with respect to the propagating wave (see Fig. 2.1). The lens is symmetrical to the wave propagation direction and, by not having a curvature, it is easy to be build. Its upper/lower boundaries have the same refractive index as the background. In optics it is usually fabricated by superposition of homogeneous layers. Each layer has a different refractive index. Thus, the thickness and number of layers defines the quality of the lens. The propagation axis of the GRIN lenses considered here is defined along the x-axis and, therefore, the our lens is built by superpositioning layers in the y-direction. Thus, the refractive index n_y changes along the y-axis; $n_y(y)$.

The physic principle behind the lens operates is the delay introduced

by each layer in the wave that impinges its entrance. The refractive index of the upper layers n_h is smaller than the one of the center n_0, so the particles travel faster there than the ones traveling through the center. This forces the wave front to bends inside the lens. This effect can be described by an internal ray trajectory model. Additionally, upon exiting, the mismatch of refractive index between the lens and the background, forces the beam to further bend. This effects is described in the external ray trajectory model.

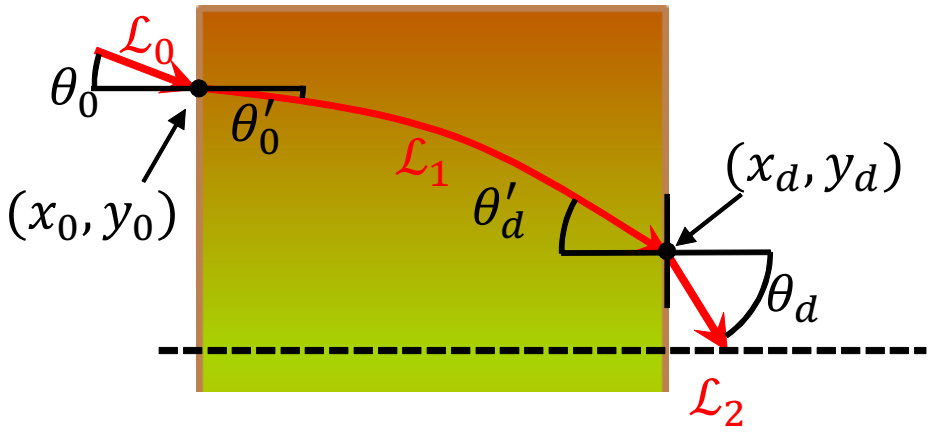

Figure 2.2: Scheme of upper half part of the GRIN lens. The red line shows the trajectory of a ray that enters the lens at (x_0, y_0) and exits at (x_d, y_d). The ray follows the trajectory $\mathcal{L}_0$ before entering, $\mathcal{L}_1$ inside the lens and $\mathcal{L}_2$ after exiting.

Let's suppose the system described in Fig. 2.2. The ray is initially following the trajectory $\mathcal{L}_0$. Then, it impinges the lens at the point (x_0, y_0) with an angle of θ_0. Due to the change of medium it bends towards the normal with an internal angle θ_0'. Then it travels through the lens following the trajectory $\mathcal{L}_1$ described in the internal model and eventually reaches its end. There, the wave impinges the lenses right boundary at (x_d, y_d) with an internal angle θ_d'. Applying Snell's law one more time, the external angle θ_d at the exit point is calculated. After that, it follows a straight line, $\mathcal{L}_2$, and eventually collides with the beam

coming from the other half of the lens forming the focal spot.

2.1.1 Internal ray trajectory model

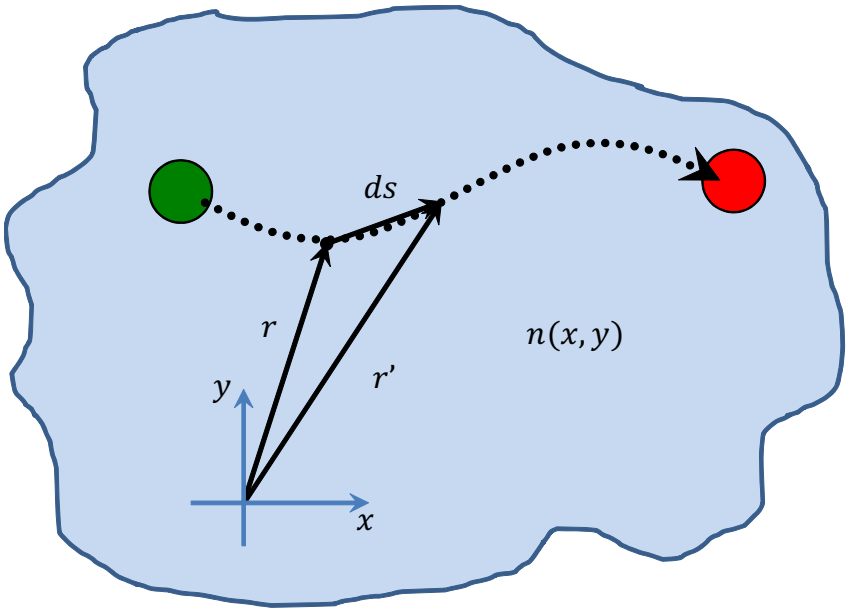

Figure 2.3: Variables of Fermat's principle.

To predict the focal spot position, beam theory can be used to develop a simple model. Although this is used for high frequencies, the error is small and can be corrected using an error constant k added to the lens length d. From the Eikonal Equation in optics [8, p. 122] [78, p. 36] we know that

$$\nabla n(\mathbf{r}) - \frac{d}{ds}\left[n(\mathbf{r})\frac{d\mathbf{r}}{ds}\right] = 0, \tag{2.1.1}$$

where $\mathbf{r} = (x, y) = x\hat{x} + y\hat{y}$ is the particle position and s is the arc length, both shown in Fig. 2.3. In this case, the $n(x, y) \equiv n(y)$, so Eq. (2.1.1) can be separated in two parts

$$-\frac{d}{ds}\left[n(y)\frac{dx}{ds}\right] = 0 \qquad \text{For } \hat{x}, \tag{2.1.2}$$

$$\frac{\partial n(y)}{\partial y} - \frac{d}{ds}\left[n(y)\frac{dy}{ds}\right] = 0 \qquad \text{For } \hat{y}, \tag{2.1.3}$$

with $ds = \sqrt{dx^2 + dy^2}$, and therefore, Eq. (2.1.2) can cast in

$$dx = \frac{C_0}{\sqrt{n^2(y) - C_0^2}}dy, \tag{2.1.4}$$

where C_0 is a constant to be determined. This equation allows to calculate the trajectory of a particle moving inside the refractive medium.

Refractive index function

Once the trajectory is known, a refractive index has to be chosen. The lens is designed with the goal of having low aberration of the focal spot. The aberration is the average deviation of the focal spot along the propagation axis. If the focal spot is inside the lens, the aberration is produced only by the refractive index pattern. In the case of an external focal spot, the aberration is the internal one amplified upon exiting the lens by Snells Law. To minimize this effect, a refractive index profile in the form of a hyperbolic secant is chosen. This refractive index is theoretical studied in [39] achieving internal focusing in large enough GRIN structures without aberration. So the refractive index profile along the transverse direction (y-axis) is defined as

$$n(y) = n_0 \operatorname{sech}(\alpha y) = \frac{n_0}{\cosh(\alpha y)}, \tag{2.1.5}$$

with

$$\alpha = \frac{1}{h}\operatorname{arcosh}\left(\frac{n_0}{n_h}\right), \tag{2.1.6}$$

where h is the semi-width of the lens, n_0 is the refractive index along the x-axis and n_h is the refractive index at the edge of the lens.

Using Eq. (2.1.5) to solve Eq. (2.1.4) (integration by substitution using $t = C_0 \sinh(\alpha y)/n_0$ is needed), the trajectory of a particle inside the GRIN lens $\mathcal{L}_1$ is obtained as

$$\mathcal{L}_1(x) = \frac{1}{\alpha} \operatorname{arsinh}\left[U_0 \cos(\alpha x) + \frac{U_1}{\alpha} \sin(\alpha x)\right], \tag{2.1.7}$$

where

$$U_0 = \sin(C_1)\sqrt{\left(\frac{n_0}{C_0}\right)^2 - 1}, \tag{2.1.8}$$

$$U_1 = \alpha \cos(C_1)\sqrt{\left(\frac{n_0}{C_0}\right)^2 - 1}, \tag{2.1.9}$$

and C_0 and C_1 are constants obtained from the initial conditions.

2.1.2 External ray trajectory model

In our case, the wave propagates along the x-axis . Let us consider that an infinite number of rays impinges the surface of the lens with an angle $\theta_0 = \theta_0' = 0$. So, the beam impinging at a height y_0 has the following initial condition

$$\mathcal{L}_1(0) = y_0, \tag{2.1.10}$$

$$\mathcal{L}_1'(0) = \tan(\theta_0'), \tag{2.1.11}$$

giving the following values for the constants $U_0 = \sinh(\alpha y_0)$ and $U_1 = 0$.

As explained previously (Fig. 2.2), once the beam exits the lens, it travels along a straight line, so

$$\mathcal{L}_2(x) = \mathcal{L}_1(d) + (x - d)\tan(\theta_l), \tag{2.1.12}$$

where

$$\tan(\theta_d) = \frac{\sin(\theta_d)}{\sqrt{1-\sin^2(\theta_d)}}. \tag{2.1.13}$$

Using Snell's Law $n_b \sin(\theta_d) = n(y_d)\sin(\theta'_d)$ we can relate the internal and the external angles as

$$\tan(\theta_d) = \frac{n(y_d)\sin(\theta'_d)}{\sqrt{n_b^2 - n^2(y_d)\sin^2(\theta'_d)}}. \tag{2.1.14}$$

From the definition of the slope we know that $\tan(\theta'_d) = \mathcal{L}'_1(d) < 0$, then

$$\sin(\theta_d^{(I)}) = \frac{\mathcal{L}'_1(d)}{\sqrt{1+\mathcal{L}'_1(d)^2}}. \tag{2.1.15}$$

Combining Eq. (2.1.14) and Eq. (2.1.15) we obtain

$$\tan(\theta_d) = \frac{n(y_d)\mathcal{L}'_1(d)}{\sqrt{n_b^2 - \mathcal{L}'_1(d)^2\left[n^2(y_d) - n_b^2\right]}}. \tag{2.1.16}$$

Notice that $\tan(\theta_d) < 0$, so the slope of $\mathcal{L}_2$ is also negative.

Since the problem is symmetric with respect to $x = 0$, to find the local spot position, we have to find the value that makes $\mathcal{L}_2 = 0$. This value is called the external focal position F_{ext} defined as

$$F_{ext} \equiv d - \frac{\mathcal{L}_1(d)}{\mathcal{L}'_1(d)}\sqrt{\frac{n_b^2 - \mathcal{L}'_1(d)^2\left[n^2(y_d) - n_b^2\right]}{n^2(y_d)}}. \tag{2.1.17}$$

2.2 Design and implementation of a GRIN lens using SC

To obtain the local variation in the refractive index, the GRIN lens has been designed as a 2D sonic crystal (see Fig. 2.4). The SC is made of a rectangular cluster of aluminum cylinders distributed in an hexagonal lattice with lattice parameter $a = 2$ cm. The cluster has a number of $M = 10$ rows (the 11th one is not fabricated), and a maximum number

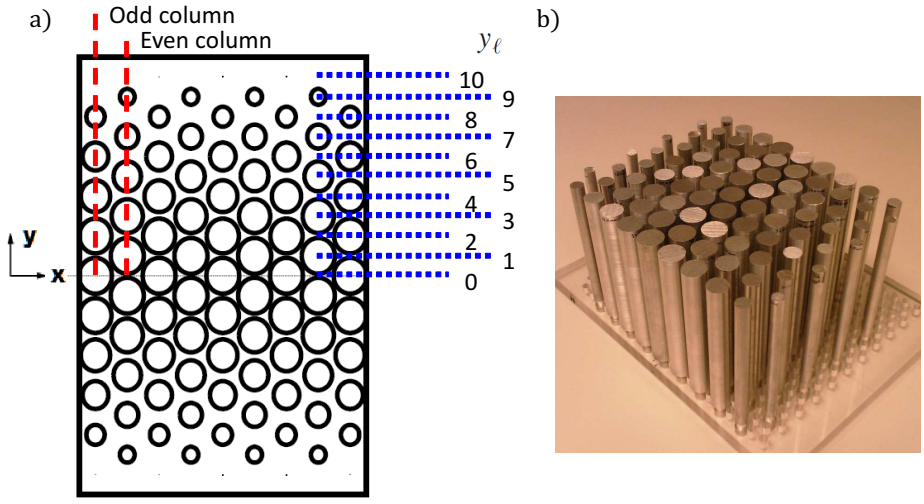

Figure 2.4: (a) Scheme and (b) photo of a 9 columns (layers) gradient index sonic crystal lens.

$N = 9$ of columns. The hexagonal lattice has been chosen because of the possibility of achieving higher filling fractions.

Due to the high acoustic impedance of aluminum compared to air, this material is considered as a rigid body with an infinite mass density. Therefore, the simplified version of the Homogenization method for rigid cylinders can be used. Then, the effective parameters of each unit cell are

$$\frac{1}{B_{eff}} = \frac{1-ff}{B_b}, \tag{2.2.1}$$

$$\rho_{eff} = \frac{\Delta + ff}{\Delta - ff}\rho_b, \tag{2.2.2}$$

which give the following effective refractive index

$$n_{eff} = \left(\frac{c_{eff}}{c_b}\right)^{-1} = \left(\sqrt{\frac{\Delta - ff}{\Delta + ff}}\frac{1}{\sqrt{1-ff}}\right)^{-1}. \tag{2.2.3}$$

The 2D GRIN SC lens studied is designed with a profile $n(y)$ as closer

Table 2.2.1: Effective refractive index $n_{eff}(y_\ell)$ and cylinder radius R_ℓ of the studied 2D GRIN SC

			Odd Layers		Even Layers	
y_ℓ [mm]	$n(y_\ell)$	$n_{eff}(y_\ell)$	ℓ	R_ℓ [mm]	ℓ	R_ℓ [mm]
0	1.330	1.339	6	9.0	-	-
10	1.326	1.339	-	-	5	9.0
20	1.314	1.313	5	8.75	-	-
30	1.293	1.293	-	-	4	8.5
40	1.266	1.258	4	8.0	-	-
50	1.232	1.228	-	-	3	7.5
60	1.193	1.201	3	7.0	-	-
70	1.149	1.151	-	-	2	6.0
80	1.102	1.107	2	5.0	-	-
90	1.052	1.070	-	-	1	4.0
100	1	1	1	0	-	-

as possible to that in Eq. (2.1.5) with $w = 10$ cm, $n_0 = 1.33$ and $n_h = 1$. As in the case of the optical GRIN lens, the acoustical counterpart is also made of L layers. A given layer ℓ is parallel to the x-axis and its independently homogeneous and isotropic. Then the continuous variation of the refractive index $n(y)$ is discredited in $n_{eff}(y_\ell)$. Inside each unit cell, the radius of the cylinder R_ℓ depends on its y_ℓ-position and is calculated using the Homogenization method equations (2.2.2) and the equation of the filling fraction of a hexagonal unit cell defined as $ff_{hex} = 2\pi/\sqrt{3}(R_\ell/a)^2$.

Table 2.2.1 reports the values of R_ℓ obtained. Note that the values corresponding to the upper half of the SC are the only ones reported since the lens is symmetric with respect to the x-axis. Figure 2.4 shows that odd layers have 11 cylinders while even layers have 10 cylinders. Column $n(y_\ell)$ in the table report the exact hyperbolic secant profile while those under $n_{eff}(y_\ell)$ are those effectively achieved in the sample.

Note that the last condition, $y_\ell = 100$, allows a smooth transition with the surrounded air and therefore reduces the unwanted diffraction

effects. These cylinders are not fabricated, as $R_{ell} = 0$, and therefore there are $M = 10$ rows. Then, the effective width and length of the rectangular cluster can be calculated using the equations Eq. (1.7.11) as $w_{eff} = Ma = 20$ cm and $d_{eff} = Na(\sqrt{3}/2)$ that changes with the number of rows N.

2.3 Experimental setup: 2D anechoic chamber

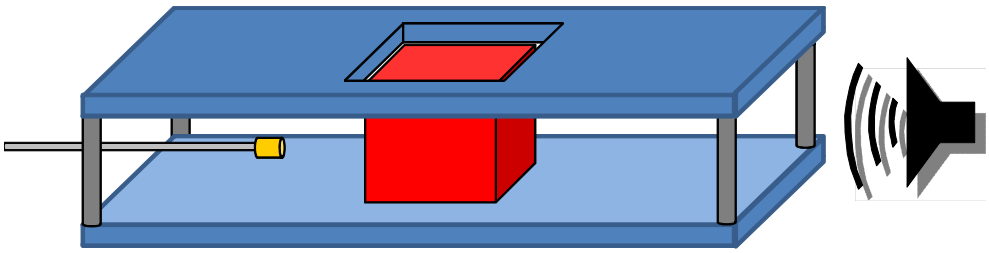

Figure 2.5: Scheme of the 2D anechoic chamber.

Fig. 2.5 shows a scheme of the experimental setup designed to characterize the 2D GRIN SC lenses. The 2D anechoic chamber consists of two parallel metal sheets separated a distance $H = 5$ cm used to simulate a 2D environment. A hole is left in the center of the chamber to place the sample, leaving enough space on the sides. The main objective of the metal sheets is to confine the waves in the z direction. This produces a number n of modes each one with a certain cut-off frequency, $f_c^{(n)}$, calculated with

$$f_c^{(n)} = \frac{n}{2H} c_b. \tag{2.3.1}$$

For frequencies below $f_c^{(1)} = 3.4$ kHz the chamber is considered mono mode along the z direction and the system can be considered as two dimensional. For the frequencies analyzed, from 3.5 kHz up to 4.5 kHz,

there are two vertical modes propagating through the chamber, but the second one has a much larger wavelength and is considered as an offset.

The chamber is open along the $y = 0$ and $y = W$ boundaries. Part of the wave is radiated outside and another one is reflected back. To minimize the disturbance, modulated gaussian pulses are used. Since the experiments are done in the acoustic domain, and, that the sound speed is inferior to the light speed, short pulses can be used instead of continuous signals. The echoes produced by the boundaries have a delay and take more time to arrive at the microphone, so if the signal is a short pulse, the echoes can be filtered by cutting the measurement time. Thus, obtaining an "anechoic effect". The modulated gaussian pulse, $G(t)$, is defined as

$$G(t) = e^{-t^2 \frac{(\sigma\pi)^2}{\ln 2}} \cos(2\pi f_\Omega). \tag{2.3.2}$$

It is known that a Gaussian Pulse has the same profile in frequency and time domain. The parameters affecting the signal are the bandwidth at 3 dB, σ, and the carrier frequency, f_Ω. It is important to choose the value of σ correctly or it will affect the measures. If the bandwidth is small, the modulated gaussian pulse is smaller in time so the echoes have less probability to interact. On the other hand, if the bandwidth is high, it will have more cycles so the spectral energy will be higher, making the signal resistant to noise.

The sound waves propagating along the x-axis are generated with a UDE AC-150 column loudspeaker separated 2 m from the chamber in order to get approximately a plane wavefront at the entrance. To record the transmitted sound, we use a B&K 4958 microphone. Data are acquired in a square area of 24×24 cm^2. The acquisition points are separated by equal distance along the x- and y-axis; i.e., $\Delta x = \Delta y =$ 2 cm. For the wavelength of interest, it satisfies Nyquist criteria, and by interpolating the result data, the complete acoustic field is reconstructed. The data is processed using a PCI acquisition card NI-5105 in a computer. For minimizing the noise, only the FFT value at the used frequency f_Ω is saved.

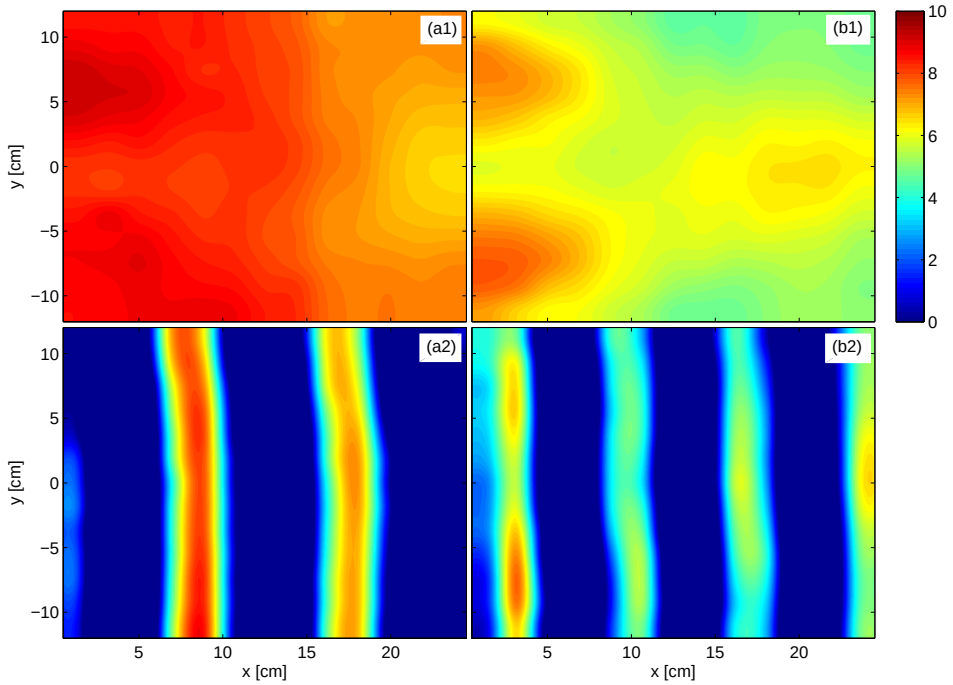

Figure 2.6: Total pressure maps of the empty chamber at 3.5 kHz (a) and 4.5 kHz (b). The upper panels display the absolute value and the lower panels the real part.

Fig. 2.6 shows measurements made without lens at (a) 3.5 kHz and (b) 4.5 kHz. The upper panels display the absolute value and the lower panels the real part. These results confirm that the propagating field inside the chamber has practically a plane wavefront.

2.4 Simulations and Experiments

Using the described 2D anechoic chamber, seven different 2D GRIN SC lenses have been characterized. The lenses differ in the number of columns along the x-axis, from $N = 4$ to $N = 10$. To further analyze the data, the recorded 2D maps have been compared with those obtained by a numerical simulations based on the multiple scattering theory (MST)

explained in section 1.3. Finally, the measured focal spots F_{ext} have been also compared with the values predicted by the ray theory [see Eq. (2.1.17)].

Measurements and simulations are performed from 3.5 kHz up to 4.5 kHz every 100 Hz. In section 1.7, the limit for the Homogenization method is set at $\lambda < 4a$, which, in our case, corresponds to linear frequencies of 4.3 kHz. However, let us stress that the onset for the homogenization is not an exact value and here, we report GRIN lenses working at 4.5 kHz, which is a frequency slightly above the cut-off limit. Moreover, it will be shown that a better agreement with the ray model is obtained in a wider range of lens thicknesses for frequencies near the cut-off limit.

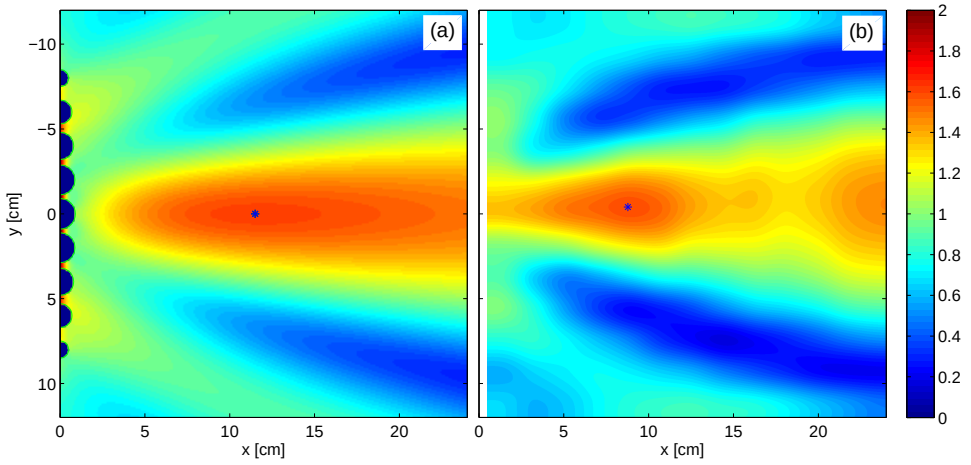

Figure 2.7: Total pressure maps (amplitude) generated by sound waves of 3.5 kHz impinging a 2D GRIN SC lens $N = 9$ columns thick. (a) Numerical simulations performed by using a multiple scattering algorithm. (b) Measurement made in an area 24×24 cm^2 behind the lens. The asterisks mark the positions of the focal spot F_{ext}.

In brief, a 2D sound wave with a plane wavefront is assumed that impinges the lens from the left and the pressure map is calculated or measured at the opposite side. Figs. 2.7(a) and 2.7(b) show the pressure

maps of a GRIN lens made of $N = 9$ columns for the frequency of 3.5 kHz. The focusing effects, focal spot and diffraction lobes, are clearly seen in both maps, calculated and measured. However, the focal area is interrupted for about 5 cm due to some spurious reflection inside the chamber.

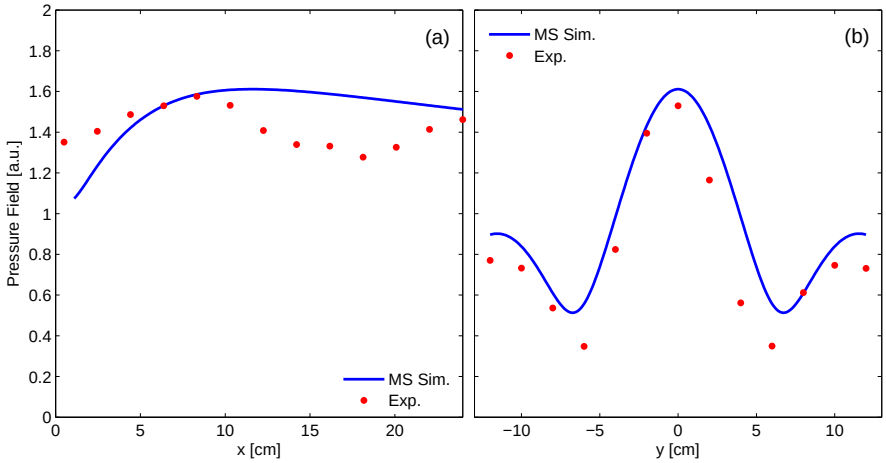

Figure 2.8: Comparison between the Multiple Scattering simulation (blue curve) and the measurements (red dots), for (a) the longitudinal cut and (b) the traversal cut of the the pressure maps in Fig. 2.7 at the focal plane. Both simulations and measurements were made with a $N = 9$ row GRIN PC at a frequency of 3.5 kHz.

A better comparison between data and simulations is given in Figs. 2.8(a) and 2.8(b) that show the longitudinal and traversal profiles at the focal spot obtained from the pressure maps. Good qualitative agreement exists between data and simulations.

Figures 2.9(a) and 2.9(b) present similar plots for the same lens, $N = 9$, but at 4.5 kHz. In comparison with results at 3.5 kHz, now the wavelength is smaller and slightly above the homogenization limit, $\lambda \approx 3.8a$. However the SC clearly behaves like a GRIN lens. The non-symmetric response observed in the experiment is due to the misalignment of the lens inside the setup. The interference described for the larger

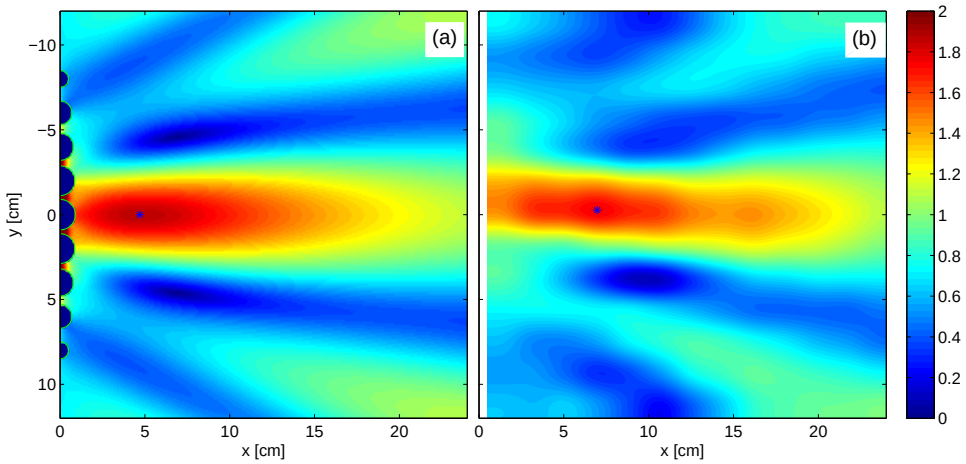

Figure 2.9: Total pressure maps (amplitude) generated by sound waves of 4.5 kHz impinging a 2D GRIN SC lens $N = 9$ columns thick. (a) Numerical simulations performed by using a multiple scattering algorithm. (b) Measurement made in an area 24×24 cm^2 behind the lens. The asterisks mark the positions of the focal spot F_{ext}

frequency is also seen between 13 cm and 18 cm. Moreover, the longitudinal and traversal cuts shown in Figs. 2.10(a) and 2.10(b), respectively, let us to conclude that the agreement between data and simulations is slightly better for this frequency than for 3.5 kHz.

Ray model comparison

In spite of the agreement reported above between theory and experiment a comparison with the position of the focal spot F_{ext} predicted by the ray theory Eq. (2.1.17) must be also performed in order to support that sound focusing is a truly effect produced by the bending of sound waves inside the GRIN lens. As explained in section 2.2, in atomic physics, the effective width and length of the lenses are given as $w_{eff} = Ma = 20$ cm and $d_{eff} = Na(\sqrt{3}/2)$, respectively. Then, the half-width h is determined from $2h = w_{eff} = 10$ cm and the lens thickness d is obtained from $d = d_{eff} + k$, where k is an adjustable parameter used to fit F_{ext} to the

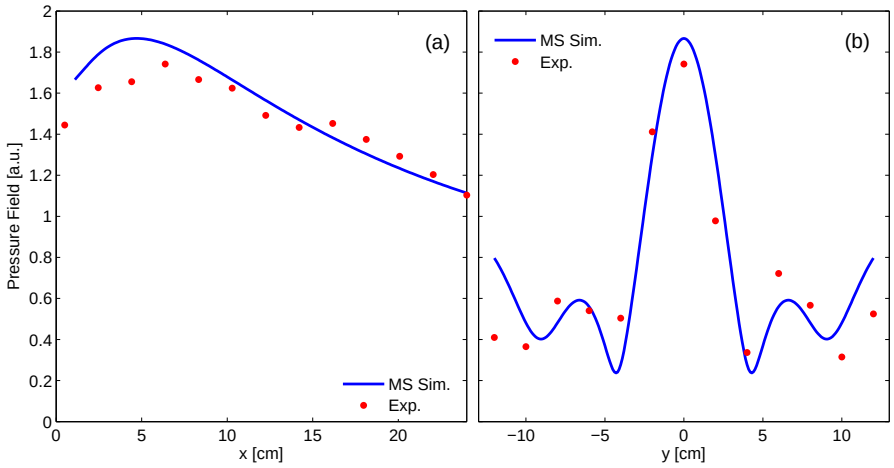

Figure 2.10: Comparison between the Multiple Scattering simulation (blue curve) and the measurements (red dots), for (a) the longitudinal cut and (b) the traversal cut of the the pressure maps in Fig. 2.9 at the focal plane. Both simulations and measurements were made with a $N = 9$ row GRIN PC at a frequency of 4.5 kHz.

data. Note that this procedure is reasonable since the surface of a SC structure is not well defined.

Fig. 2.11 summarized the results obtained for the nine columns GRIN SC lens at two working frequencies under analysis: (a) 3.5 kHz and (b) 4.5 kHz. The values obtained for the adjustable parameter are $k = -0.41$ cm for 3.5 kHz, and $k = -0.28$ cm for 44.5 kHz, which means that the lens surface is nearer to the cylindrical units than that usually employed in atomic physics, where the surface position is taken at a distance above the atoms equal to a half of the lattice parameter; i.e. $k = 0$ in our modeling. The results show that a fairly good agreement is obtained for the thicker lenses, $N > 5$, and for the large frequency, 4.5 kHz.

Data and numerical simulations show a better agreement with the ray model when: i) the frequency operation is near the homogenization limit and ii) for the thicker lens. These conclusions are physically intuitive.

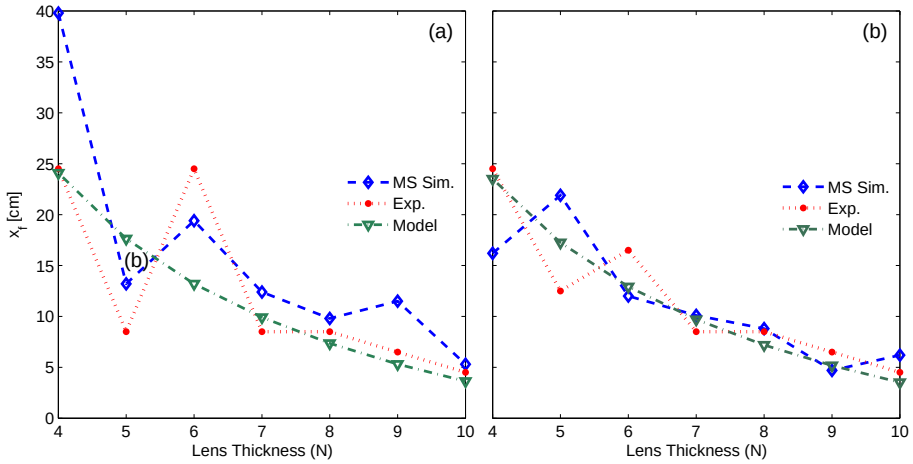

Figure 2.11: Behavior of the position of the focal spot as a function of the lens thickness. The position F_{ext} have been calculated by a ray model (green doted curve) and the multiple scattering method (blue curve). The red dots represent the data for (a) 3.5 kHz, and (b) 4.5 kHz.

On the one hand, for large wavelengths the homogenization in the SC cluster averages several cells of the lattice and, as a consequence, the locally designed refractive index profile n(y) is partially destroyed. On the second hand, for thicker lenses the sound travels along larger lengths and the lens surfaces are also better defined. The combination of these two effects produces a better agreement with the predictions made by the ray model.

Geometry modifications

As an additionally result, the geometry of the lens has been modified to compare its behavior. The first layer of the lens (in our case is the layer positioned at $x = 0$, the rightmost layer) can have an odd number or an even number of cylinders. Fig. 2.12 shows the pressure maps obtained by the multiple scattering simulation. The frequency was established at 4.3 kHz, the cut-off of the Homogenization limit. Three different samples were studied, with 4, 7 and 9 layers. The left (a) and right (b) panels show

the simulations result of a lens beginning with an even and odd number of cylinders, respectively. There can be seen that the samples beginning with odd layers have greater amplitude than the one beginning with an even number. This effect is amplified when the lens grows in number of layers. This is behavior is produced by border effects on the lens. The contribution is greater in the case of the lens beginning with odd layers, because corners are smoother than those of the other cases.

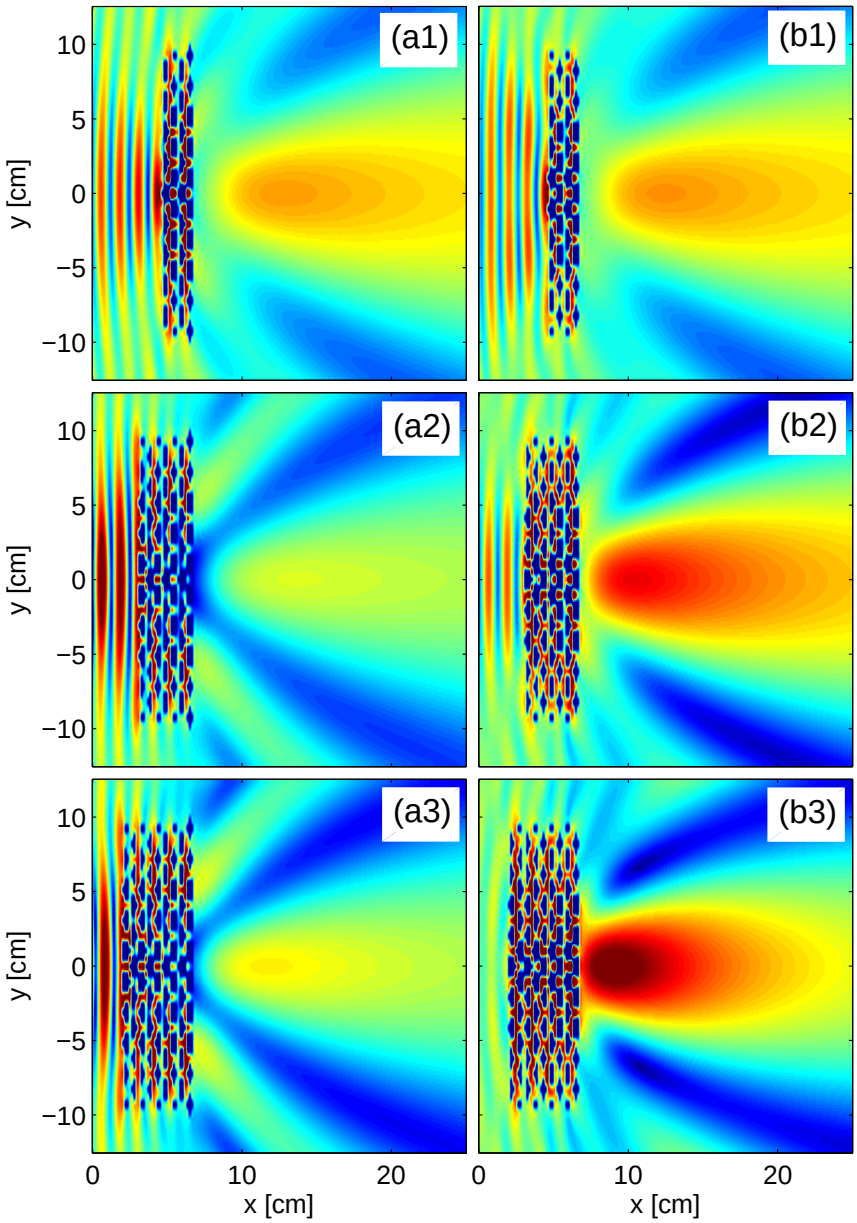

Figure 2.12: Total pressure maps (amplitude) generated by a sound wave of 4.3 kHz impinging a 2D GRIN SC lens with $N = 4$ (a1,b1), $N = 7$ (a2,b2) and $N = 9$ (a3,b3) columns thick. The left and right panels show the results of the numerical simulations of a lens beginning with an even and odd number of cylinders, respectively.

Chapter 3

Acoustic black hole

In this chapter, an omnidirectional acoustic absorber, here named "acoustic black hole" (ABH) is presented. It is based on a previous work done in electromagnetism by Narimanov and Kildishev [30, 52], who proposed a structure consisting of a symmetric shell designed to bend the light rays towards the center where an inner core perfectly absorbs the focused energy. Here, its acoustic counterpart is theoretically proposed, designed and implemented using a cylindrical gradient index lens based on SC. Experimental measurements are presented and discussed.

3.1 Introduction

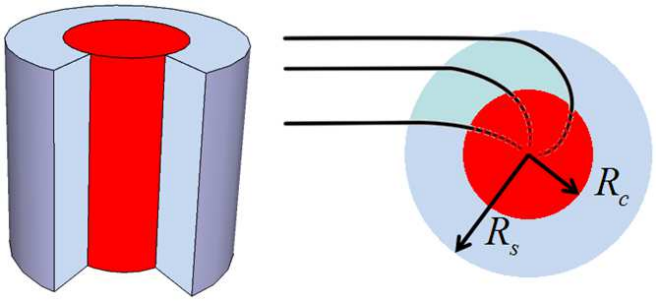

Figure 3.1: Scheme of the acoustic black hole

Fig. 3.1(a) shows an scheme of the 2D acoustic black hole. It consists of a cylindrically symmetric shell, with a radial variation of the acoustic refractive index $n(r)$, and an inner core, where the acoustic energy is dissipated. The shell is a GRIN lens with $n(r)$ matching the index of the outer medium (air) and the internal core, respectively. Thus, the shell guides the energy sound to the inner core where it is dissipated by the designed core. Fig. 3.1(b) shows the path trajectory that the rays follow inside the structure.

The radial dependence of $n(r)$ has been obtained using the mapping existing between the EM and acoustic parameters for waves propagating in a two dimensional space. So, it is possible to translate the solution found for EM waves into the acoustic domain, leading to the following radially dependent index

$$n(r) = \begin{cases} n_b & R_s < r \\ \frac{R_s}{r} n_b & R_c < r < R_s \\ n_c + i\gamma & r < R_c \end{cases}, \tag{3.1.1}$$

where R_c and R_s are the radius of the core and the shell, respectively. They are related through $R_s = R_c(n_c/n_b)$, n_b being the refractive index of air, n_c the real part of the refractive index of the core material and γ is a parameter representing the absorptive properties of the core.

To prove our hypothesis that the black hole effect can be reproduced in the acoustic regime, finite element simulations has been performed used a COMSOL. The parameters used for the simulation are the following. The ABH consists of a core and a shell with $R_c = 60$ mm and $R_s = 126$ mm, respectively. The core refractive index is $n_c = 2.1$ and the shell refractive index variates along the radial position following Eq. (3.1.1). All the structure is embedded in air. To ensure that the acoustic impedance is perfectly matched, the mass density is equal on the three media ($\rho_c = \rho_s = \rho_b = 1.25\text{kg/m}^3$). Finally, the sound speed inside the core is $c_c = c_b/n_c - 2000i$, where the imaginary term introduces the absorption of the core. The structure is excited with an narrow width acoustic Gaussian beam with a wavelength $\lambda = 3$ mm.

Fig. 3.2 shows the modulus of the pressure obtained from the simulations. The beam impinges the shells at its edge and the wave front starts to bend due to the gradient index. The sound travels through the shell and eventually some part of the wave hits the core and is absorbed. The other part is either trapped in the black hole like falling spiral or follows a parabolic "escape" trajectory exiting the acoustic black hole. It is important to note the reflection observed near the impact zone of the wave against the core. Although it seemed that the core and the shell were perfectly matched in terms of acoustic impedance and refractive index, the imaginary part of the sound speed introduces the mismatch explaining the reflection.

3.2 Design and implementation as a SC

The ABH is separated in two different parts, the shell and the core. The core is defined as a cylinder of radius $R_{core} = 80$ mm and a refractive index $n_{core} = 1.5$. This value is chosen, because, as explained in section 1.7 and seen in Fig. 1.11, the effective refractive index changes rapidly with values greater than $n_{eff} > 1.5$. On the other hand, the shell is implemented as a 2D sonic crystal, due to the difficulty of fabricating a material with a continuous variation on the refractive index.

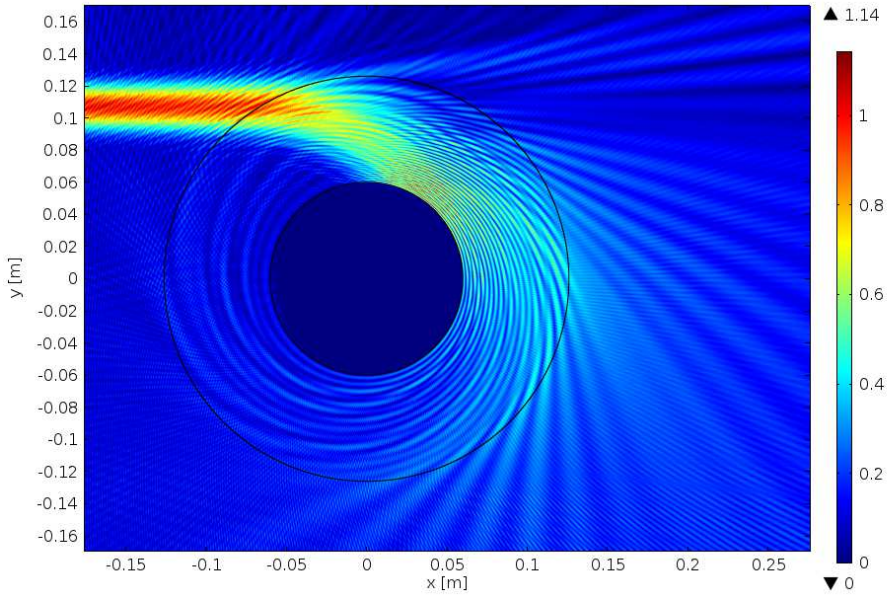

Figure 3.2: Modulus of the pressure obtain from a COMSOL simulation. A Gaussian beam of $\lambda = 3$ mm impinges the upper part of an acoustic black hole with $R_{core} = 60$ mm and $n_c = 2.1$. The three regions (background, shell and core) have the same mas density ($\rho = 1.25\text{kg/m}^3$) and the refractive index of each region follows Eq. (3.1.1). The sound speed inside the core is $c_c = c_b/n_c - 2000i$, where the imaginary term introduces the absorption of the core.

This procedure was also used in section 2.2. The background fluid is air with a refractive index $n_b = 1$. Therefore, the shell has a radius $R_s = R_c(n_c/n_b) = 120$ mm

3.2.1 Outer shell

Figure 3.3 shows a scheme of the structure. The shell is made of a circular cluster of cylinders distributed in an hexagonal lattice with lattice parameter $a = 7.5$ mm. It is constructed with a 3D prototyping machine, so the cylinders are made of a plastic material (ABS), which can be considered acoustically rigid in the air background due to the high

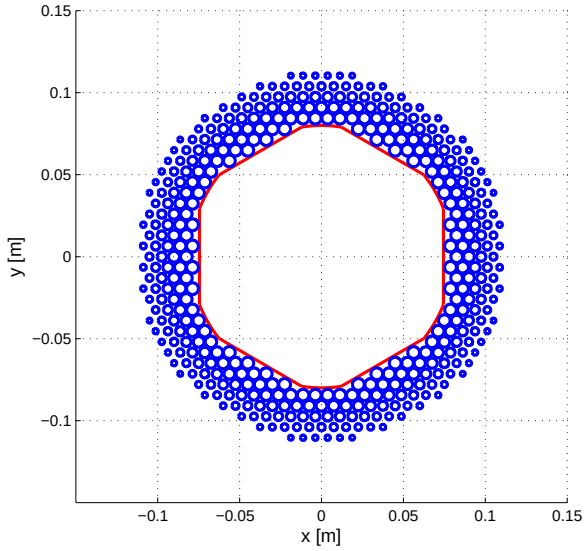

Figure 3.3: Scheme of the ABH as a SC. The outer shell is made of cylinders whose diameters increase with decreasing distance to the center, while the core is defined within the red region.

impedance mismatch between these two media. The shell is designed with five concentric layers with acoustic properties changing from the inner layer (the one closer to the core) to the outer layer. The radius of the cylinders in each layer is properly determined to obtain the required local dependence of $n(r)$ given by Eq. 3.1.1.

Figure 3.4 shows the variation of the acoustic impedance (blue curve) and the refractive index (red curve) along the radial position. Notice the increment of both values as they approach the core having a maximum value of $Z_{max} = 4200$ rayls and $n_{max} = 1.5$. These effective parameters have been calculated using Eq. (2.2.1) and (2.2.2).

Simulations

To test if the implementation as a sonic crystal works, multiple scattering simulations are performed (see section 1.3). The values of velocity and

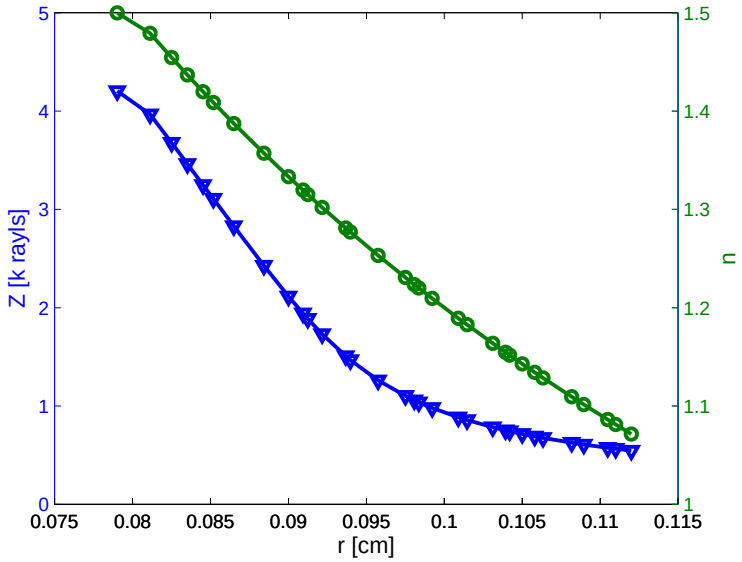

Figure 3.4: Acoustic impedance (blue curve) and refractive index (green curve) of the designed black hole shell.

mass density of the core have been taken from the effective parameters of the closest shell cylinder, giving the values of $c_{core} = 231.33$ m/s and $\rho_{core} = 18.16$ kg/m^3. The absorption of the core is defined as $\gamma = 0.3$.

To evaluate the absorption, we calculate the energy flux (Φ) introduced in section 1.6. The energy flux in this case can also be considered as an intensity loss. There are no sources inside the boundary Ω, so any change in the energy flux is due to the absorption. The intensity loss of the ABH is compared with that of a solid cylinder with the same acoustic properties of the core, but having a radius R_{shell}.

In brief, a 2D sound wave with a plane wavefront impinges the structure from left to right and a pressure map and the intensity loss are calculated. The frequencies analyzed are from 1 kHz up to 10 kHz in steps of 200 Hz. Figure 3.5 shows the results of the intensity loss produced by the ABH (blue continuous line) and by the solid absorbing cylinder (red dashed curve). Note that up to the frequency of 5 kHz, the structure is

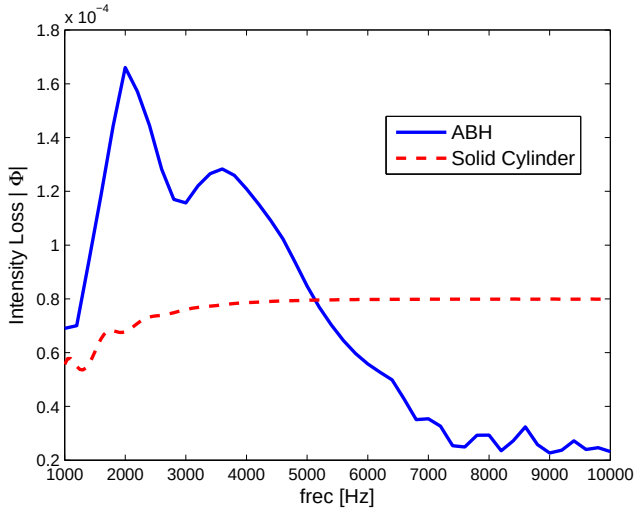

Figure 3.5: Intensity loss produced by the ABH (blue continuous line) with $R_{shell} = 120$ mm and a solid cylinder of radius $R_{cyl} = 120$ mm made of the designed absorbing material (red dashed line).

absorbing more energy, having two peaks around 2.0 kHz and 3.6 kHz which correspond to Fabry Pérot modes of the structure.

Figures 3.6(a) and 3.6(b) show the modulus of the pressure map produced by solid cylinder and the black hole structure, respectively, at the frequencies of 2.0 kHz (left panels) and 3.6 kHz (right panels) corresponding to the peaks in Fig. 3.5. It is seen that the ABH concentrates the energy in the core due to the bending effect, and that has lower reflectance due the impedance matching, thus achieving more absorption that the solid absorbing cylinder. The physical explanation of the difference of absorption between both configurations is intuitive: More energy is absorbed when more energy enters into the core. From this simulation, one concludes that, the shell has two main purposes: 1) matches the background acoustic properties with the ones of the core and, 2), bends the waves towards the core.

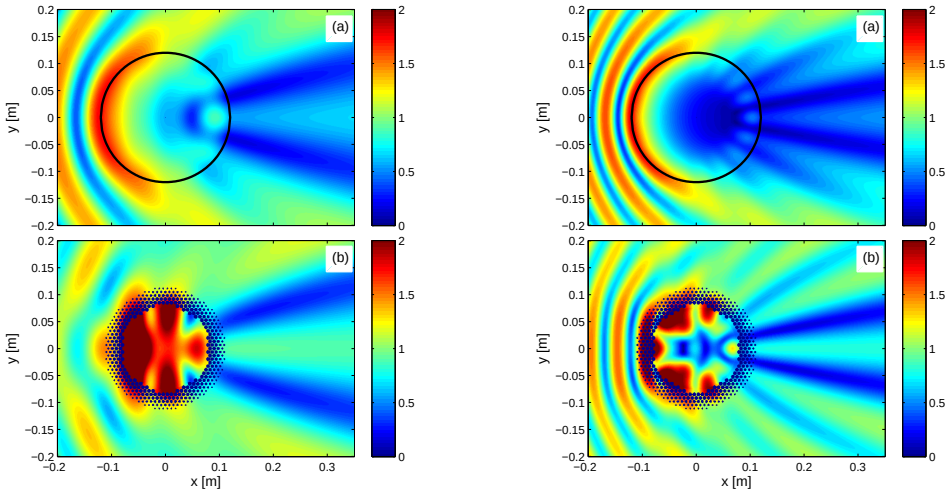

Figure 3.6: Modulus of the pressure map of (a) the solid cylinder and (b) the ABH at 2.0 kHz (left panels) and at 3.6 kHz (right panels)

3.2.2 Inner core

To implement the core, two different approaches were followed. In the first one, eight different samples, made of existing absorbing materials were characterized and their acoustic properties obtained as function of the frequency. From the experimental results, which are explained later on, we follow the second approach. Here, a metamaterial core was designed as a sonic crystal with optimal acoustic parameters to maximize the absorptive performance.

Cores existing in nature

As a first approach, eight different materials are chosen as cores. These samples has been clasified in two categories, soft and hard materials. The soft materials include three types of "Supreem" Foams (SF) and one type of Fiber Glass (FG). The hard materials comprise three types of Expanded Polystyrene (EPS) and two types of Polyurethane (PUR). The eight samples has been characterized in a impedance tube with the four microphones method described in the Appendix B.

Table 3.2.1: Values of the characteristic impedance (Z) and the refractive index (n) of the eight samples made of existing absorbing materials in the frequency range from 580 Hz up to 3.4 kHz

Soft samples	Z rayls	n	Hard samples	Z rayls	n
SF-1	450 ± 20	1.12 ± 0.02	PUR-1	1780 ± 600	3.60 ± 0.20
SF-2	520 ± 20	1.34 ± 0.03	PUR-2	2370 ± 800	3.67 ± 0.25
SF-3	540 ± 40	1.43 ± 0.07	EPS-1	3530 ± 2200	5.61 ± 0.48
FG	470 ± 40	1.19 ± 0.06	EPS-2	3680 ± 1900	1.48 ± 0.28
			EPS-3	5600 ± 3100	2.47 ± 0.71

The range of values of the complex refractive index and the acoustic impedance of the eight samples are experimentally obtained for frequencies from 580 [Hz] up to 3.4 kHz. Table 3.2.1 summarizes these results.

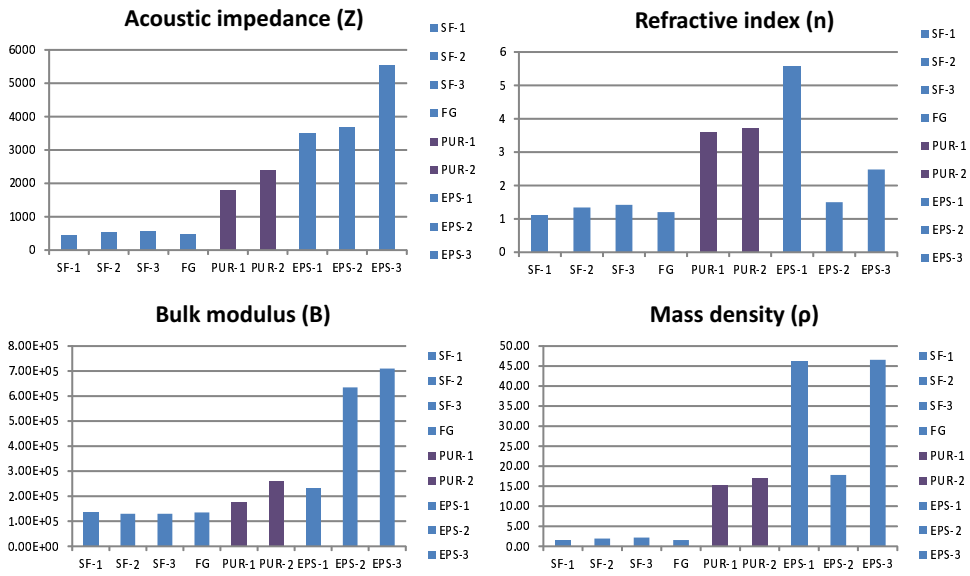

Figure 3.7: Graphs of the characteristic acoustic impedance (Z), the refractive index (n), the bulk modulus (B) and the mass density (ρ) of the eight samples here analyzed (see text).

To compare these materials, Fig. 3.7(a-d) shows the mean values of the characteristic acoustic impedance, the refractive index, the bulk modulus and the mass density, respectively, of the eight in nature existing samples. Notice that the samples are sorted with increasing impedance.

As is expected the acoustic impedance from the soft materials is smaller than the one of the hard materials. The soft materials are almost matched to air ($Z_{air} = 433$ rayls and $n_{air} = 1$) and seem to be very similar, but later on, results will show some differences between them.

The PUR materials have a low impedance, for being hard materials, but a very high refractive index. The compressibility modulus (or bulk modulus) of these materials is also very similar to the one of air, but in comparison they have a very high mass density.

The EPS materials deserve a brief explanation of their special properties. While EPS-1 and EPS-2 have almost the same impedance, much lower than the one of EPS-3; EPS-1 has a very high refractive index in comparison to EPS-2 and EPS-3. Notice also, that the properties of EPS-2 are closer to the inner most layer of the shell, $Z_{max} = 4200$ [rayls] and $n_{max} = 1.5$ (see Fig. 3.4). Finally, it worth to mention, that EPS-1 has almost the same bulk modulus as the PUR materials, while EPS-2 has almost the same mass density.

Later on, the characterization of these materials will be very useful to understand the measurements obtained once these cores are inserted inside the designed shell.

Metamaterial core

The metamaterial core (MMC) consists of a cluster of cylinders with equal diameters distributed in a hexagonal lattice with a high filling fraction to produce dissipation by friction. The hexagonal lattice has been chosen because it can achieve higher filling fractions than the square one. The radius of these cylinders coincides with the ones of the inner layer cylinders of the shell. This ensures that the matching of acoustic impedances between background and the core is also obtained.

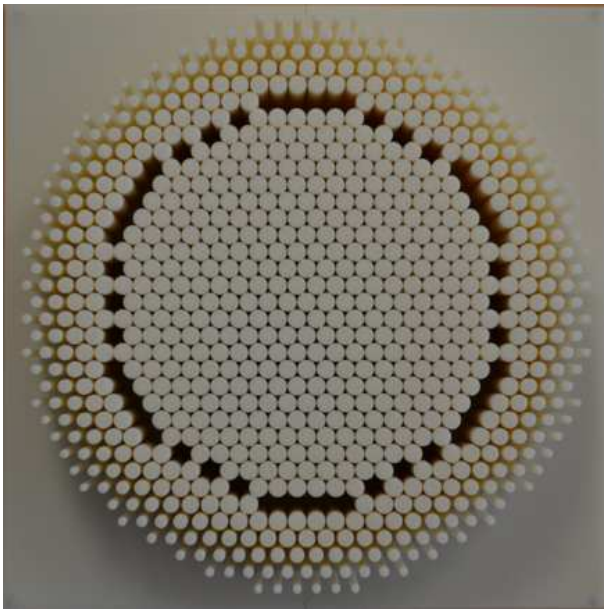

Figure 3.8: Photograph of the fabricated structure. The outer shell is made of cylinders whose diameters increase with decreasing distance to the center. The inner core is made of identical cylinders in a hexagonal lattice with about 84% of filling fraction.

Figure 3.8 shows a photo of the sonic crystal shell and the metamaterial core. Both have been fabricated using the 3D prototyping machine. The MMC is made of cylinders with equal diameter $d_c = 7.2$ mm. Its effective refractive index is $n_c = 1.5$ and the corresponding hexagonal lattice has a filling fraction $f_{hex} = \frac{\pi}{2\sqrt{3}}(\frac{d_c}{a})^2 = 83.6\%$. Note that this fraction of volume occupied by the sound scatterers is near to that corresponding to the close-packing (CP) condition, where $d = a$ and, therefore, $f_{hex}^{CP} = \pi/(2\sqrt{3}) = 90.6\%$. Consequently, the air is forced to pass through the narrow channels left between cylinders. The acoustic energy is strongly dissipated by friction and introduces an imaginary part, γ, in $n(r)$.

3.3 Experimental setup: Multi-modal impedance chamber

The Multi-modal impedance chamber (MMIC) is a homemade experimental setup which is based on the impedance tube and the four microphones method described in the Appendix B.

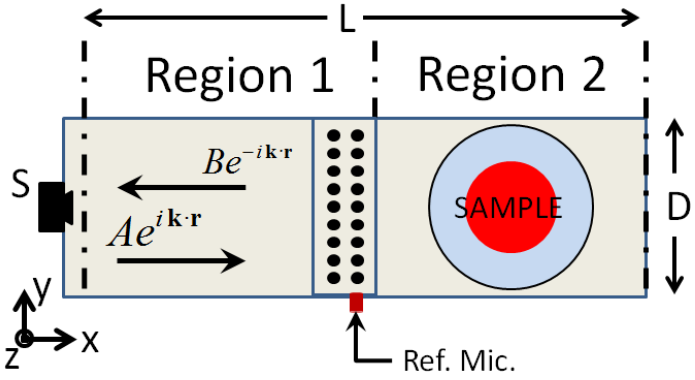

Figure 3.9: Scheme of the multi-modal impedance chamber. The chamber has a width $D = 30$ cm, a length $L = 150$ cm and height $H = 5$ cm. The speaker (S) at the left excites an acoustic flow represented by coefficients A, while the back-scattered flow is given by coefficients B. Black dots define the 9 pairs of microphones used to record the signal. Another microphone (Ref. Mic.) is employed as the reference. The sample is placed in the right hand side region, which is accessible by a removable tap.

Let's consider the rectangular waveguide depicted in Fig. 3.9, where $D = 30$ cm and $H = 5$ cm. The total length is $L = 150$ cm and is closed on both sides. The chamber is filled with air and is made of aluminum 1 cm thick. Due to the high mismatch of impedance, the walls can be considered rigid. A speaker located at the chamber's left side excites a sound field that propagates along the positive x-axis. This sound field leaves Region 1 and enters into Region 2 where interacts with the sample and it is reflected at the chamber's right end. Therefore, in principle, we

assume that all the energy dissipated during the process is absorbed by the sample. By properly measuring the sound field, the dissipated energy can be estimated, and therefore characterize the absorbing efficiency of the structure.

The pressure field P in the resonant chamber can be represented as a linear combination of plane waves propagating along the x-axis. Moreover, since we consider that the chamber behaves as a waveguide with rectangular section and rigid walls, in principle, all the modes in the YZ plane must be also taken into account. Applying boundary conditions, and considering propagation in the x-direction, the pressure field of the (m,n)-mode inside the chamber is described by

$$P_{m,n}(x,y,z) = \left[A_{m,n}e^{ik_x x} + B_{m,n}e^{-ik_x x}\right]\left[\cos\left(\frac{m\pi}{D}y\right)\cos\left(\frac{n\pi}{H}z\right)\right], \tag{3.3.1}$$

where

$$k^2 = \left(\frac{\omega}{c_b}\right)^2 = k_x^2 + \left(\frac{m\pi}{D}\right)^2 + \left(\frac{n\pi}{H}\right)^2, \tag{3.3.2}$$

c_b is the speed of sound in air and $\omega = 2\pi f$ is the angular frequency. Then, the cut-off frequencies $f_{m,n}$ can be derived from Eq. (3.3.2) as

$$f_{m,n} = \left(\frac{c_b}{2\pi}\right)^2\left[\left(\frac{m\pi}{D}\right)^2 + \left(\frac{n\pi}{H}\right)^2\right]. \tag{3.3.3}$$

For frequencies below $f_{0,1} = f_{6,0} = 3470$ Hz, the chamber is considered mono-mode in the z-direction. Working under this premise, Eq. (3.3.1) can be cast in

$$P(x,y) = \sum_{m=0}^{\infty}\left[A_m e^{i\beta_m x} + B_m e^{-i\beta_m x}\right]\cos\left(\frac{m\pi}{D}y\right), \tag{3.3.4}$$

where

$$\beta_m = \sqrt{\left(\frac{\omega}{c_b}\right)^2 - \left(\frac{m\pi}{D}\right)^2}. \tag{3.3.5}$$

Though the summation is infinite, as we increase m the propagation constant β_m becomes complex and the waves are evanescent; the contribution of these modes to P is negligible and, therefore, P only depends on a few number of coefficients A_m and B_m. In our case, bellow $f_{0,1}$ there are only six propagating modes and therefore twelve constants need to be determined from the measurements inside the multi-modal impedance chamber.

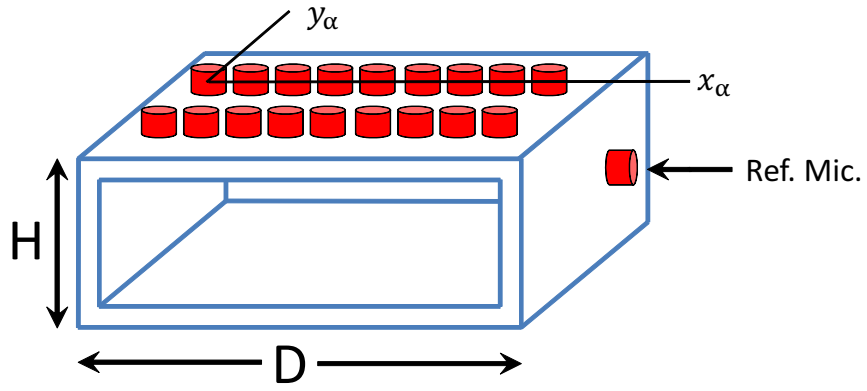

Figure 3.10: Scheme of position of the microphones.

Figure 3.10 shows a 3D representation of the microphones depicted in Fig. 3.9. Nine pairs of microphones are employed at selected positions (x_α, y_α) in the chamber. The pairs of microphones are located along the y-axis separated 3 cm. On the other hand, the microphones of each pair are oriented along the x-axis and separated 3.5 cm. This separation sets, through Nyquist theorem, the minimum wavelength $\lambda = 7$ cm, or $f_{ny} = 4960$ Hz, that can be measured without error. This frequency is much larger than the one established by the mono-mode propagation along the z-axis.

Each microphone is inserted from above, without entering the cavity of the chamber, but is flushed to the inner surface. An additional microphone is used as a reference (Ref. Mic. in Fig. 3.10). It is inserted through one side of the chamber at position (x_0, y_0) and at the height

$H/2$. This microphone is also flushed to the inner wall.

The chamber is excited with the speaker by injecting an Additive White Gaussian Noise (AWGN). The choice of this type of signal makes possible to measure a large bandwidth in one go. The drawback of this method is that it makes impossible to obtain the pressure values directly, because the input signal is non-deterministic. Let's define the pressure in each microphone position as P_α, and P_0 for the case of the reference one. Then, instead of obtaining the pressure, the microphones measure the transfer function $H_{0\alpha} = S_{0\alpha}/S_{00}$, where $S_{0\alpha} = P_\alpha P_0^*$ is the cross-spectrum between the signal of the α-microphone and the reference and $S_{00} = P_0 P_0^*$ is the auto-spectrum of the reference one. Therefore, the reference microphone is used to get information of the phase.

Then, we obtain instead the coefficients A_m/P_0 and B_m/P_0 by solving the following linear system of equations

$$H_{0\alpha} = \frac{P_\alpha}{P_0} = \sum_{m=0}^{M} \left[\frac{A_m}{P_0} e^{i\beta_m x_\alpha} + \frac{B_m}{P_0} e^{-i\beta_m x_\alpha} \right] \cos\left(\frac{m\pi}{D} y_\alpha\right). \tag{3.3.6}$$

Note that we can determine the coefficients only relative to the pressure field at the reference position, that is, A_m/P_0 and B_m/P_0. However these quantities still allow us to obtain the reflectance in Region 1, since this reflectance is given by the ratio of the energy (or energy flux) that leaves that region Φ_B by the energy that enters it Φ_A. These are obtained by integrating the acoustic intensity across the chamber cross section (the area being $D \times H$), as

$$\Phi_A = \frac{DH}{4\omega\rho_b} S_{00} \sum_{m=0}^{M} \beta_m \frac{|A_m|^2}{|P_0|^2}, \tag{3.3.7}$$

$$\Phi_B = \frac{DH}{4\omega\rho_b} S_{00} \sum_{m=0}^{M} \beta_m \frac{|B_m|^2}{|P_0|^2}. \tag{3.3.8}$$

Note that $S_{00} = |P_0|^2$. Finally, the reflectance is obtained from $\mathcal{R} = \Phi_B/\Phi_A$ and it is independent of any multiplicative factor appearing in the coefficients. Finally, the energy absorbed by the sample is

$$\alpha = 1 - \mathcal{R}. \tag{3.3.9}$$

Calibration

As explained previously, the system relays on the difference between measurements in each microphone, so it is important to calibrate them. Let us define the transfer function $H_i^{(M)}(f)$ of the microphone M_i as

$$V(f) = H_i^{(M)}(f)P(f), \tag{3.3.10}$$

where $P(f)$ is the measured pressure and $V(f)$ is the given electric voltage. All values are in function of the frequency f. Then, let's consider two microphones M_1 and M_2 located at different position α and β, respectively. By taking data, interchanging the position and measuring again, we obtain the following equations

$$\begin{array}{ll} V_0 = P_0 H_0^{(M)} \\ V_1 = P_1 H_1^{(M)} \end{array} \quad \text{and} \quad \begin{array}{ll} V_0' = P_0 H_1^{(M)} \\ V_1' = P_1 H_0^{(M)}. \end{array} \tag{3.3.11}$$

Note that, although measures where taken in the same place, two different values of electric voltage $V_1 \neq V_1'$ where obtained. This is due to the different transfer function of each microphone. From this measures it is possible to obtain the calibration constant as

$$K_{10} = \sqrt{\frac{V_1}{V_0}\frac{V_0'}{V_1'}} = \frac{H_1^{(M)}}{H_0^{(M)}}, \tag{3.3.12}$$

which is a complex number. Then the calibrated values can be obtained from

$$\left(\frac{V_1}{V_0}\right)_{calib} = \frac{V_1}{V_0}\frac{1}{K_{10}} = \frac{P_1}{P_0}. \tag{3.3.13}$$

Note that the relationship between the electric voltages and the pressures is the same. Additionally, this procedure can be expanded for the case of

three or more microphones. More information on this topic can be found in [31]

Experimental test

To prove the efficiency of the experimental setup, the absorption produced by two samples of material SF-2 has been measured in the commercial impedance tube (CIT) and in the MMIC. Both samples have a length of $\ell = 7.7$ cm and fill the whole medium in which they are inserted. The sample of the tube is a cylinder with a diameter of $d = 3.5$ cm, while the sample of the chamber is a prism with a width of $d = D$ and a height of $h = H$.

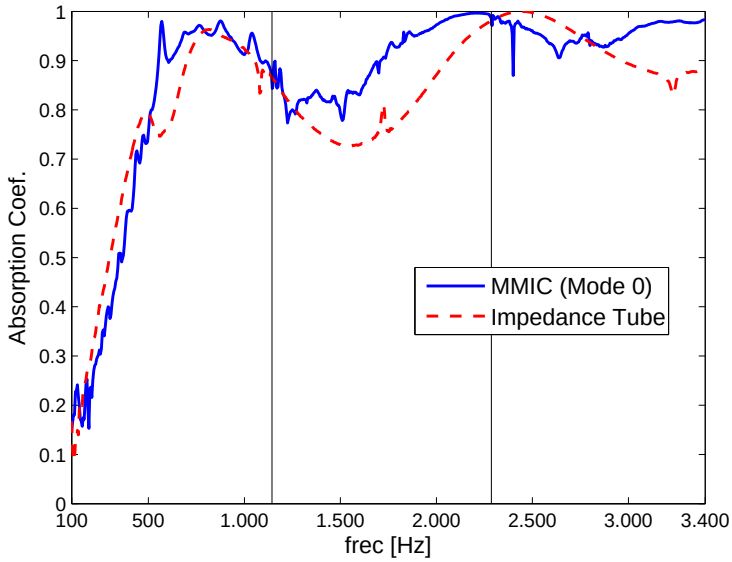

Figure 3.11: Absorption coefficient produced by the fundamental mode of a reference sample measured in a commercial Impedance Tube (red dashed line) and the one measured with the MMIC developed for this work (blue continuous line). The vertical lines are guides for the eye and define the onset of modes $m = 2$ and $m = 4$.

Measurements have been performed for the two samples. The fre-

quency region analyzed is from 100 Hz up to 3400 Hz. In the case of the CIT only one mode is propagating, but in the MMIC the analyzed region allows the propagation of modes $m = 0$ to $m = 5$. To be able to compare them, the absorption coefficient of the MMIC has been calculated by taking into account only the fundamental mode ($m = 0$). Since this mode has no variation in the y-axis the absorption does not depend on the samples width. The mono-mode absorption coefficient is calculated as $\alpha_0 = 1 - B_0/A_0$.

Figure 3.11 shows the results of both experiments. The blue continuous and the red dashed curves show the absorption coefficient acquired by measuring the sample in the commercial impedance tube and the MMIC, respectively. The vertical black lines lines define the frequencies at which the second ($f_2 = 1143.33$ Hz) and the forth ($f_4 = 2286.66$ Hz) modes along the y-axis start propagating inside the chamber. The two curves show a fairly good agreement. The result obtained from the MMIC considering only the fundamental mode are shifted towards lower frequencies with respect to the one acquired using the CIT. Note that the shifting appears when the second mode stars propagating, $f > f_2$, and is emphasized for frequencies higher than $f > f_4$. This could be due to mode conversion happening inside the sample.

3.4 Results and discussion

Here, the results from the experiments done with the eight natural cores and the metamaterial core are presented and discussed. For comparison purpose, the absorption coefficient produced by the ABH, or the combined structure of shell and core, is compared with the one produced by two cylindrical samples made of the same material as the core, but with different radii. The first one equals the radius of the used core $R_1 = 80$ mm, while the second one has the same radius as the shell $R_2 = 120$ mm. Figure 3.12 shows the three configuration studied, where the absorbing material and the shell are depicted with the red and the blue color, respectively.

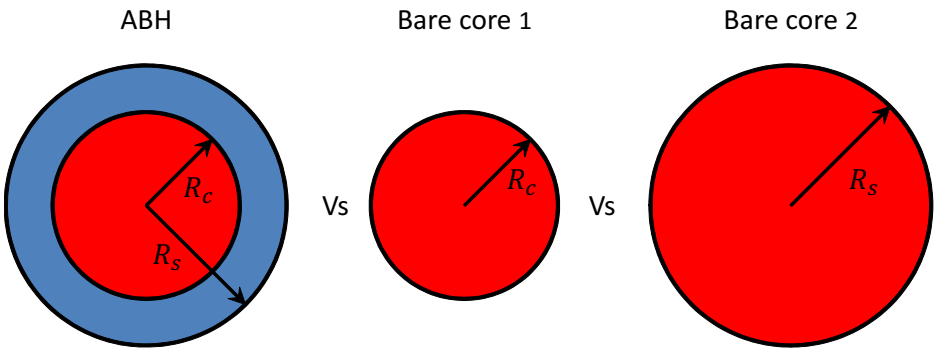

Figure 3.12: Definition of the three configurations used to compare the absorption coefficient

As explained, for frequencies below $f_6 = 3470$ Hz, the chamber is considered mono-mode in the z-direction. Therefore, the range of measured frequencies is from $f_{min} = 100$ Hz up to $f_{max} = 3400$ Hz. The broadband performance of the ABH shell is based on effective medium theory, which is valid for any wavelength large enough to satisfy the homogenization condition, that is $\lambda \geq 4a$. By substituting the value of a, the corresponding frequencies are $f \leq 11430$ Hz which is much higher than the chosen range.

The frequency region analyzed allows the propagation of modes $m = 0$ to $m = 5$. However, due to the symmetry of the chamber and the sample, the odd modes are not excited (their coefficients are negligible) and, consequently, modes m =0, 2, and 4 are the only ones considered. The second mode starts propagating inside the chamber after the cut-off frequency $f_2 = 1143$ Hz and the fourth mode after $f_4 = 2287$ Hz. The contribution of the evanescent modes should be also neglected, but numerical test demonstrate that the algorithm gains stability if the first even evanescent mode, only the reflected one, is also considered. The first incident one has no physic logic and is not counted due its tendency to infinite in Region 1. The coefficients of the modes that are not considered have been set equal to zero.

Finally, although the absorption coefficient, α, has been measured in

the chosen range of frequencies for all the samples, to be able to compare them easily, we introduce the absorption quality factor, Q_α, defined as

$$Q_\alpha \equiv \frac{1}{\Delta f} \int_{f_{min}}^{f_{max}} \alpha\left(f\right) df, \tag{3.4.1}$$

where $\Delta f = f_{max} - f_{min}$ is the bandwidth.

3.4.1 Results for natural existing materials

The eight types of cores implemented with materials existing in nature have been tested in the three possible configurations shown in Fig. 3.12.

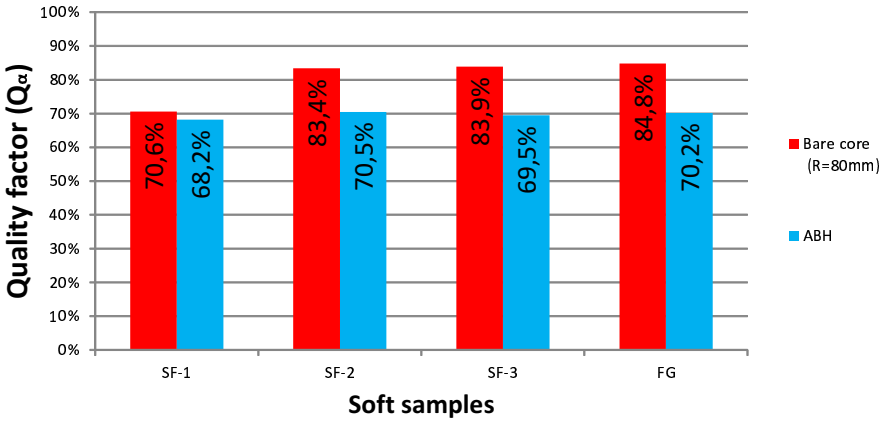

Figure 3.13: Absorptive quality factor Q_α [see Eq. (3.4.1)] of the soft samples analyzed in the two configurations shown in Fig. 3.12, ABH and Bare Core 1.

Figure 3.13 present a graph of the quality factors Q_α obtained for the soft materials. Only the results of the ABH and bare cores with radius R_c are shown. The results of the bare cores with radius R_s are omitted, because the quality factors of the smaller bare cores are bigger than the ones of the ABH configuration. The SF-2 and SF-3 materials are very similar and almost no difference is found in the results.

Although the SF-1 material is the one with acoustic properties similar to air, it presents lower absorption than the others. On the other hand,

the FG material has almost the same acoustic properties as SF-1, but the quality absorption is almost a 14% bigger, in the bare core configuration with R_c.

In general, all the soft material are almost matched to the surrounding air and deliver high quality factors in the bare core configurations. But adding the shell to the soft material decreases the absorption. This effect is produced by the impedance mismatch between the innermost layer of the shell, (see Fig. 3.4 blue curve), and the cores made of soft materials (see Table 3.2.1). Notice the difference of one order of magnitude between the maximum characteristic impedance of the shell $Z_{max} = 4200$ [rayls] and the ones of the soft materials ($Z \in [440 - 550]$ rayls). By the other hand, these materials have approximately the same refractive index ($n \in [1.2 - 1.4]$) as the maximum value of the shell, $n_{max} = 1.5$. From here we conclude, that the matching of impedances is more important than the matching of refractive indexes.

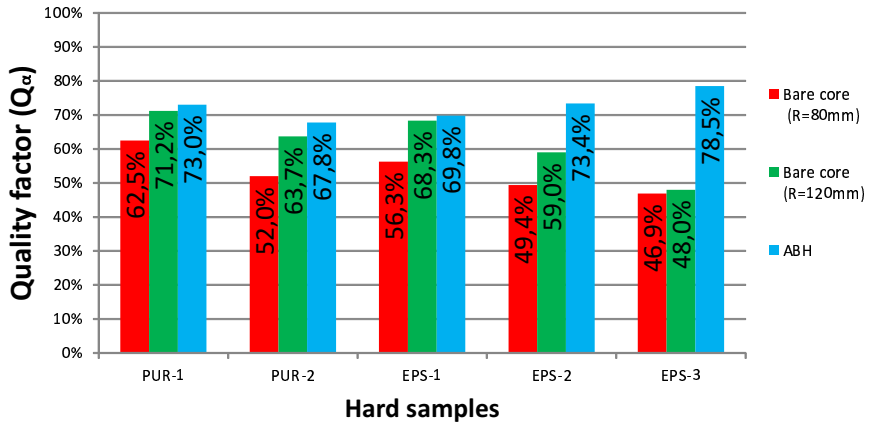

Figure 3.14: Absorptive quality factor Q_α [see Eq. (3.4.1)] of the hard samples analyzed in the three configurations shown in Fig. 3.12. The materials have increasing impedance from left to right (see Table 3.2.1).

Figure 3.14 presents the graph of Q_α obtained for the hard natural materials in the three possible configurations. As expected, the Q_α values obtained in the bare core configurations decreases with increasing

impedance.

In the case of the first three materials (PUR-1, PUR-2 and EPS-1), there is almost no difference between the bare core with R_s and the ABH configurations. Looking back at Fig. 3.7, we notice the mismatch in the bulk modulus (or in the refractive index) between these materials and the goal value established by the shell.

The EPS-2 material is the one that has the acoustic properties more similar to the ones required. Notice an improvement of a 24% and 14% with respect to the bare configuration with R_c and R_s, respectively. In spite of this, EPS-3 provides the highest quality factor in the ABH configuration, with an improvement of 30% in comparison to the other two configurations. In fact, this improvement is due to the low performance of the EPS-3 materials in the two bare core configurations. Notice that increasing the radius of the core from $R_c = 80$ mm to $R_s = 120$ mm results in almost no variation in the quality factor, only a 1%.

In general, the shell with the hard material core has, not only, improved the quality factor of the bare core with R_c, but also surpassed the Q_α of the bare core with R_s. As has been stressed, matching the acoustic impedance improves the quality factor of the ABH, but for a large enhancement of absorption, it is necessary to match the refractive index, too.

Note from Table 3.2.1 that the hard materials have a characteristic acoustic impedance ($Z \in [1780 - 5600]$ rayls) with the same order of magnitude as the maximum one of the shell $Z_{max} = 4200$ rayls. The material EPS-2 is the one with most similar value ($Z_{EPS-2} = 3680$ rayls). In the case of the first three materials, although the impedance is more or less similar, there is almost no improvement. This is caused by the difference between the refractive index of the inner most layer of the shell ($n_{max} = 1.5$) and the one of the cores. In the case of the first three materials, $n > 3.5$, and for the last two samples, $n \approx 1.5$. As expected, both, the refractive index and the characteristic acoustic impedance, have to be matched for the ABH to work properly.

Finally, Figure 3.15 shows the frequency dependence of the absorption

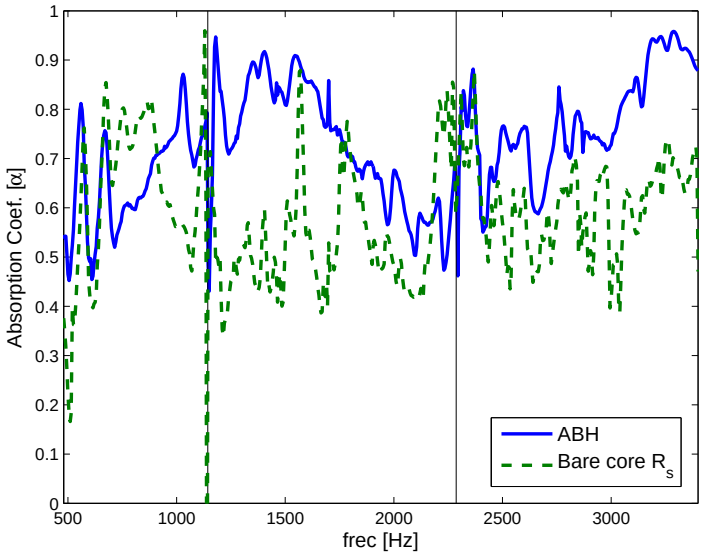

Figure 3.15: Absorption coefficient produced by EPS-2 material in two configurations. The ABH (blue continuous curve) and the bare core configuration with radius R_s (green dashed curve). The vertical lines are guides for the eye and define the cutoffs at which the modes $m = 2$ and $m = 4$, respectively, start propagating inside the chamber.

coefficient α for the ESP-2 sample in two configurations, the ABH and the bare core with the same radius R_s. Note that for almost any frequency the absorption factor is strongly enhanced by using the refractive shell.

3.4.2 Results with the metamaterial core

From the results presented in the previous section, we arrived at the conclusion that, its necessary that, both, the refractive index and the characteristic acoustic impedance, are matched for a good performance of the ABH. Here, we report the measurements using the metamaterial core (MMC), specially designed with these characteristics.

Figure 3.16 shows a graph with the quality factors Q_α experimentally determined for the three possible configurations. It is observed that

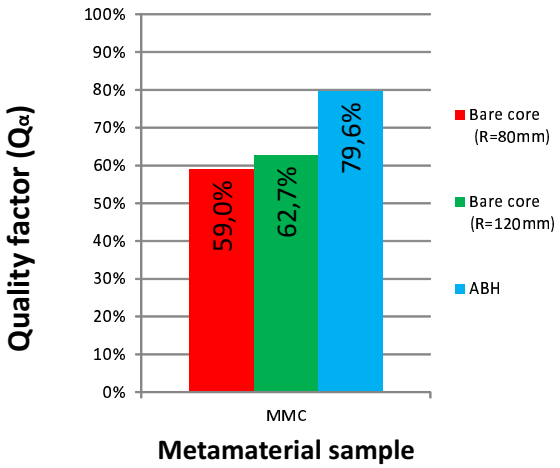

Figure 3.16: Absorptive factor Q_α [see Eq. (3.4.1)] of the metamaterial core analyzed in the three configurations shown in Fig. 3.12.

the MMC behaves like the hard samples in the manner that the ABH configuration provides better results than the other configurations. Also, in a similar way to the EPS-3 material, there is almost no difference in Q_α of the two bare core configurations due to the high impedance of metamaterial.

Notice, that the ABH configuration improves the quality factor, Q_α, a 17% and 10% with respect to the bare core with R_c and R_s, respectively. This result seems to be worst than the one achieved by the EPS-3 material (30% improvement), but this is due to the low value of Q_α obtained in the bare core configuration. Also, in absolute values, Q_α is bigger in the case of the MMC than in the EPS-3 core.

Therefore, the MMC has almost the same acoustic properties than the EPS-2 material, but with a higher impedance. In spite of this, it provides better quality factors in the bare core configurations. Therefore, we could say, that, although been a made of rigid cylinders, the MMC presents more absorption than the EPS-2 material. The losses introduced by friction adding to the combined effect of the black hole shell, show results almost as good as the ones obtained by the soft materials, which

are commonly used as absorbing materials.

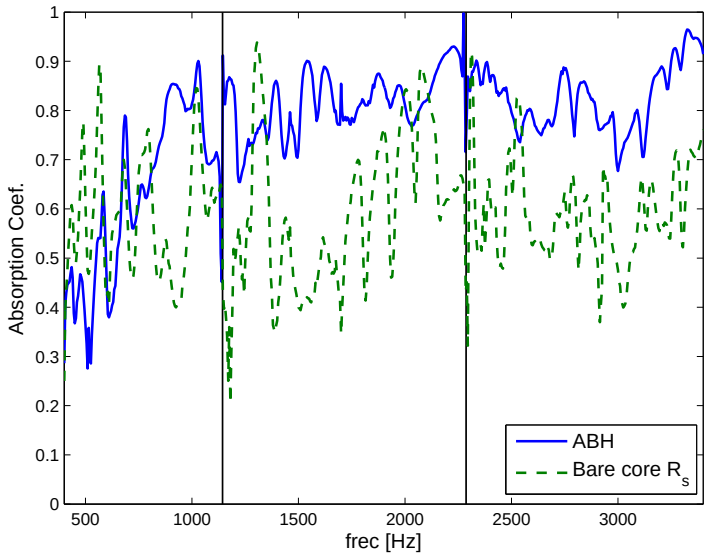

Figure 3.17: Absorption produced by the ABH configuration (blue continuous line) and by the metamaterial core (green dashed line). The vertical lines are guides for the eye and define the cutoffs at which the modes $m = 2$ and $m = 4$, respectively, start propagating inside the chamber.

Figure 3.17 shows the frequency dependence of α for the metamaterial core (blue continuous line) and for the ABH configuration (green dashed line). Note that for almost any frequency the absorption of the bare core 2, with the same dimension than the ABH, is enhanced when the ABH is considered, demonstrating the performance of the acoustic black hole.

In comparison with the data shown in Fig. 3.15 for the EPS-2 absorbing material, the MMC provides a larger enchancement of Q_α in the range from $f = 1750$ Hz up to $f = 3000$ Hz.

Part II

Vibrations

Chapter 1

Theoretical introduction

This chapter introduces the basic theory needed to understand the following chapters. Concepts like strain and stress, the material's properties Poisson ratio, Young Modulus and mass density and the relationship they have with the dynamics of elastic materials will be explained. Additionally, the Euler-Bernoulli beam equation of motion and the Kirchhoff-Love plate equation of motion will be derived, an example of solution for both systems will be given and the boundary conditions for different systems will be explained.

The systems used throughout this work are considered one dimensional (1D) or two dimensional (2D), so the theory will be explained from a 2D point of view. Then, from that point it's easy to particularize for the 1D systems. Also, in the scope of this work, we consider isotropic homogeneous materials, although the resulting metamaterial will be anisotropic and inhomogeneous.

1.1 Stress and Strain

Strain and stress make reference to the ratio of deformation that a material suffers and the force that its applied to create this deformation. For two-dimensional systems, we find two different strains and stresses, which may be classified as 'normal' and 'shear' (i.e. acting perpendicular to or along the face of an element respectively).

For explaining the concept of strain, let's consider the 2D infinitesimal rectangular material element with dimensions $dx \times dy$ shown in Fig 1.1 , which after deformation, takes the form of a rhombus.

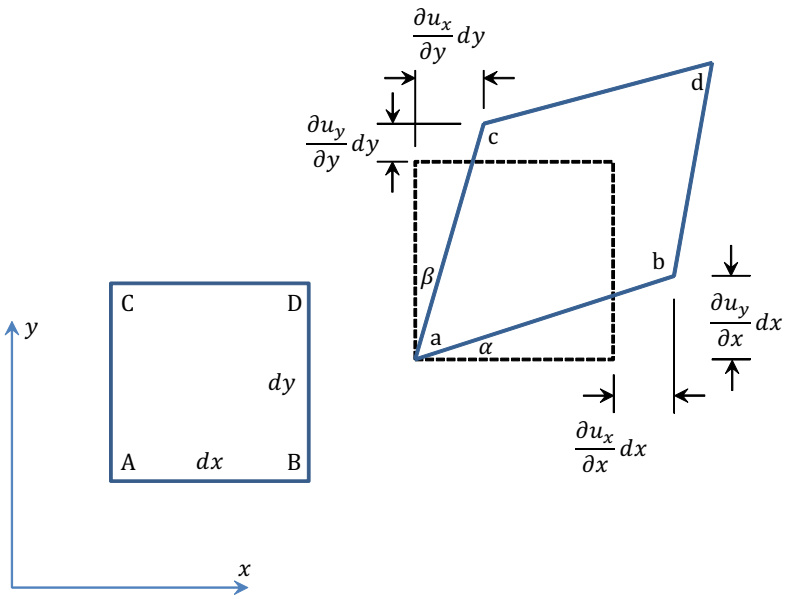

Figure 1.1: Strain: Neutral and flexed states of a square plate.

The normal strain in the x-direction, ε_{xx}, is expressed as the ratio of total deformation L_{ab} to the initial dimension L_{AB}. The normal strain is positive if the material fibers are stretched and negative if they are compressed. On the other hand, the shear strain γ_{xy} is defined as the change in angle between lines $\overline{AC}$ and $\overline{AB}$. Therefore,

$$\varepsilon_{xx} = \frac{L_{ab} - L_{AB}}{L_{AB}} = \frac{\partial u_x}{\partial x}, \tag{1.1.1}$$

$$\gamma_{xy} = \alpha + \beta = \frac{\partial u_y}{\partial x} + \frac{\partial u_x}{\partial y} = \gamma_{yx}, \tag{1.1.2}$$

where, for small deformations and rotations, the lengths and angles are

$$L_{AB} = dx, \tag{1.1.3a}$$

$$Lab = \sqrt{\left(dx + \frac{\partial u_x}{\partial x}dx\right)^2 + \left(\frac{\partial u_y}{\partial x}dx\right)^2} \approx dx + \frac{\partial u_x}{\partial x}dx, \tag{1.1.3b}$$

$$\alpha = \arctan \frac{\frac{\partial u_y}{\partial x}dx}{dx + \frac{\partial u_x}{\partial x}dx} \approx \frac{\partial u_y}{\partial x}, \tag{1.1.3c}$$

$$\beta = \arctan \frac{\frac{\partial u_x}{\partial y}dy}{dy + \frac{\partial u_y}{\partial y}dy} \approx \frac{\partial u_x}{\partial y}. \tag{1.1.3d}$$

In addition, there exists a relationship between the normal stresses of different faces. It is known that, when a materials suffers compressional force on one pair of faces, this is usually accompanied by an elongation of the material into another direction. The ratio of displacements is called the Poisson's ratio ν. Note that it is positive when a compressional force creates an elongation, so

$$\varepsilon_{yy} = -\nu\varepsilon_{xx}, \tag{1.1.4a}$$

$$\varepsilon_{zz} = -\nu\varepsilon_{xx}. \tag{1.1.4b}$$

The values of the Poisson's ratio range from $-\infty$ to $1/2$. For the majority of materials in nature the Poisson's ratio has positive values, where the value $1/2$ means that the material is incompressible.

As stated previously, to produce a strain (deformation) in a material, it is necessary to apply a stress (force). For a linear elastic material (the generalization of Hooke's Law for continuous media), the normal stress and the normal strain of a face are related through the Young's modulus

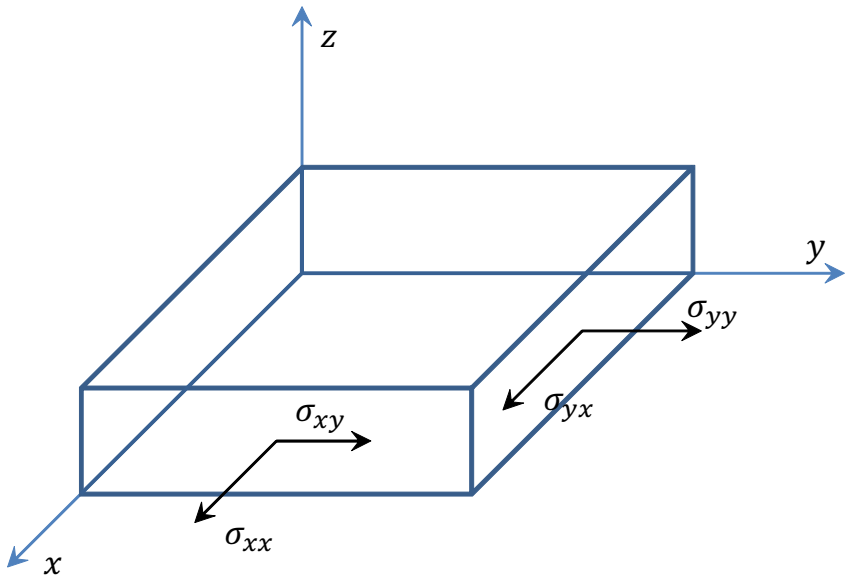

Figure 1.2: Stresses acting on a thin plate

E. In an similar way, the shear stress and the shear strain of one face are related through the shear modulus G. In other words,

$$\sigma_{xx} \cong E\varepsilon_{xx}, \tag{1.1.5a}$$

$$\sigma_{xy} \cong G\gamma_{xy}. \tag{1.1.5b}$$

For the case of the materials used throughout this work, that is homogeneous and isotropic, the shear modulus is related to the Young's modulus and the Poisson's ratio as

$$G = \frac{E}{2(1+\nu)}. \tag{1.1.6}$$

Now, taking into account the combination all the stresses acting on Fig. 1.2(2D system) the normal strains on each face are

$$\varepsilon_{xx}^{(T)} = \frac{1}{E}(\sigma_{xx} - \nu\sigma_{yy}), \tag{1.1.7a}$$

$$\varepsilon_{yy}^{(T)} = \frac{1}{E}(\sigma_{yy} - \nu\sigma_{xx}), \tag{1.1.7b}$$

$$\varepsilon_{zz}^{(T)} = -\frac{\nu}{E}(\sigma_{xx} + \sigma_{yy}), \tag{1.1.7c}$$

and the shear strains are

$$\gamma_{xy}^{(T)} = \frac{1}{G}\sigma_{xy}, \tag{1.1.8a}$$

$$\gamma_{xz}^{(T)} = 0, \tag{1.1.8b}$$

$$\gamma_{yz}^{(T)} = 0, \tag{1.1.8c}$$

where T denotes total. Notice that the shear strains are not influenced by the normal stresses.

1.2 Beam Physics

In this section, the Euler-Bernoulli beam equation of motion is derived, a solution is given and finally the boundary conditions are presented.

1.2.1 Equation of motion

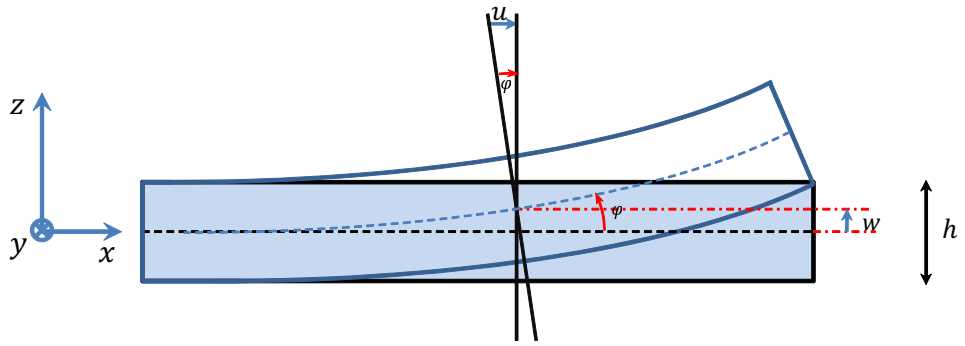

Figure 1.3: Beam variables in a neutral and flexed state.

The beam theory is a mathematical one-dimensional representation of a long and thin three-dimensional body that undergoes flexure. The thickness and the width of the beam are considered to be much smaller

than its length ($\lambda >> h$), so the problem is reduced to finding the deflection of the middle axis of the beam. The following assumptions are made:

1. The plane halving the beam height h is called the *middle plane*.
2. The normal to the *middle plane* remains normal after deformation.
3. The *middle plane* is unstrained.
4. The normal stress in the z-direction is negligible.

Let us consider the variables defined in Fig. 1.3. The displacement in the x-direction, $u(x, z)$, can be related to the angle of rotation φ as

$$u_x(x, z) = -z\varphi(x). \tag{1.2.1}$$

Notice that for small deflections, the angle of rotation of the middle axis may be approximated by the tangent itself ($\varphi \cong \partial w/\partial x$). Then, from the definition of the normal strain, Eq. (1.1.1), we know that

$$\varepsilon_x = -z\frac{\partial^2 w}{\partial x^2}, \tag{1.2.2}$$

and by following Hooke's Law, the axial stress acting on the cross section, A, of the beam is defined as

$$\sigma_{xx} = -Ez\frac{\partial^2 w}{\partial x^2}. \tag{1.2.3}$$

The resultant moment $M(x)$ produced on a cross section A of the beam by σ_{xx} about an axis that passes through the middle plane is obtain by integrating the moments produced by each individual differential normal stress σ_{xx}, thus

$$M(x) = \int_A \sigma_{xx} z dA. \tag{1.2.4}$$

Substituting Eqs. (1.2.3) into the above expression we obtain

$$M(x) = -EI\partial\frac{\partial^2 w}{\partial x^2}, \tag{1.2.5}$$

where I is the second moment of area.

In a similar way, the resultant shear force $Q(x)$ acting on a cross section A of the beam is obtained by integrating the differential shear stresses σ_{xz}, thus

$$Q(x) = \int_A \sigma_{xz} dA, \tag{1.2.6}$$

which is not derived in this explanation. Further on, it will be obtained through a simpler method.

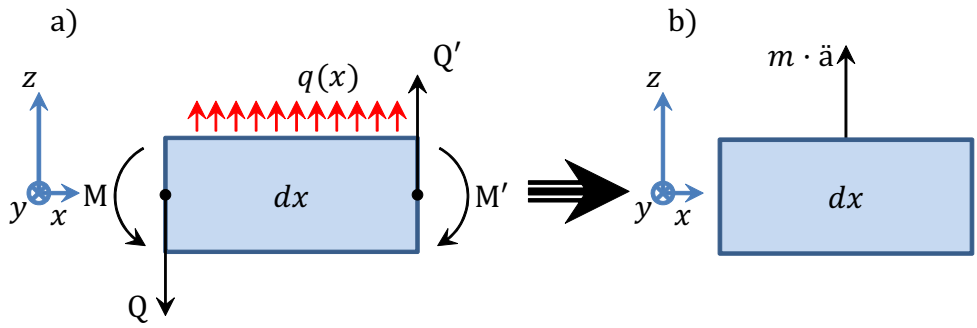

Figure 1.4: Forces and moments acting on a beam differential element (a) and the effective differential element (b).

To derive the equation of motion for a beam let us consider a generic differential element of length dx as shown in Fig. 1.4. Over the beam an external force is applied that can be represented as a distributed transverse load $q(x)$. The right hand rule is applied, so a force in the positive z-direction, will create a counter clock moment in the positive faces. The sum of all the moment and shear forces on the differential element have to met Newton's Second Law, so

$$q(x)dx - Q + \left[Q + \frac{\partial Q}{\partial x}dx\right] = m\frac{\partial^2 w}{\partial t^2}dx, \quad (1.2.7a)$$

$$Q\frac{dx}{2} + \left[Q + \frac{\partial Q}{\partial x}dx\right]\frac{dx}{2} + M - \left[M + \frac{\partial M}{\partial x}dx\right] = 0, \quad (1.2.7b)$$

where m is the mass per unit length. By neglecting second order terms, the equations reduces

$$q(x) + \frac{\partial Q}{\partial x} = m\frac{\partial^2 w}{\partial t^2}, \quad (1.2.8a)$$

$$Q = \frac{\partial M}{\partial x}. \quad (1.2.8b)$$

Substituting Eq. (1.2.5) and (1.2.8b) into Eq. (1.2.8a) we obtain the known Euler-Bernoulli equation of motion for beams

$$\frac{\partial^2}{\partial x^2}EI\frac{\partial^2 w}{\partial x^2} - m\frac{\partial^2 w}{\partial t^2} = q(x). \quad (1.2.9)$$

1.2.2 Solution to the Euler-Bernoulli beam equation

To show an example of solution of the previous equation, let's consider time harmonic propagation of the form $e^{-i\omega t}$ inside an homogenous rectangular section beam with constant thickness h and width b over a length L. Then the solution for the Euler-Bernoulli equation has the following shape

$$w(x) = C_1 e^{+ikx} + C_2 e^{-ikx} + C_3 e^{+kx} + C_4 e^{-kx}, \quad (1.2.10)$$

where the C_i are coefficients that have to be determined with the boundary conditions and k is the wave number obtained from

$$k = \left(\frac{m\omega^2}{EI}\right)^{\frac{1}{4}}, \quad (1.2.11)$$

being $m = \rho h b$, ρ the mass density and I the second moment of area. For the case of a rectangular section beam with the x-axis passing through its center

$$I = \int_A z^2 dA = \frac{bh^3}{12}. \tag{1.2.12}$$

1.2.3 Boundary conditions

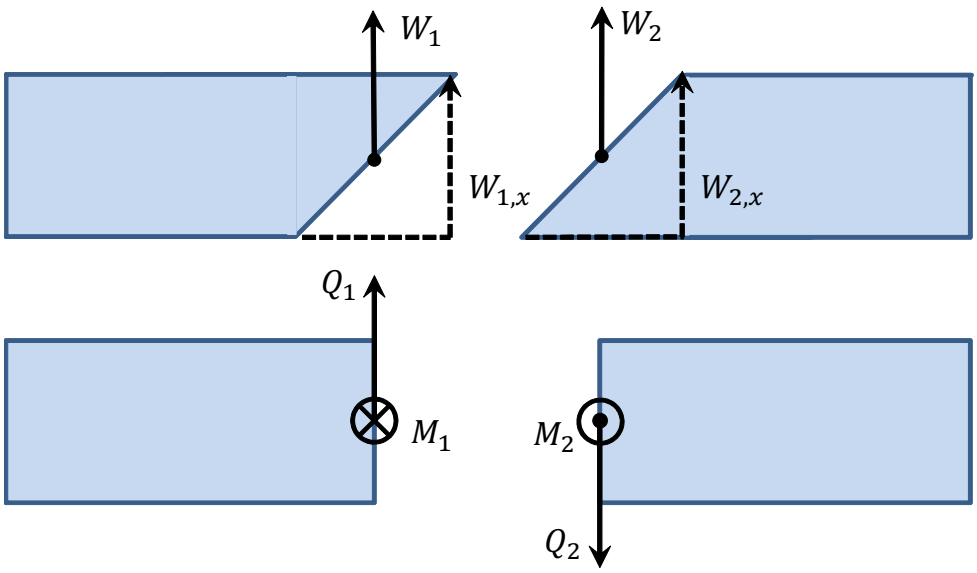

Figure 1.5: Schematic view of the beam boundary conditions.

The boundary conditions determine how the equation of motion of two different media are coupled. Being Eq. (1.2.9) a fourth order equation it will require four boundary conditions at the interface Ω. Thus, the displacement W_i and the slope $W_{i,x}$ have to be continuous and the sum of the moments M_i and the shear forces Q_i have to be zero (see Fig 1.5), that is

$$W^-(x)\big|_\Omega = W^+(x)\big|_\Omega\,, \tag{1.2.13a}$$
$$\left.\frac{\partial W^-(x)}{\partial x}\right|_\Omega = \left.\frac{\partial W^+(x)}{\partial x}\right|_\Omega\,, \tag{1.2.13b}$$
$$M^-(x)\big|_\Omega = M^+(x)\big|_\Omega\,, \tag{1.2.13c}$$
$$Q^-(x)\big|_\Omega = Q^+(x)\big|_\Omega\,. \tag{1.2.13d}$$

From these equations every other boundary condition can be specified, being the most common ones, the clamped condition, when the boundary is fixed to prevent any movement,

$$W^-(x)\big|_\Omega = 0, \tag{1.2.14a}$$
$$\left.\frac{\partial W^-(x)}{\partial x}\right|_\Omega = 0, \tag{1.2.14b}$$

and the free vibration, when there is no moment or shear force acting on the boundary,

$$M^-(x)\big|_\Omega = 0, \tag{1.2.15a}$$
$$Q^-(x)\big|_\Omega = 0. \tag{1.2.15b}$$

1.3 Plate Physics

In this section, the Kirchhoff-Love plate equation of motion is derived, a solution is given for Cartesian and polar coordinates and the boundary conditions are presented.

1.3.1 Equation of motion

The Kirchhoff-Love plate theory can be easy expanded from the Euler-Bernoulli beam theory. It is intrinsically a 2D theory, and can be expressed for the two main coordinate system. First, the derivation for the

Cartesian system is explained, then, following an analogy, the derivation for the Polar system can be obtained. As in the case of the beam, the thickness is considered to be much smaller than its length and width ($\lambda >> h$), so the problem reduces to finding the deflection of the middle axis of the beam. The following assumptions are made:

1. The plane halving the plate height h is called the *middle plane*.
2. The normal to the *middle plane* remains normal after deformation.
3. The *middle plane* is unstrained.
4. The normal stress in the z-direction is negligible.

Cartesian coordinates

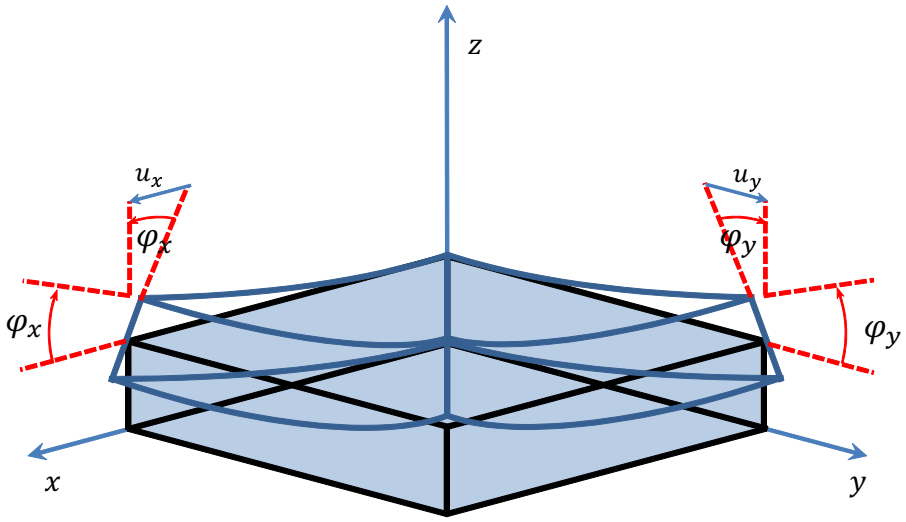

Figure 1.6: Plate variables in a neutral and flexed state.

Let us consider the variables defined in Fig. 1.6. As in the case of the beam, the displacement in the x-direction, u_x, and the y-direction, u_y, can be related to the angles of rotation (φ_i) as

$$u_x(x,y,z) = -z\varphi_x, \tag{1.3.1a}$$

$$u_y(x,y,z) = -z\varphi_y. \tag{1.3.1b}$$

Notice that for small deflections, the angle of rotation of the middle axis may be approximated by the tangent itself ($\varphi_i = \partial w/\partial i$). Then, from the definition of the normal and shear stress Eqs. (1.1.7) and (1.1.8) and from Eqs. (1.1.1) and (1.1.3) we obtain the stresses acting on a 2D differential element as

$$\sigma_{xx} = -\frac{Ez}{1-\nu^2}\left(\frac{\partial^2 w}{\partial x^2} + \nu\frac{\partial^2 w}{\partial y^2}\right), \tag{1.3.2a}$$

$$\sigma_{yy} = -\frac{Ez}{1-\nu^2}\left(\frac{\partial^2 w}{\partial y^2} + \nu\frac{\partial^2 w}{\partial x^2}\right), \tag{1.3.2b}$$

$$\sigma_{xy} = \sigma_{yx} = -\frac{Ez}{1+\nu}\left(\frac{\partial^2 w}{\partial x \partial y}\right). \tag{1.3.2c}$$

In analogy to the simple beam theory, the resultant bending and twisting moments by unit length M produced by the normal stress about an axis x_i that passes through the middle plane are obtained by integrating the moments produced by each individual differential force σ along the height of the plate, thus

$$M_x(x,y) = \int_{-h/2}^{h/2} \sigma_{xx} z dz = -D\left(\frac{\partial^2 w}{\partial x^2} + \nu\frac{\partial^2 w}{\partial y^2}\right), \tag{1.3.3a}$$

$$M_y(x,y) = \int_{-h/2}^{h/2} \sigma_{xx} z dz = -D\left(\frac{\partial^2 w}{\partial y^2} + \nu\frac{\partial^2 w}{\partial x^2}\right), \tag{1.3.3b}$$

$$M_{xy}(x,y) = M_{yx} = \int_{-h/2}^{h/2} \sigma_{xy} z dz = -D(1-\nu)\left(\frac{\partial^2 w}{\partial x \partial y}\right), \tag{1.3.3c}$$

where $D = Eh^3/12(1-\nu^2)$ is the flexural stiffness. In a similar way, the resultant shear forces per unit length Q are obtained by integrating the differential shear stress $\sigma_{x_i z}$, thus

$$Q_x(x,y) = \int_{-h/2}^{h/2} \sigma_{xz} dz, \tag{1.3.4a}$$

$$Q_y(x,y) = \int_{-h/2}^{h/2} \sigma_{yz} dz, \tag{1.3.4b}$$

which are not derived in this explanation. Further on, they will be obtain through a simpler method.

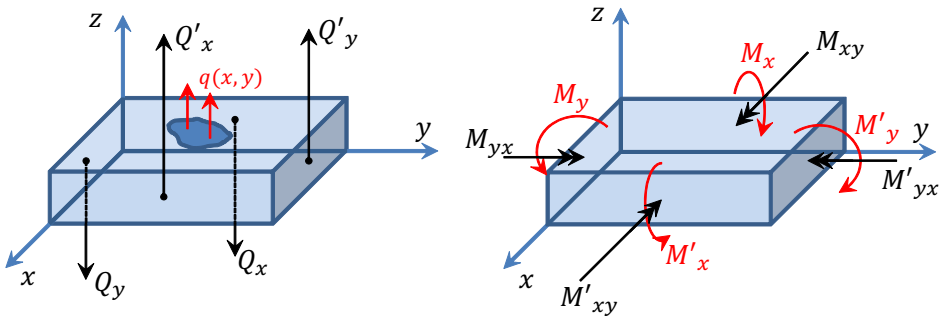

Figure 1.7: Plate Cartesian differential element.

To derive the equation of motion of a plate let us consider a generic differential element of length $dx \times dy$ as shown in Fig. 1.7. Over the plate an external force is applied that can be represented as a distributed load $q(x,y)$. The right hand rule is applied, so a force in the positive z-direction, will create a counter clock moment in the positive faces. The sum of all the moments and shear forces on the differential element have to met Newton's Second Law, so

$$\left[Q_x + \frac{\partial Q_x}{\partial x}dx\right]dy - Q_x dy + \left[Q_y + \frac{\partial Q_y}{\partial y}dy\right]dx - Q_y dx + q(x,y)dxdy = \rho h \frac{\partial^2 w}{\partial t^2}dxdy, \tag{1.3.5a}$$

$$M_y dx - \left[M_y + \frac{\partial M_y}{\partial y}dy\right]dx + M_{xy}dy - \left[M_{xy} + \frac{\partial M_{xy}}{\partial x}dx\right]dy + Q_y dx\frac{dy}{2} + \left[Q_y + \frac{\partial Q_y}{\partial y}dy\right]dx\frac{dy}{2} = 0, \tag{1.3.5b}$$

$$M_x dy - \left[M_x + \frac{\partial M_x}{\partial x}dx\right]dy - M_{yx}dx + \left[M_{yx} + \frac{\partial M_{yx}}{\partial y}dy\right]dx + Q_x dy\frac{dx}{2} + \left[Q_x + \frac{\partial Q_x}{\partial x}dx\right]dy\frac{dx}{2} = 0, \tag{1.3.5c}$$

where ρ is the mass density and h is the plate height. By neglecting third order terms they reduce to

$$q(x,y) + \frac{\partial Q_x}{\partial x} + \frac{\partial Q_y}{\partial y} = \rho h \frac{\partial^2 w}{\partial t^2}, \tag{1.3.6a}$$

$$Q_y = \frac{\partial M_y}{\partial y} + \frac{\partial M_{xy}}{\partial x}, \tag{1.3.6b}$$

$$Q_x = \frac{\partial M_x}{\partial x} - \frac{\partial M_{yx}}{\partial y}. \tag{1.3.6c}$$

From here, applying Eq. (1.3.3), we can define the shear forces per unit length as

$$Q_x = -D\frac{\partial}{\partial x}\left(\Delta w\right), \tag{1.3.7a}$$

$$Q_y = -D\frac{\partial}{\partial y}\left(\Delta w\right). \tag{1.3.7b}$$

where $\Delta = \nabla^2$ is the Laplace operator in Cartesian coordinates.

Substituting Eqs. (1.3.7) into (1.3.6a) we obtain the known Kirchhoff-Love equation of motion for plate as

$$D\nabla^4 w - \rho h \frac{\partial^2 w}{\partial t^2} = q(x, y), \tag{1.3.8}$$

where ∇ is the Nabla operator in Cartesian coordinates.

Polar coordinates

The relationship between the Cartesian and the polar coordinates is

$$r^2 = x^2 + y^2 \qquad ; \qquad \theta = \arctan\left(\frac{y}{x}\right). \tag{1.3.9}$$

Applying the chain rule the following expression can be found for the first derivative respect to x and y

$$\frac{\partial w}{\partial x} = \frac{\partial w}{\partial r}\frac{\partial r}{\partial x} + \frac{\partial w}{\partial \theta}\frac{\partial \theta}{\partial x} = \frac{\partial w}{\partial r}\cos\theta - \frac{1}{r}\frac{\partial w}{\partial \theta}\sin\theta, \tag{1.3.10a}$$

$$\frac{\partial w}{\partial y} = \frac{\partial w}{\partial r}\frac{\partial r}{\partial y} + \frac{\partial w}{\partial \theta}\frac{\partial \theta}{\partial y} = \frac{\partial w}{\partial r}\sin\theta + \frac{1}{r}\frac{\partial w}{\partial \theta}\cos\theta. \tag{1.3.10b}$$

Then the second order derivatives can be obtained from

$$\frac{\partial^2 w}{\partial x^2} = \left(\frac{\partial}{\partial r}\cos\theta - \frac{1}{r}\frac{\partial}{\partial \theta}\sin\theta\right)\left(\frac{\partial w}{\partial r}\cos\theta - \frac{1}{r}\frac{\partial w}{\partial \theta}\sin\theta\right), \tag{1.3.11a}$$

$$\frac{\partial^2 w}{\partial y^2} = \left(\frac{\partial}{\partial r}\sin\theta + \frac{1}{r}\frac{\partial}{\partial \theta}\cos\theta\right)\left(\frac{\partial w}{\partial r}\sin\theta + \frac{1}{r}\frac{\partial w}{\partial \theta}\cos\theta\right), \tag{1.3.11b}$$

$$\frac{\partial^2 w}{\partial x \partial y} = \left(\frac{\partial}{\partial r}\cos\theta - \frac{1}{r}\frac{\partial}{\partial \theta}\sin\theta\right)\left(\frac{\partial w}{\partial r}\sin\theta + \frac{1}{r}\frac{\partial w}{\partial \theta}\cos\theta\right). \tag{1.3.11c}$$

Repeating the operations, the third and forth order derivation are obtained. Then, Eq. (1.3.8) can be written in polar coordinates as

$$D\nabla^4 w - \rho h \frac{\partial^2 w}{\partial t^2} = q(x, y), \tag{1.3.12}$$

where now ∇ is the Nabla operator in polar coordinates.

Moments and shear forces can be transformed in a similar way. Let us consider the differential element shown in Fig. 1.8 of length $dr \times d\theta$.

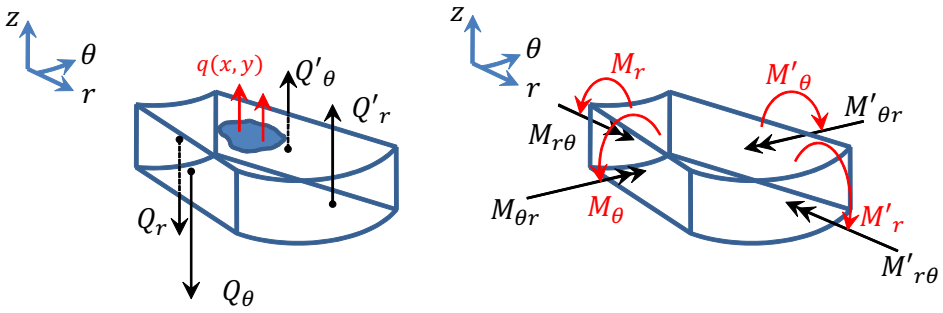

Figure 1.8: Plate polar differential element.

Notice that the x-axis coincides with the radius r, so the bending and twisting moments per unit length M coincide with the ones from Eq. (1.3.3) at the same point, and by substituting $\theta = 0$ in Eq. (1.3.11), we obtain

$$M_r(r,\theta) = -D\left(\frac{\partial^2 w}{\partial r^2} + \nu\left[\frac{1}{r}\frac{\partial w}{\partial r} + \frac{1}{r^2}\frac{\partial^2 w}{\partial \theta^2}\right]\right), \tag{1.3.13a}$$

$$M_r(r,\theta) = -D\left(\frac{1}{r}\frac{\partial w}{\partial r} + \frac{1}{r^2}\frac{\partial^2 w}{\partial \theta^2} + \nu\frac{\partial^2 w}{\partial r^2}\right), \tag{1.3.13b}$$

$$M_{r\theta}(r,\theta) = M_{\theta r} = -D(1-\nu)\left(\frac{1}{r}\frac{\partial^2 w}{\partial r \partial \theta} - \frac{1}{r^2}\frac{\partial w}{\partial \theta}\right). \tag{1.3.13c}$$

In a similar manner to Eq. (1.3.7), we obtain the shear forces per unit length as

$$Q_r = -D\frac{\partial}{\partial r}(\Delta w), \tag{1.3.14a}$$

$$Q_\theta = -D\frac{1}{r}\frac{\partial}{\partial \theta}(\Delta w). \tag{1.3.14b}$$

where $\Delta = \nabla^2$ is the Laplace operator in polar coordinates.

1.3.2 Solution to the Kirchhoff-Love's plate equation

To show an example of the solution of the previous equation, let's consider an homogeneous plate with constant thickness h, Young Modulus E, mass density ρ and Poisson's ratio ν. Considering time harmonic solutions of the form $e^{-i\omega t}$, the solution of the Eq. (1.3.8) can be expanded as $W = W_1 + W_2$, where W_1 and W_2 are solutions of the Helmholtz and modified Helmholtz equations, respectively. Thus,

$$\begin{aligned} w = &\left(C_{x1}e^{+ik_x x} + C_{x2}e^{-ik_x x} + C_{x3}e^{+k_x x} + C_{x4}e^{-k_x x}\right) \\ &\left(C_{y1}e^{+ik_y y} + C_{y2}e^{-ik_y y} + C_{y3}e^{+k_y y} + C_{y4}e^{-k_y y}\right), \end{aligned} \tag{1.3.15}$$

where the C_{xi} and C_{yi} are coefficients have to be determined with the boundary conditions and k_x and k_y are the wave numbers in the x- and the y-direction, respectively. They are obtained from

$$k^4 = k_x^4 + k_y^4 = \frac{\rho h \omega^2}{D}. \tag{1.3.16}$$

In a similar way, the solution of Eq. (1.3.12) in Polar coordinates is an expansion in q-terms of Bessel functions (see Appendix A). On the one hand, the solutions to the Helmholtz equations correspond to Bessel functions, $J_q(x)$, and first kind Hankel functions, $H_q(x) = J_q(x) + iY_q(x)$. On the other hand, the solutions to the modified Helmholtz equation are modified Bessel functions of the first, $I_q(x)$, and second kind, $K_q(x)$. Then, the incoming and outgoing waves are expressed as

$$\begin{aligned} W(r,\theta) = \sum_q \big[&A_q^{(J)} J_q(k_r r) + A_q^{(I)} I_q(k_r r) + \\ &B_q^{(H)} H_q(k_r r) + B_q^{(K)} K_q(k_r r)\big]\, e^{iq\theta}, \end{aligned} \tag{1.3.17}$$

where $A_q^{(J)}$ and $A_q^{(I)}$ are the incoming wave coefficients and $B_q^{(H)}$ and $B_q^{(K)}$ are the outgoing wave coefficients; all to be determined using boundary conditions. In addition, k_r is the wave number obtained from

$$k_r = \left(\frac{\rho h \omega^2}{D} \right)^{1/4}. \tag{1.3.18}$$

1.3.3 Boundary conditions

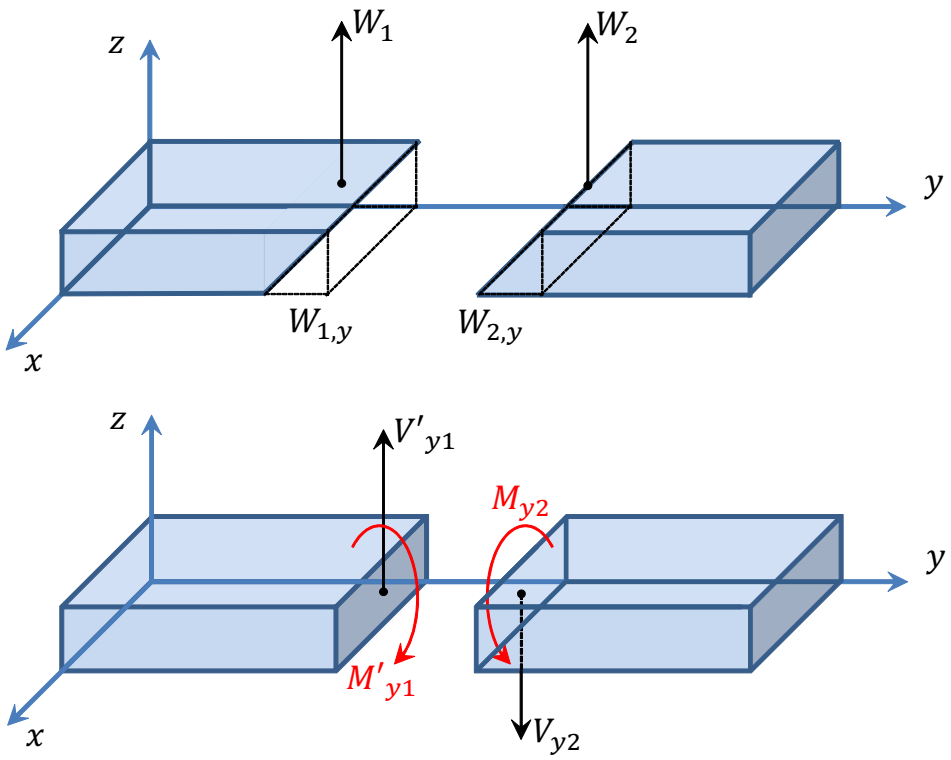

Figure 1.9: Schematic view of the plate boundary conditions.

The boundary conditions determine how the equations of motion of two different media are coupled. Being Eq. (1.3.8) or Eq. (1.3.12), fourth order equations they will require four boundary conditions at the interface Ω. Thus, the displacement in the surface W_Ω and the normal slope to the surface $W_{,n}$ have to be continuous and the sum of the normal to the surface moments M_n and the shear forces acting on the surface have to be are zero (see Fig. 1.9). That is

$$W^-\big|_\Omega = W^+\big|_\Omega\,, \tag{1.3.19a}$$

$$\left.\frac{\partial W^-}{\partial \mathbf{n}}\right|_\Omega = \left.\frac{\partial W^+}{\partial \mathbf{n}}\right|_\Omega, \tag{1.3.19b}$$

$$M^-_{\mathbf{n}}\big|_\Omega = M^+_{\mathbf{n}}\big|_\Omega\,, \tag{1.3.19c}$$

$$V^-_{\mathbf{n}}\big|_\Omega = V^+_{\mathbf{n}}\big|_\Omega\,, \tag{1.3.19d}$$

where $\mathbf{n}$ and $\mathbf{t}$ make reference to the normal and tangent vectors to the surface Ω, respectively. $V_{\mathbf{n}}$ is the Kirchhoff stress [72] defined as

$$V_{\mathbf{n}} = Q_{\mathbf{n}} + \frac{\partial}{\partial \mathbf{t}} M_{\mathbf{nt}}. \tag{1.3.20}$$

It is observed that the Kirchhoff stress takes into account not only the shear forces, but also the twisting moments acting on the surface. Throughout this work, we make an extensive use of the radial Kirchhoff-Stress which is given by

$$V_r = -D\frac{\partial}{\partial r}\Delta w - D(1-\nu)\frac{1}{r^2}\frac{\partial}{\partial \theta}\left(\frac{\partial^2 w}{\partial r \partial \theta} - \frac{1}{r}\frac{\partial w}{\partial \theta}\right), \tag{1.3.21}$$

where $\partial/\partial\mathbf{t} \cong (1/r)\,\partial/\partial\theta$ has been used.

From these equations every other boundary condition can be specified, being the most common ones the clamped condition, where the wave impinges a region which cannot support any displacement

$$W^-\big|_\Omega = 0, \tag{1.3.22a}$$

$$\left.\frac{\partial W^-}{\partial \mathbf{n}}\right|_\Omega = 0, \tag{1.3.22b}$$

and the free condition, where the region is entirely free and there are no twisting or bending moments and also no shear forces

$$M^-_{\mathbf{n}}\big|_\Omega = 0, \tag{1.3.23a}$$

$$V^-_{\mathbf{n}}\big|_\Omega = 0. \tag{1.3.23b}$$

1.4 Single scatterer

When an external field impinges a close region Ω with different elastic parameters as the background, a scattering phenomenon occurs. In the present work, the close region is considered a cylinder and therefore the problem can be solved using polar coordinates in 2D.

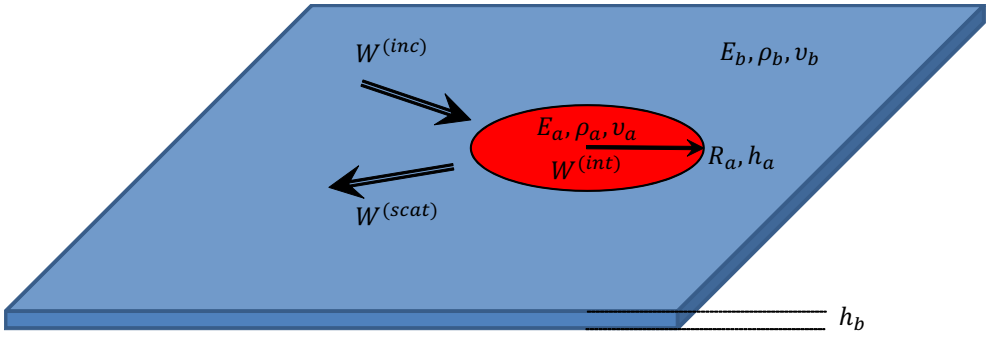

Figure 1.10: Scheme of a plate of thickness h_b and elastic parameters (E_b, ρ_b, ν_v). The circular region with radius R_a has a thickness h_a and elastic parameters (E_a, ρ_a, ν_a). An incoming wave W_{inc} impinges the region and generates a scattering wave W_{scat} and an internal wave W_{int}.

Let consider a infinite plate of thickness h_b with the following elastic parameters, mass density ρ_b, Young's modulus E_b and Poisson ratio ν_b. The circular region defined by $r \leq R_a$ with thickness h_a has different elastic parameters as the plate, denoted by ρ_a, E_a and ν_a (see Fig. 1.10). The plate thickness is not going to be considered a geometrical parameter anymore, but it is instead introduced in the boundary conditions through the elastic properties of the material. Then, the solution of the Kirchhoff-Love plate equation in each medium in polar coordinates is

$$W^{(inc)} + W^{(scat)} = \sum_q \left[A_q^{(J)} J_q(k_b r) + A_q^{(I)} I_q(k_b r)\right] e^{iq\theta} + \sum_q \left[B_q^{(H)} H_q(k_b r) + B_q^{(K)} K_q(k_b r)\right] e^{iq\theta}, \quad r > R_a \tag{1.4.1a}$$

$$W^{(int)} = \sum_q \left[C_q^{(J)} J_q(k_a r) + C_q^{(I)} I_q(k_a r)\right] e^{iq\theta}, \quad r \leq R_a \tag{1.4.1b}$$

where

$$k_b = \left(\frac{\rho_b h_b \omega^2}{D_b}\right)^{1/4} \quad ; \quad k_a = \left(\frac{\rho_a h_a \omega^2}{D_a}\right)^{1/4}, \tag{1.4.2a}$$

$$D_b = \frac{E_b h_b^3}{12(1-\nu_b^2)} \quad ; \quad D_a = \frac{E_a h_a^3}{12(1-\nu_a^2)}, \tag{1.4.2b}$$

and $W^{(inc)}$, $W^{(scat)}$ and $W^{(int)}$ make reference to the incoming, scattered and internal wave, respectively.

Let's group the incoming, outgoing and internal wave coefficients in vector form as

$$\mathbf{A}_q = \begin{bmatrix} A_q^{(J)} \\ A_q^{(I)} \end{bmatrix} \quad ; \quad \mathbf{B}_q = \begin{bmatrix} B_q^{(H)} \\ B_q^{(K)} \end{bmatrix} \quad ; \quad \mathbf{C}_q = \begin{bmatrix} C_q^{(J)} \\ C_q^{(I)} \end{bmatrix}, \tag{1.4.3}$$

Then, in the general problem, the incoming coefficients $\mathbf{A}_q$ are the inputs and the scattered coefficients $\mathbf{B}_q$ are the outputs. They can be related through a infinite matrix called the transfer matrix or T-matrix as

$$\begin{bmatrix} \vdots \\ \mathbf{B}_q \\ \vdots \end{bmatrix} = \begin{bmatrix} \ddots & \vdots & \\ \cdots & \mathbf{T}_{qs} & \cdots \\ & \vdots & \ddots \end{bmatrix} \begin{bmatrix} \vdots \\ \mathbf{A}_s \\ \vdots \end{bmatrix}. \tag{1.4.4}$$

To obtain the T-matrix it is necessary to apply the boundary conditions of a circular interface [see Eq. (1.3.19)]

$$\left(W^{(inc)} + W^{(scat)}\right)\Big|_{r=R_a} = W^{(int)}\Big|_{r=R_a}, \tag{1.4.5a}$$

$$\left(\frac{\partial W^{(inc)}}{\partial r} + \frac{\partial W^{(scat)}}{\partial r}\right)\Big|_{r=R_a} = \frac{\partial W^{(int)}}{\partial r}\Big|_{r=R_a}, \tag{1.4.5b}$$

$$\left(M_r^{(inc)} + M_r^{(scat)}\right)\Big|_{r=R_a} = M_r^{(int)}\Big|_{r=R_a}, \tag{1.4.5c}$$

$$\left(V_r^{(inc)} + V_r^{(scat)}\right)\Big|_{r=R_a} = V_r^{(int)}\Big|_{r=R_a}. \tag{1.4.5d}$$

To eliminate the sum in q, the equations are multiplied by $e^{is\theta}$ and integrating from 0 to 2π. Then, only the terms $s = q$ are different than zero and the system reduces to

$$\mathbf{M}_q \begin{bmatrix} \mathbf{B}_q \\ \mathbf{C}_q \end{bmatrix} = -\mathbf{N}_s \left[\mathbf{A}_s\right], \tag{1.4.6}$$

where $\mathbf{M}_q$ and $\mathbf{N}_q$ are matrix of the form

$$\mathbf{M}_q = \begin{bmatrix} H_q(k_bR_a) & K_q(k_bR_a) & -J_q(k_aR_a) & -I_q(k_aR_a) \\ (k_bR_a)H_q'(k_bR_a) & (k_bR_a)K_q'(k_bR_a) & -(k_aR_a)J_q'(k_aR_a) & -(k_aR_a)I_q'(k_aR_a) \\ S_q^H(k_b,R_a) & S_q^K(k_b,R_a) & -S_q^J(k_a,R_a) & -S_q^I(k_a,R_a) \\ T_q^H(k_b,R_a) & T_q^K(k_b,R_a) & -T_q^J(k_a,R_a) & -T_q^I(k_a,R_a) \end{bmatrix}, \tag{1.4.7}$$

$$\mathbf{N}_s = \begin{bmatrix} J_s(k_bR_a) & I_s(k_bR_a) \\ (k_bR_a)J_s'(k_bR_a) & (k_bR_a)I_s'(k_bR_a) \\ S_s^J(k_b,R_a) & S_s^I(k_b,R_a) \\ T_s^J(k_b,R_a) & T_s^I(k_b,R_a) \end{bmatrix}, \tag{1.4.8}$$

and

$$S_q^{\xi}(k_i,r) = -\frac{D_i}{r^2}\left[(q^2(1-\nu_i) \mp (k_i r)^2)\xi_q(k_i r) - (1-\nu_i)(k_i r)\xi_q'(k_i r)\right], \tag{1.4.9}$$

$$T_q^{\xi}(k_i,r) = -\frac{D_i}{r^3}\left[(q^2(1-\nu_i))\xi_q(k_i r) - (q^2(1-\nu_i) \pm (k_i r)^2)(k_i r)\xi_q'(k_i r)\right], \tag{1.4.10}$$

and $\xi = J, I, H, K$; the upper sign is used for (J, H) and the lower sign for (I, K). To simplify $S_q^{\xi}(k_i, r)$ and $T_q^{\xi}(k_i, r)$, the second order ODEs of these functions and the Wronskian (A.1.9) and (A.2.9) identities have been used. Solving the previous system of equations we obtain the relationship between the coefficients as

$$-\mathbf{M}_q^{-1}\mathbf{N}_s \equiv \begin{bmatrix}\mathbf{T}_{qs}\\ \mathbf{X}_{qs}\end{bmatrix}, \tag{1.4.11}$$

where $\mathbf{T}_{qs}$ is the qs-element of the T-matrix and $\mathbf{X}_{qs}$ relates the $\mathbf{C}_q$ with the $\mathbf{A}_s$ coefficients.

For a circular region, the T-matrix is semi-diagonal (the diagonal is filled with two by two matrix) and note these equations are only valid when the center of the coordinate system coincides with the center of the circular region.

1.4.1 Types of incoming waves

To obtain the scattering coefficients, the incoming field has to be expressed as a combination of Bessel functions with arguments in polar coordinates $\mathbf{r} = (r, \theta)$. Additionally, if the circular region is not centered in the origin of coordinates, the reference frame of the incoming field has to be shifted to coincide with it. The most common incoming waves are the plane wave and the cylindrical point source.

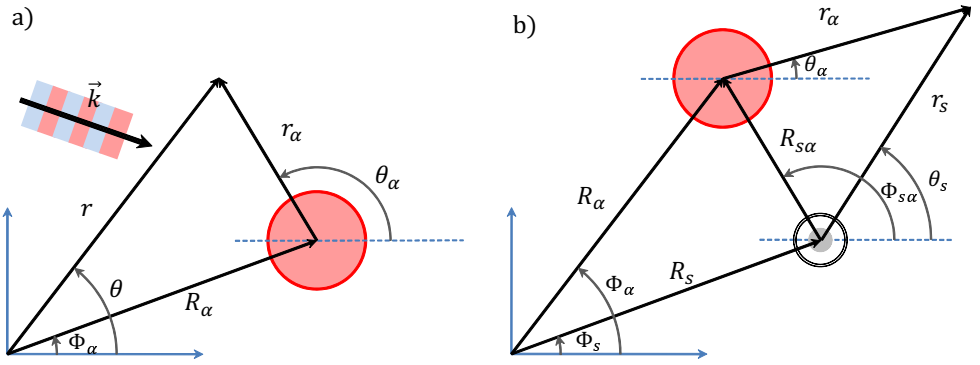

Figure 1.11: Source types: (a) Plane wave and (b) cylindrical point source.

Plane Wave

The plane wave is a constant-frequency wave whose wavefronts (surfaces of constant phase) are infinite parallel planes of constant peak-to-peak amplitude normal to the phase velocity vector. This incoming field is defined by the wavenumber $\vec{k} = \mathbf{k} = k(\cos\theta_s, \sin\theta_s)$ and is represented by the equation

$$W_s(\mathbf{r}) = e^{i\mathbf{k}\cdot\mathbf{r}} \tag{1.4.12}$$

By using the integral definition of the Bessel function [1] it can be cast as

$$W_s(\mathbf{r}) = \sum_q \left[i^q e^{-iq\theta_s}\right] J_q(kr) e^{iq\theta} = \sum_q A_q^{(J)} J_q(kr) e^{iq\theta}. \tag{1.4.13}$$

Notice that $A_q^{(I)} = 0$ for all q [see (1.4.1a)] . When the scatter is not placed at the center of the coordinates, the incoming wave can be expressed in a different reference frame α, shown in Fig. 1.11(a), as

$$W_s(\mathbf{r}_\alpha) = e^{i\mathbf{k}\cdot\mathbf{R}_\alpha} e^{i\mathbf{k}\cdot\mathbf{r}_\alpha} = \sum_q \left[i^q e^{\mathbf{k}\cdot\mathbf{R}_\alpha} e^{-iq\theta_s} \right] J_q(kr_\alpha) e^{iq\theta_\alpha} = \sum_q (A_q^{(J)})_\alpha J_q(kr_\alpha) e^{iq\theta_\alpha}, \tag{1.4.14}$$

where $\mathbf{r}_\alpha = \mathbf{r} - \mathbf{R}_\alpha$

Cylindrical point source

The point source is defined as a combination of Bessel functions of the same order ξ. Let us suppose a cylindrical point source $\xi = 0$ with wavenumber $\mathbf{k}$ located at $\mathbf{R}_s = (R_s, \Phi_s)$ as shown in Fig. 1.11(b), then the wave equation is defined as

$$W_s(\mathbf{r}) = \sum_q \left[H_\xi(kr_s) + \frac{2i}{\pi} K_\xi(kr_s) \right] e^{iq\theta_s}, \tag{1.4.15}$$

where $\mathbf{r}_s = \mathbf{r} - \mathbf{R}_s = (r_s, \theta_s)$. Using Graph's Addition Theorem (see Appendix A.3), the previous equation can be expanded in Bessel functions and expressed in a different frame α, shown in 1.11(b), as

$$\begin{aligned} W_s(\mathbf{r}_\alpha) = & \sum_q \left[H_{q-\xi}(kR_{\alpha s}) e^{i(\xi-q)\Psi_{\alpha s}} \right] J_q(kr_\alpha) e^{iq\theta_\alpha} + \\ & \sum_q \left[\frac{2i}{\pi} (-1)^q K_{q-\xi}(kR_{\alpha s}) e^{i(\xi-q)\Psi_{\alpha s}} \right] I_q(kr_\alpha) e^{iq\theta_\alpha} \\ = & \sum_q (A_q^{(J)})_\alpha J_q(kr_\alpha) e^{iq\theta_\alpha} + (A_q^{(I)})_\alpha I_q(kr_\alpha) e^{iq\theta_\alpha}, \end{aligned} \tag{1.4.16}$$

where $\mathbf{r}_\alpha = \mathbf{r} - \mathbf{R}_\alpha$

1.5 Multiple scattering

Consider a cluster of N circular regions with arbitrary position located at (R_α, Φ_α) and radius R_α^{cyl} with $\alpha = 1, 2, \ldots, N$ as shown in Fig. 1.12.

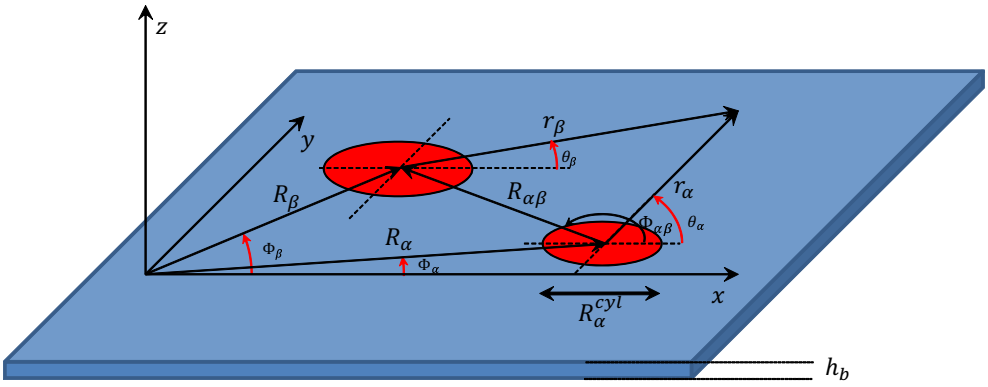

Figure 1.12: Cluster of N=2 circular regions located at (R_α, Φ_α) and (R_β, Φ_β).

If an external displacement interacts with the cluster, the total incoming displacement on the α-region will be a combination of the incident and the scattered displacement of all the other region. Therefore the system is completely coupled as the wave bounces back and forth through the cluster.

Let us define the total incoming displacement as $W_\alpha^{(inc)}$, which takes into account all the incoming waves arriving to the α-region; and the total scattered displacement as $W_\alpha^{(scat)}$. Their expressions have the form

$$W_\alpha^{(inc)} = \sum_s \mathbf{F}_s^{JI}(k_b r, \theta)(\mathbf{A}_s^{(T)})_\alpha, \tag{1.5.1a}$$

$$W_\alpha^{(scat)} = \sum_q \mathbf{F}_q^{HK}(k_b r, \theta)(\mathbf{B}_q^{(T)})_\alpha, \tag{1.5.1b}$$

where

$$\mathbf{F}_q^{\Upsilon\Phi}(\kappa, \gamma) = \begin{bmatrix} \Upsilon_q(\kappa_i) & \Phi_q(\kappa) \end{bmatrix} e^{iq\gamma}, \tag{1.5.2}$$

and $(\mathbf{A}_s^{(T)})_\alpha$ and $(\mathbf{B}_q^{(T)})_\alpha$ are the total incoming and scattered coefficients in matrix form, respectively [see Eq. (1.4.3)]. They are related by

$$(\mathbf{B}_q^{(T)})_\alpha = \sum_s (\mathbf{T}_{qs})_\alpha (\mathbf{A}_s^{(T)})_\alpha, \tag{1.5.3}$$

where $\mathbf{T}_{qs}$ is a two by two matrix [see Eq. (1.4.11)].

As was explained in the previous chapter, the T-matrix relates the incoming and the scattered wave, but only when the center of the coordinate system and the circular region coincide. To change the position of the origin of coordinates, Graphs Theorem (see Appendix A.3) can be applied, such that the total scattering displacement created by the β-region described as

$$W_\beta^{(scat)}(r_\beta, \theta_\beta) = \sum_r \mathbf{F}_r^{HK}(k_b r_\beta, \theta_\beta)(\mathbf{B}_r^{(T)})_\beta, \tag{1.5.4}$$

can be rewritten in the system of coordinates centered at α as

$$W_\beta^{(scat)}(r_\alpha, \theta_\alpha) = \sum_r \left[\sum_s \mathbf{F}_s^{JI}(k_b r_\alpha, \theta_\alpha) \mathbf{G}_{rs}(k_b R_{\alpha\beta}, \Phi_{\alpha\beta}) \right] (\mathbf{B}_r^{(T)})_\beta \tag{1.5.5}$$

where

$$\mathbf{G}_{rs}(\kappa, \gamma) = \begin{bmatrix} H_{s-r}(\kappa) & 0 \\ 0 & (-1)^r K_{s-r}(\kappa) \end{bmatrix} e^{i(r-s)\gamma} \tag{1.5.6}$$

Then the total incident displacement on the α-region is written as

$$W_\alpha^{(inc)} = \sum_s \mathbf{F}_s^{JI}(k_b r_\alpha, \theta_\alpha)(\mathbf{A}_s)_\alpha + \sum_{\beta \neq \alpha} W_\beta^{(scat)}(r_\alpha, \theta_\alpha), \tag{1.5.7}$$

where $(\mathbf{A}_s)_\alpha$ are the incoming coefficients of the external displacement field expressed in the α frame. Notice that both fields are now expressed in the α frame. Combining Eq. (1.5.1a) with (1.5.7) and rearranging terms we obtain

$$(\mathbf{A}_s^{(T)})_\alpha = (\mathbf{A}_s)_\alpha + \sum_{\beta \neq \alpha} \sum_r \mathbf{G}_{rs}(k_b R_{\alpha\beta}, \Phi_{\alpha\beta})(\mathbf{B}_r^{(T)})_\beta \tag{1.5.8}$$

Multiplying this equation by $(\mathbf{T}_{qs})_\alpha$ and adding for all s we get

$$(\mathbf{B}_q^{(T)})_\alpha = \sum_s (\mathbf{T}_{qs})_\alpha (\mathbf{A}_s)_\alpha + \sum_{\beta\neq\alpha} \sum_s (\mathbf{T}_{qs})_\alpha \sum_r \mathbf{G}_{rs}(k_b R_{\alpha\beta}, \Phi_{\alpha\beta})(\mathbf{B}_r^{(T)})_\beta \tag{1.5.9}$$

By introducing the Kronecker delta function ($\delta_{ij} = 1$ only if $i = j$) and rearranging terms we arrive to the following equation

$$\sum_\beta \sum_r (\mathbf{M}_{qr})_{\alpha\beta}(\mathbf{B}_r^{(T)})_\beta = (\mathbf{N}_q)_\alpha \tag{1.5.10}$$

where

$$(\mathbf{M}_{qr})_{\alpha\beta} = \delta_{\alpha\beta}\delta_{qr} - \sum_s (1-\delta_{\alpha\beta})(\mathbf{T}_{qs})_\alpha \mathbf{G}_{rs}(k_b R_{\alpha\beta}, \Phi_{\alpha\beta}) \tag{1.5.11}$$

$$(\mathbf{N}_q)_\alpha = \sum_s (\mathbf{T}_{qs})_\alpha (\mathbf{A}_s)_\alpha \tag{1.5.12}$$

More specifically, equation (1.5.10) can be written in matrix form as its acoustic counterpart [see Part I Eqs. (1.3.10)-(1.3.11b)]. Now each element of the matrix will be a two by two matrix instead of a scalar value. To solve the infinite linear systems described in Eq. (1.5.10) it is truncated so that $\max|q| = \max|r| = \max|s| < Q$. Then the total scattering coefficients $(\mathbf{B}_r^{(T)})_\alpha$ are obtained and the total displacement W in the background medium is calculated as

$$W(\mathbf{r}) = \sum_q \mathbf{F}_q^{JI}(k_b r, \theta)\mathbf{A}_q + \sum_\alpha \sum_q \mathbf{F}_q^{HK}(k_b r_\alpha, \theta_\alpha)(\mathbf{B}_q^{(T)})_\alpha, \tag{1.5.13}$$

with $\mathbf{r}_\alpha = \mathbf{r} - \mathbf{R}_\alpha$ being the distance from the center of the α-region to an arbitrary position $\mathbf{r}$ in the background medium.

To calculate the internal displacement of each region, the internal coefficients of each region $(\mathbf{C}_q)_\alpha$ are needed. These are obtained by combining Eq. (1.5.8)] and Eq. (1.4.6).

1.6 Multilayer scatterer

This section presents the multilayer scattering method. This models is employed to make numerical simulations of structures that are radially inhomogeneous, that is, their parameters depend only on the radial coordinate.

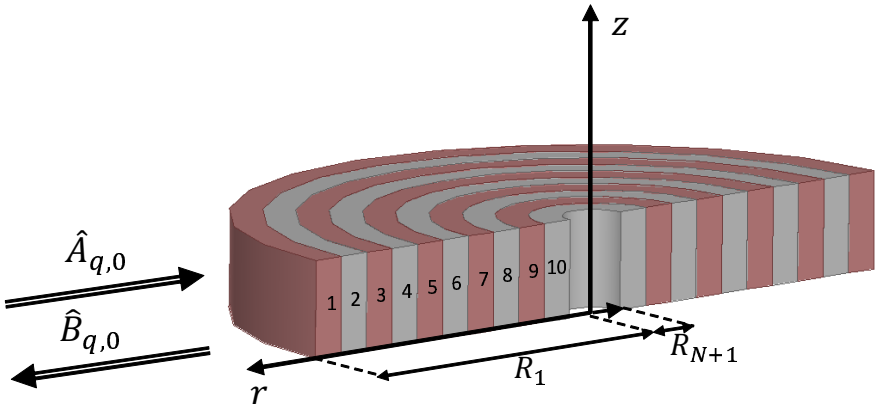

Figure 1.13: Multilayered structure employed in the multiple scattering algorithm with $N = 10$ layers. The background layer is $n = 0$ and corresponds to the region $r > R_1$) and the core layer is $n = N + 1$ and corresponds to the region $r < R_{N+1}$.

The continuous variation of the parameters of the structures is discretized into a number N of homogeneous cylindrically symmetric layers. Figure 1.13 shows the cylindrical structure discretized into $N = 10$ layers each one with different elastic properties. The layers are numbered such that the background corresponds to $n = 0$ and the core layer corresponds to $n = N + 1$.

From the previous section, it is known that the displacement in a thin plate is a combination of standard and modified Bessel function. So, in the case of a multilayer structure, the field of the n-th layer is described as

$$W_n(r,\theta) = \sum_q \left[(A_q^{(J)})_n J_q(k_n r) + (A_q^{(I)})_n I_q(k_n r)\right] e^{iq\theta} + \sum_q \left[(B_q^{(H)})_n H_q(k_n r) + (B_q^{(K)})_n K_q(k_n r)\right] e^{iq\theta}, \tag{1.6.1}$$

being $(A_q^{(J)})_n, (A_q^{(I)})_n, (B_q^{(H)})_n, (B_q^{(K)})_n$ the coefficients of the expansion (A for the incoming wave towards the center of the region and B for the scattered one) and k_n being the wavenumber in the n-th layer.

The objective now is to relate the coefficients of each layer with the ones of the previous and next layer. Defining

$$\mathbf{A}_{q,n} = \begin{bmatrix} (A_q^{(J)})_n \\ (A_q^{(I)})_n \end{bmatrix} \quad , \quad \mathbf{B}_{q,n} = \begin{bmatrix} (B_q^{(H)})_n \\ (B_q^{(K)})_n \end{bmatrix}, \tag{1.6.2}$$

from Fig. 1.13 we can deduce that the relation between the coefficients of layers n and $n-1$ is given by

$$\mathbf{A}_{q,n} = \mathbf{T}_{q,n-1n} \cdot \mathbf{A}_{q,n-1} + \mathbf{R}_{q,nn-1} \cdot \mathbf{B}_{q,n}, \tag{1.6.3a}$$

$$\mathbf{B}_{q,n-1} = \mathbf{R}_{q,n-1n} \cdot \mathbf{A}_{q,n-1} + \mathbf{T}_{q,nn-1} \cdot \mathbf{B}_{q,n}, \tag{1.6.3b}$$

where $\mathbf{T}_{q,n-1n}$ and $\mathbf{R}_{q,n-1n}$ are the q-th element of the transmission and reflection coefficient matrix (2x2) from layer $n-1$ to n, respectively. Defining the layer elastic impedance matrices (2x2) as $\mathbf{B}_{q,n} = \mathbf{Z}_{q,n} \cdot \mathbf{A}_{q,n}$, the above equations read as

$$\mathbf{A}_{q,n} = (\mathbf{I} - \mathbf{R}_{q,nn-1} \cdot \mathbf{Z}_{q,n})^{-1} \cdot \mathbf{T}_{q,n-1n} \cdot \mathbf{A}_{q,n-1}, \tag{1.6.4a}$$

$$\mathbf{A}_{q,n} = (\mathbf{T}_{q,nn-1} \cdot \mathbf{Z}_{q,n})^{-1} \cdot (\mathbf{Z}_{q,n-1} - \mathbf{R}_{q,n-1n}) \cdot \mathbf{A}_{q,n-1}, \tag{1.6.4b}$$

from which we can obtain the recursive relation for the coefficient $\mathbf{Z}_{q,n}$ as

$$\mathbf{Z}_{q,n-1} = \mathbf{R}_{q,n-1n} + \mathbf{T}_{q,nn-1} \cdot \mathbf{Z}_{q,n} \cdot \mathbf{X}_{q,n}, \tag{1.6.5a}$$

$$\mathbf{X}_{q,n} = (\mathbf{I} - \mathbf{R}_{q,nn-1} \cdot \mathbf{Z}_{q,n})^{-1} \cdot \mathbf{T}_{q,n-1n}. \tag{1.6.5b}$$

Starting at the last layer $n = N$, since $\mathbf{B}_{q,N+1} = 0$, the impedance in the last layer $\mathbf{Z}_{q,N}$ is simply

$$\mathbf{B}_{q,N} = \mathbf{R}_{q,NN+1} \cdot \mathbf{A}_{q,N} \rightarrow \mathbf{Z}_{q,N} = \mathbf{R}_{q,NN+1}. \tag{1.6.6}$$

The iterative process continues till $n = 1$, so all $\mathbf{Z}_{q,n}$ and $\mathbf{X}_{q,n}$ matrix are obtained. Then, the incoming and scattering coefficients of each layer are given as a function of $\mathbf{A}_{q,0}$, which is defined by the external incident field, applying the following relationships

$$\mathbf{B}_{q,n} = \mathbf{Z}_{q,n} \cdot \mathbf{A}_{q,n}, \tag{1.6.7a}$$

$$\mathbf{A}_{q,n+1} = \mathbf{X}_{q,n} \cdot \mathbf{A}_{q,n}. \tag{1.6.7b}$$

Notice that with few modifications in the notation is is possible to couple the Multiple Scattering (see 1.5) and the Multilayer Scattering algorithms and therefore have a cluster of multilayered structures.

Reflection and transmission coefficients

The calculation of the reflection and transmission coefficients of every layer in both propagation directions (to and from the center of the structure), required to realize the aforementioned procedure, is detailed below.

Let us consider a single layer with only one boundary where an incoming wave $\mathbf{A}_{q,i}$ impinges on the interface. In Fig. 1.14a the incoming wave $\mathbf{A}_{q,n}$ travels towards the center of the circular region, producing a reflected wave $\mathbf{B}_{q,n}$ in the opposite direction and a transmitted one $\mathbf{A}_{q,n+1}$ to the next layer. On the other hand, in Figure 1.14b, the incoming wave $\mathbf{A}_{q,n+1}$ travels towards infinity, producing a reflected wave $\mathbf{B}_{q,n+1}$ towards the center of the circular region and a transmitted one $\mathbf{A}_{q,n}$ to the previous layer.

To obtain these reflection and transmission matrices, the boundary conditions described in Eqs. (1.4.4) are imposed. For the first system, the coefficients of layers n and $n + 1$ are related by

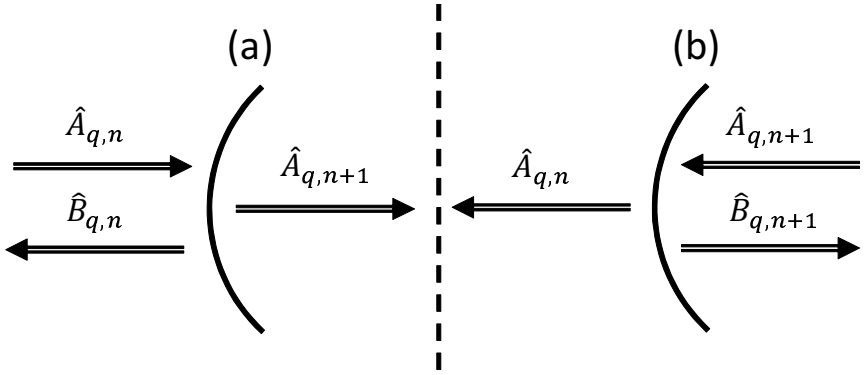

Figure 1.14: Mono-layer systems employed to obtain the reflexion and transmission matrices from layer n to $n+1$ (a) and from layer $n+1$ to n (b).

$$\mathbf{M}_q^{(1)} \begin{bmatrix} \mathbf{B}_{q,n} \\ \mathbf{A}_{q,n+1} \end{bmatrix} = -\mathbf{N}_q^{(1)} \begin{bmatrix} \mathbf{A}_{q,n} \end{bmatrix}, \tag{1.6.8}$$

where

$$\mathbf{M}_q^{(1)} = \begin{bmatrix} H_q(\kappa_n) & K_q(\kappa_n) & -J_q(\kappa_{n+1}) & -I_q(\kappa_{n+1}) \\ (\kappa_n)H_q'(\kappa_n) & (\kappa_n)K_q'(\kappa_n) & -(\kappa_{n+1})J_q'(\kappa_{n+1}) & -(\kappa_{n+1})I_q'(\kappa_{n+1}) \\ S_q^H(\kappa_n) & S_q^K(\kappa_n) & -S_q^J(\kappa_{n+1}) & -S_q^I(\kappa_{n+1}) \\ T_q^H(\kappa_n) & T_q^K(\kappa_n) & -T_q^J(\kappa_{n+1}) & -T_q^I(\kappa_{n+1}) \end{bmatrix}, \tag{1.6.9}$$

$$\mathbf{N}_q^{(1)} = \begin{bmatrix} J_q(\kappa_n) & I_q(\kappa_n) \\ (\kappa_n)J_q'(\kappa_n) & (\kappa_n)I_q'(\kappa_n) \\ S_q^J(\kappa_n) & S_q^I(\kappa_n) \\ T_q^J(\kappa_n) & T_q^I(\kappa_n) \end{bmatrix}, \tag{1.6.10}$$

and $\kappa_n = k_n R_n$. Additionally, $S_n^\xi(\kappa_n) \equiv S_n^\xi(k_n, R_n)$ and $T_n^\xi(\kappa_n) \equiv T_n^\xi(k_n, R_n)$ where defined in Eq. (1.4.9) and Eq. (1.4.10), respectively.

Similarly, for the second system, the coefficients of layers $n+1$ and n are related by

$$\mathbf{M}_q^{(2)} \begin{bmatrix} \mathbf{B}_{q,n+1} \\ \mathbf{A}_{q,n} \end{bmatrix} = -\mathbf{N}_q^{(2)} \begin{bmatrix} \mathbf{A}_{q,n+1} \end{bmatrix}, \tag{1.6.11}$$

where

$$\mathbf{M}_q^{(2)} = \begin{bmatrix} J_q(\kappa_{n+1}) & I_q(\kappa_{n+1}) & -H_q(\kappa_n) & -K_q(\kappa_n) \\ (\kappa_{n+1})J'_q(\kappa_{n+1}) & (\kappa_{n+1})I'_q(\kappa_{n+1}) & -(\kappa_n)H'_q(\kappa_n) & -(\kappa_n)K'_q(\kappa_n) \\ S_q^J(\kappa_{n+1}) & S_q^I(\kappa_{n+1}) & -S_q^H(\kappa_n) & -S_q^K(\kappa_n) \\ T_q^J(\kappa_{n+1}) & T_q^I(\kappa_{n+1}) & -T_q^H(\kappa_n) & -T_q^K(\kappa_n) \end{bmatrix}, \quad (1.6.12)$$

$$\mathbf{N}_q^{(2)} = \begin{bmatrix} H_q(\kappa_{n+1}) & K_q(\kappa_{n+1}) \\ (\kappa_{n+1})H'_q(\kappa_{n+1}) & (\kappa_{n+1})K'_q(\kappa_{n+1}) \\ S_q^H(\kappa_{n+1}) & S_q^K(\kappa_{n+1}) \\ T_q^H(\kappa_{n+1}) & T_q^K(\kappa_{n+1}) \end{bmatrix}. \quad (1.6.13)$$

Now, by knowing the definition of the reflection and transmission matrices in the first system

$$\mathbf{R}_{q,nn+1} = \mathbf{B}_{q,n} \cdot (\mathbf{A}_{q,n})^{-1}, \quad (1.6.14)$$

$$\mathbf{T}_{q,nn+1} = \mathbf{A}_{q,n+1} \cdot (\mathbf{A}_{q,n})^{-1}, \quad (1.6.15)$$

and the second system,

$$\mathbf{R}_{q,n+1n} = \mathbf{B}_{q,n+1} \cdot (\mathbf{A}_{q,n+1})^{-1}, \quad (1.6.16)$$

$$\mathbf{T}_{q,n+1n} = \mathbf{A}_{q,n} \cdot (\mathbf{A}_{q,n+1})^{-1}. \quad (1.6.17)$$

It is straightforward to obtain them from Eq. (1.6.8) and (1.6.11).

1.7 Scattering cross section

As in the case of acoustics waves, the displacement maps of a plate can be plotted, but to better analyze the results, or compare the effects produced by two different systems, one dimensional plots are more suitable.

Once again, let us introduce the scattering cross section (SCS). The scattering cross-section is defined in optics as a hypothetical area describing the likelihood of light particles being scattered by a scattering center. It is a measure of the strength of the interaction between the scattered

particles and one or several scattering centers. Also in this case, the SCS also describes the shape of the scattered displacement at the far field produced by a circular region. It is defined as

$$\sigma_{scat}(k,\theta) = \lim_{r\to\infty} \left|\sqrt{r} W^{scat}(r,\theta)\right| \tag{1.7.1}$$

where W^{scat} is the scattered displacement, which is a combination of Bessel functions. Its asymptotic expression detailed in Appendix A can be used.

Combining Eq. (1.4.1a), (1.7.1) and (A.2.10) the SCS of the circular region centered in the origin of coordinates is

$$\sigma_{scat}(k,\theta) = \left|\sqrt{\frac{2}{\pi k}} \sum_q (-i)^q B_q^{(H)} e^{iq\theta}\right|. \tag{1.7.2}$$

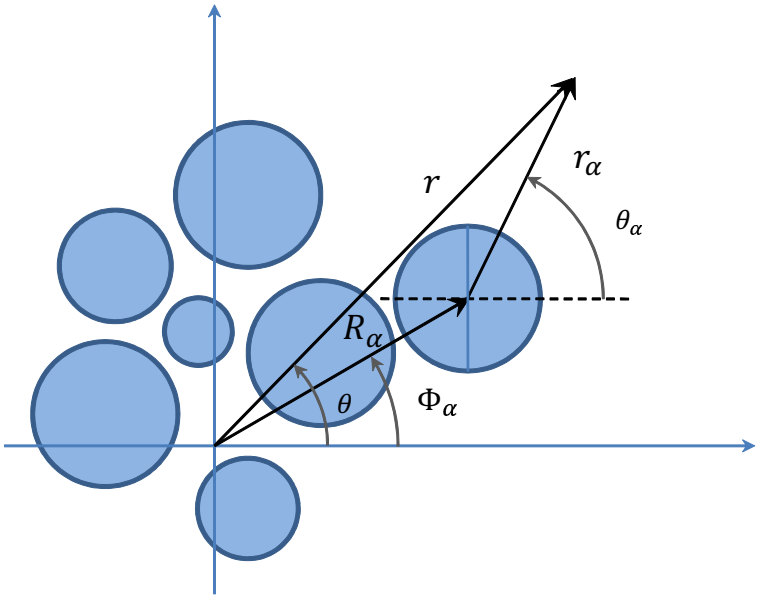

Figure 1.15: Variables needed to calculate the scattering cross section.

The calculation of the SCS of a cluster is more complex and some of the steps will be below. Let's consider the cluster shown in Fig 1.15. From the right hand side of Eq. (1.5.13) we know that

$$W^{scat}(r,\theta) = \sum_{\alpha}\sum_{q} \mathbf{F}_q^{HK}(k_b r_\alpha, \theta_\alpha)(\mathbf{B}_q^{(T)})_\alpha. \tag{1.7.3}$$

When $r \to \infty$ we can apply the asymptotic expression of the Bessel functions [see Eq. (A.1.10) and Eq. (A.2.10)]. Note that $K_q(r) \to 0$. Then the previous equation is rewritten as

$$\lim_{r\to\infty} W^{scat}(r,\theta) \approx \sum_{\alpha}\sum_{q} (B_q^{(TH)})_\alpha \sqrt{\frac{2}{\pi k r}} (-i)^q e^{-i\pi/4} e^{ik(r_\alpha - R_\alpha\cos(\theta-\Phi_\alpha))} e^{iq\theta}, \tag{1.7.4}$$

where $(B_q^{(TH)})_\alpha$ is the total scattering coefficient of the Hankel function and the following simplifications have been performed

$$\lim_{r\to\infty} r_\alpha \approx \begin{cases} r - R_\alpha\cos(\theta-\Phi_\alpha) & \text{For the exponentials} \\ r & \text{For the rest} \end{cases} \tag{1.7.5}$$

$$\lim_{r\to\infty} \theta_\alpha \approx \theta \tag{1.7.6}$$

Finally, the SCS of a cluster of cylinders is

$$\sigma_{scat}(k,\theta) = \left| \sqrt{\frac{2}{\pi k}} \sum_{q}\sum_{\alpha} (-i)^q (B_q^{(TH)})_\alpha e^{-ikR_\alpha\cos(\theta-\Phi_\alpha)} e^{iq\theta} \right|. \tag{1.7.7}$$

1.8 Energy Flux

In a two dimensional system, the energy flux (Φ) is the rate of energy transfer through a closed boundary Ω. Assuming a periodic motion of the form $e^{-i\omega t}$, it is defined as

$$\Phi = \frac{\omega D}{2} \int_{\Omega} I \; d\Omega, \tag{1.8.1}$$

where

$$\mathbf{I} = \Im\left[W\frac{\partial}{\partial n}\Delta W^* - \Delta W^*\frac{\partial W}{\partial n}\right], \tag{1.8.2}$$

and Δ is the Laplace operator, $\Im$ denotes the imaginary part and $\partial/\partial n$ is the derivative with respect to the normal of the boundary Ω.

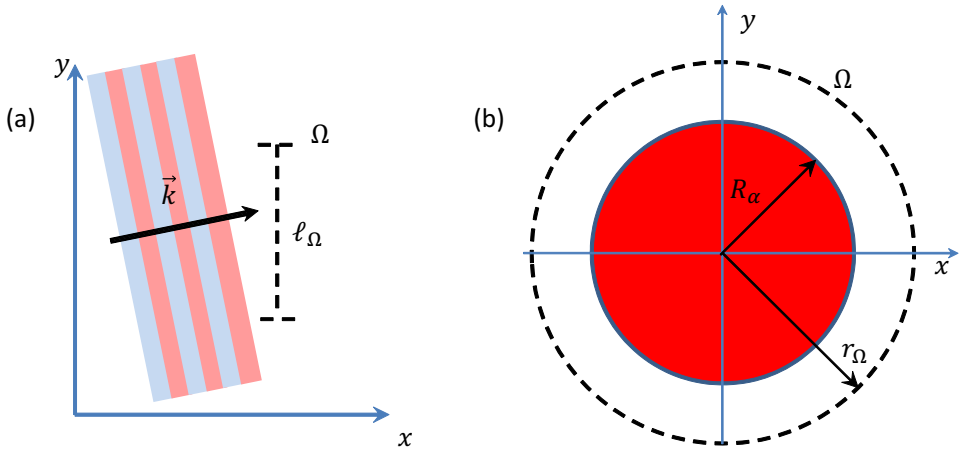

Figure 1.16: Variables used to calculate the intensity of a plane wave (a) and a circular region (b)

In the following paragraphs, we calculate the energy flux of the two main fields used during this work: A plane wave field and the field produced by the interaction of an incident wave impinging a circular region inside a plate.

Plane wave

In the case of a plane wave, it is common to calculate the energy flux of a line segment Ω of length ℓ_Ω, (see Fig. 1.16a). Taking into account that the wavenumber of the plane wave is defined as $\vec{k} = (k_x, k_y)$ and the vector normal to Ω is $\mathbf{n} \equiv \hat{x}$, then the energy flux is defined as

$$\Phi = \frac{\omega^3 ph}{k_x}\ell_\Omega, \tag{1.8.3}$$

where h is the thickness of the plate. Notice that Φ variates with the thickness. If the plate's thickness decreases gradually without reflecting back, the amplitude of a wave increases due to the energy conservation. This result will be important later on.

Single circular region or cluster

To calculate the energy flux of a circular region it is common to define the contour Ω as the boundary of a circle of radius $r_\Omega > R_\alpha$ (see Fig. 1.16b). In this case, the normal vector to the contour coincides with the radial vector, then $\mathbf{n} = \mathbf{r}$. From Eq. (1.4.2) we know that the background field produced by a single scattered is $W = \sum_q W_q$ where

$$W_q = \left[A_q^{(J)} J_q(kr) + A_q^{(I)} I_q(kr) + B_q^{(H)} H_q(kr) + B_q^{(K)} K_q(kr)\right] e^{iq\theta}. \tag{1.8.4}$$

Then, by applying it to Eq. (1.8.1) we obtain the energy flux as

$$\Phi = \frac{\omega D}{2} \int_0^{2\pi} I_r d\Omega, \tag{1.8.5}$$

where

$$I_r = \Im\left[\sum_q W_q \times \sum_s \frac{\partial \Delta W_s^*}{\partial r}\right] + \Im\left[\sum_q \frac{\partial W_q}{\partial r} \times \sum_s \Delta W_s^*\right], \tag{1.8.6}$$

which can be further simplified with the following considerations

1. To obtain the energy flux [Eq. (1.8.5)], $\mathbf{I}$ is integrated from 0 to 2π. In this case, only the terms $s = q$ are different from zero.

2. If the arguments of the Bessel functions are real, then the complex conjugate of the radial functions can be eliminated. Notice that $H = J + iY$. Additionally, the Wronskian identity defined in Appendix A for both regular and modified Bessel functions can be used.

3. Notice also from Eq. (1.8.6) that only the pure imaginary terms are needed.

4. The following properties apply to complex numbers $ZZ^* = |Z|$, $Z + Z^* = 2\Re[Z]$ and $Z - Z^* = 2\Im[Z]$.

Finally, the energy flux is defined as

$$\Phi = 4\omega D k^2 \sum_q \left[|B_q^{(H)}|^2 + \Re\left((A_q^{(J)})^* B_q^{(H)} \right) + \frac{\pi}{2} \Im\left((A_q^{(I)})^* B_q^{(K)} \right) \right]. \tag{1.8.7}$$

As stated previously, the normal to the surface coincides with the radial vector (towards infinity). As a consequence, if $\Phi > 0$ then inside the region there is a source of energy. If $\Phi < 0$ the inside region is absorptive. Finally, if $\Phi = 0$ then there is a balance between the energy amount entering and leaving the region enclosed by Ω. This method has been used through out this work to test if the T-matrix has been calculated correctly.

Chapter 2

Elastic Lenses

This chapter reports several gradient index lenses for flexural waves in thin plates. The method for its realization is explained in the theoretical introduction. Unlike the previous approaches in acoustics, based on phononic crystals, the present method is based on the thickness-dependence of the dispersion relation of flexural waves, which is used to create gradient index devices by means of local variations of the plate thickness. Numerical simulations of known circularly symmetrical gradient index lenses have been performed and the results are presented in later sections.

2.1 Introduction

The equation of motion describing flexural waves in thin plates is modeled using the Kirchhoff-Love plate equation (1.3.12), in which the vertical displacement W of the plate is obtained from

$$\nabla^4 W - k^4 W = 0, \tag{2.1.1}$$

where ω is the angular velocity and the wave number k is given by a quadratic dispersion relation of the form

$$k = \sqrt[4]{\frac{\omega^2 h\rho}{D}}, \tag{2.1.2}$$

being ρ the mass density, h the thickness of the plate, $D = Eh^3/12(1-\nu^2)$ the flexural rigidity, E the Young Modulus and ν the Poisson ratio.

It is seen that both the phase and group velocities of the waves are function of the plate's thickness. It is straightforward to obtain the refractive index as a function of the position-dependent h

$$n(r,\theta) = \frac{c_b}{c} = \sqrt{\frac{h_b}{h(r,\theta)}}, \tag{2.1.3}$$

where h_b is the background's thickness and $h(r,\theta)$ the variation of the thickness in polar coordinates. If all the other elastic properties of the plate remains unchanged, then Eq. (2.1.3) describes how the refractive index increases with decreasing thickness. It is important to notice that, despite of being an intrinsically dispersive medium, the refractive index does not depend on the frequency of the wave.

2.2 Design of elastic lenses

A set of refractive index lenses with circular symmetry have been studied. Table 2.2.1 shows the list of these lenses, corresponding to several solutions of the Luneburg problem with their respective variation of the

Table 2.2.1: Normalized refractive index of several solutions of the Luneburg problem (first four lenses). Additionally, a concentrator lens (last lens) obtained by mapping the electromagnetic regime in the elastic one.

Lens Name	Refractive Index (n)
Luneburg	$n = \sqrt{2 - r^2}$
Maxwell Fish-Eye	$n = 2/(1 + r^2)$
90° Rotating	$rn^4 - 2n + r = 0$
Eaton	$n = \sqrt{2/r - 1}$
Concentrator	$n = 1/r$

refractive index. Any Luneburg lens is a spherically symmetric gradient-index lens with a typical refractive index n decreasing radially from the center to the outer surface [16, 44]. The last device corresponds to the elastic analogue of the optical concentrator studied for electromagnetic waves by Narimanov and Kildishev [52]. Note that all these lenses have been defined for optical waves, however, since they are obtained using the geometrical optics approximation, we assume that the solutions are also valid for flexural waves. This assumption has been successfully applied previously for acoustics in Part I Chapter 2, where the mapping with the electromagnetic waves is well supported.

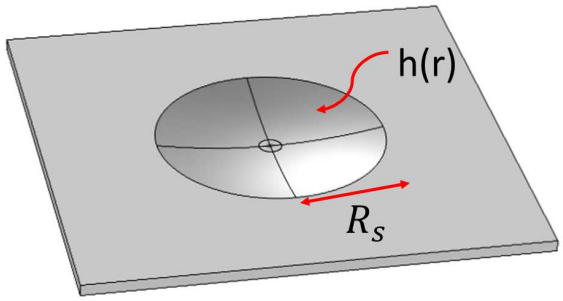

Figure 2.1: Scheme of a circular flexural lens with radius R_s with a radial dependent thickness $h(r)$ to achieve the desired refractive index $n(r)$.

Figure 2.1 shows a schematic view of the five gradient index lenses

presented in this chapter. All the lenses are defined by a circular region $r \leq R_s$ in which the thickness $h(r)$ of the plate is a function of the radial coordinate. This gradual variation of the plate's thickness can be modeled to match the gradual variation of the refractive index of the desired lenses.

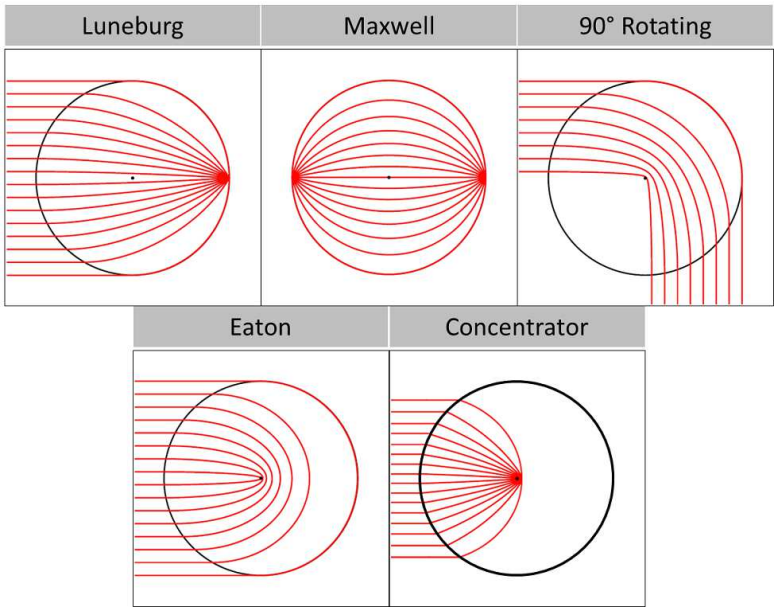

Figure 2.2: Ray tracing for several solutions of the Luneburg problem: Luneburg, Maxwell's fish eye, 90° rotating and Eaton lens. The last one, corresponds to a concentrator lens obtained by mapping the electromagnetic regime in the elastic one.

Figure 2.2 shows the ray tracing of the five lenses. In the case of the Luneburg lens, (a), each point on the surface is the focal point for parallel radiation incident on the opposite side. Therefore a plane wave impinging the lens is focused in a point. This effect can be reversed, so a point source located on the surface will be transformed in a plane wave. The Maxwell's fish eye lens, (b), focuses each point on its surface to the opposite point on the same surface. Within the lens, the paths of the rays are arcs of circles, creating the pattern that gives name to the lens.

The 90° rotating lens (c), as its named implies, bends the trajectory of the waves 90 degrees. Notice that a plane wave impinging the whole surface of the wave will be divided in two. The wave that hits the upper part of the lens while bend downwards, while the one that hits the lower part while bend upwards. The Eaton lens, (d), completely bends the impinging wave backwards. Finally, the concentrator lens, (e), focuses the wave towards the center of the lens.

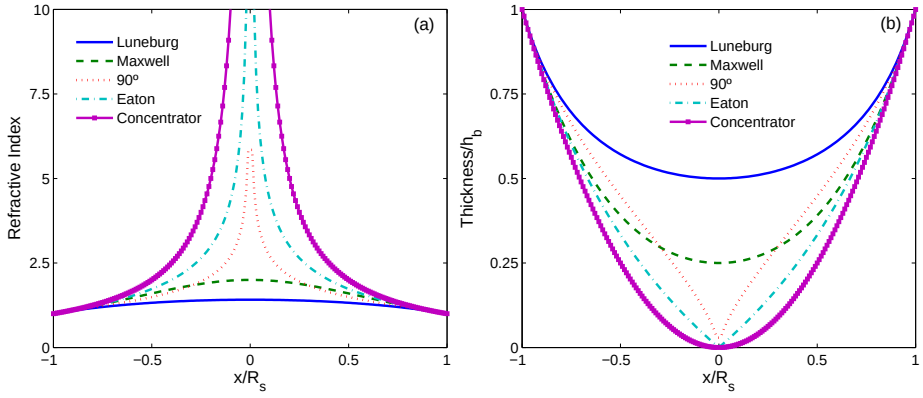

Figure 2.3: Variation of (a) the refractive index and (b) the thickness of the studied lenses in function of the normalized distance.

Figure 2.3(a) shows the variation of the refractive index along the propagation axis for each one of the lenses described in Table 2.2.1. Figure 2.3(b) shows the corresponding solution for the radius-dependent plate thickness $h(r,\theta)/h_b$ obtained using Eq. (2.1.3). Notice that all the proposed flexural lenses present a refractive index larger than that of the background, therefore the height will always be smaller than that of the plate. In other words, all these lenses can be done by gradually decrease the plate's thickness.

A homogeneous infinite aluminum plate with $E = 78.97$ Gpa, $\rho = 2700$ kg/m^3 and $\nu = 0.33$ has been considered. The normalized thickness of the plate is $h_b/R_s = 0.0167$. It is important to note in Fig. 2.3(a) that in some cases the thickness tends to zero as we approach the center of

the lens. To avoid this singularity a minimum thickness is established as $h_{min}(r)/h_b = 0.2{\cdot}10^{-3}$ which is small enough to not affect the simulations.

2.3 Numerical simulations

The simulations have been performed using the one dimensional multilayer scattering method, described in section 1.6, where the continuous refractive index of each lens has been discretized in a number N of cylindrical symmetric layers. As the method describes, the vertical displacement in each layer W_n satisfies the Kirchhoff-Love plate equation and, by applying boundary conditions at each layer, the total scattering displacement of the whole system can be calculated. Each lens was discretized in $N = 100$ and the simulations demonstrate that this is a good approximation to the ideal continuous device for the wavelengths of interest.

Figure 2.4 shows the real part of the displacement $W(r, \theta)$ for the different type of lenses listed in Table 2.2.1 when a field with $kR_s = 8.3\pi$ ($\lambda/R_s = 0.24$) is excited on the plate. Panel (a) shows a Luneburg Lens in which a plane wave is focused at the border of the device. Panel (b) shows a Maxwell Fish-Eye, where, in this case, a point source is excited at the border of the lens and it is focused at the opposite point. Panel (c) shows a 90° Rotating lens, where the incident plane wave is symmetrically redirected along the perpendicular direction of propagation, similarly as the Eaton lens shown in panel (d), where the wave is directed backwards this time. The concentrator lens shown in panel (e) is identical to the photonic black hole [52] which was also studied for acoustic waves in Part I Chapter 3. As expected, the elastic counterpart presents a similar behavior.

Broadband performance

As a parameter used to prove the broadband efficiency of the method to control the refractive index with the thickness, we have used the scatter-

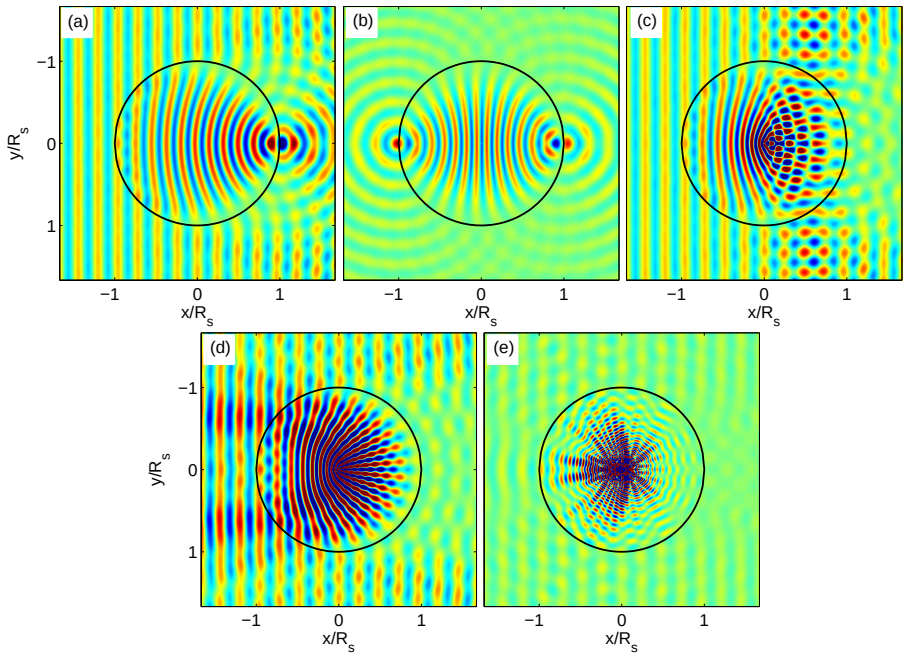

Figure 2.4: Real part of the displacement $W(r,\theta)$ produced by a plane (a,c,d,e) or cylindrical (b) wave impinging a (a) Luneburg, (b) Maxwell, (c) 90° Rotating, (d) Eaton and (e) Concentrator lens at $kR_s = 8.3\pi$. Color scale is the same as in Fig. 2.6.

ing cross section (SCS) defined at as [see section 1.7]

$$\sigma(k,\theta) \equiv \lim_{r\to\infty} \left|\sqrt{r} W_{sc}(r,\theta)\right|, \tag{2.3.1}$$

where $W_{sc}(r\theta)$ is the displacement of the scattered wave. The SCS has been calculated from $\theta \in [-\pi,\pi]$ and for a wide range of normalized wave-numbers ($kR_s \in [5,40]$). Fig. 2.5 (a), on one hand, shows σ for the 90° Rotating Lens. Note how it increases in the near of $\theta = \pm\pi/2$ and becomes narrow when the normalized wave-number increases. By the other hand, Fig. 2.5(b) shows σ for the Eaton Lens. In this case, it increases in the near of $\theta = \pm\pi$ and also narrows with increasing normalized wave-number.

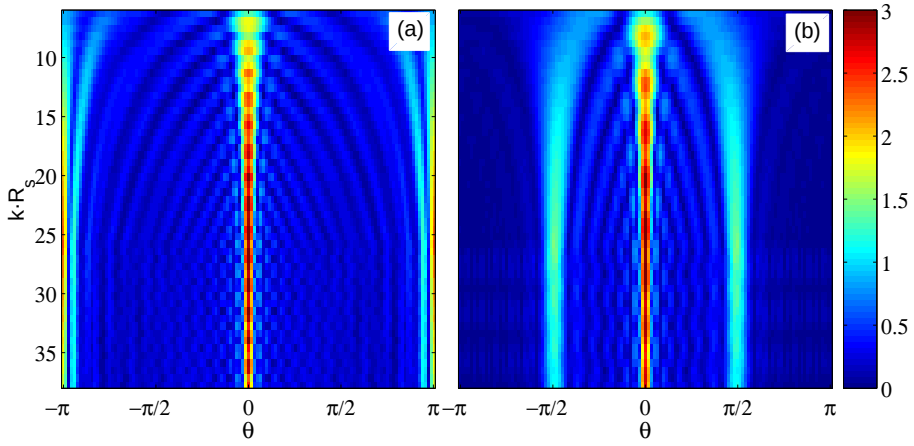

Figure 2.5: Scattering cross-section produced by (a) the 90° Rotating Lens and (b) the Eaton Lens.

Commercial FEM simulator

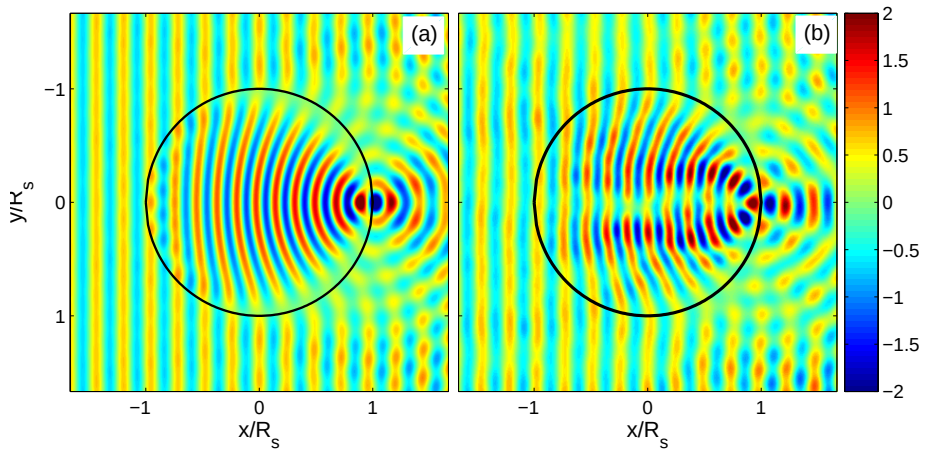

Figure 2.6: Real part of the displacement $W(r, \theta)$ produced by a plane wave impinging a Luneburg Lens. Simulations done with a commercial FEM simulator using the 3D Elastic Theory (a) and a the 1D Multilayer simulator (b).

Finally, in order to test the flexural wave approximation, a numerical experiment employing the full 3D elastic equations, has been realized with a commercial finite element (FEM) simulator. Figure 2.6 shows the real part of the displacement $W(r, \theta)$ resulting when a plane wave impinges the Luneburg lens. Fig 2.6(a) shows the result given by the numerical simulator based on the Kirchhoff-Love plate equation and Figure 2.6(b) the results obtained from the commercial simulator. Both results are very similar and show the expected behavior produced by a Luneburg lens. Note that the result obtained by the commercial simulator are slightly distorted due to the difficulty of achieving zero reflectance on the boundary of the elastic plate. Moreover it is a full 3D elastic simulation.

Chapter 3

Insulating Device

This chapter reports a gradient index device for insulating from vibrations a circular area of a thin plate. The device is made to mimic the attractive and repulsive potentials of a well-like structure. The waves focused at its bottom are dissipated by means of an absorptive layer placed on top of the plate. First an introduction is given, then the design of the device is presented and finally numerical simulations are discussed.

3.1 Introduction

As explained in the chapter 2 the refractive index of a plate can be tailored by changing the thickness of the plate as

$$n(r,) = \sqrt{\frac{h_b}{h(r,\theta)}}, \qquad \text{(2.1.3 revisited)}$$

where h_b is the backgrounds thickness and $h(r,\theta)$ the variation of the thickness in polar coordinates.

Using this method, we have designed a thickness-inhomogeneous region which will attract and dissipate vibrations on the plate, accomplishing then a double objective. From one side, the central region will be properly isolated, from the other one, the device will dissipate the vibrations on the plate.

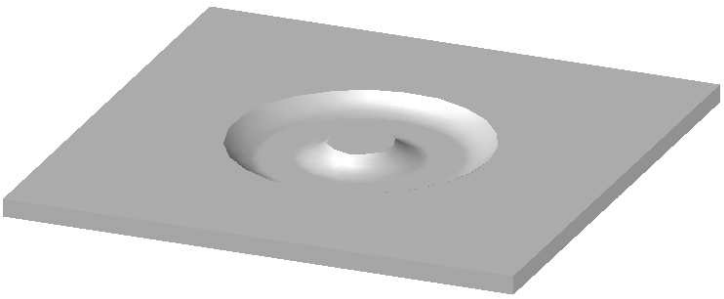

Figure 3.1: Schematic view of the structure studied in the present work. The central circular region is surrounded by a thickness-varying shell so that it is isolated from the propagation of flexural waves on the plate.

Figure 3.1 shows a schematic view of the gradient index device. It consist of a circularly symmetric region in which the thickness of the plate is gradually changed according to the desired functionality. In this case, a well-like profile is drilled surrounding a central area, which is the region to be isolated from external vibrations. Following the results obtained in chapter 2, the objective of the decreasing height (increasing refractive index) region is to act as an "attractive" potential, so that

it tends to concentrate vibrations, while the inner region of increasing height (decreasing refractive index) will act as a "repulsive" potential, isolating in this way the central region. All waves traveling around this device will be concentrated at the bottom of the well where they will be dissipated.

The dissipation is obtained by placing an absorptive material in contact with the plate in the region between the attractive and the repulsive potential. As explained in section 1.8, when the thickness of the plate decreases, the amplitude of the wave increases. Thus, the ideal place to place the absorptive layer is at the bottom of the well. The plate-absorptive system can be described as an effective metamaterial making use of the Ross-Kerwin-Ungar (RKU) model.

3.1.1 RKU absorbing layer model

Using the Ross-Kerwin-Ungar (RKU) model [64] it is possible to describe the system plate-absorptive material as a single composite.

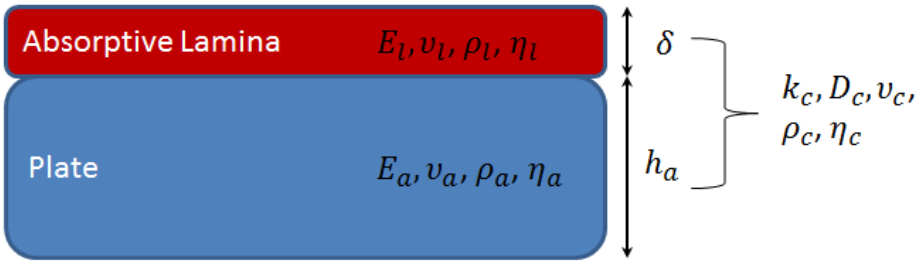

Figure 3.2: Scheme of a binary system composed of an absorbing layer (thickness δ) placed on the top a the plate (thickness h_a). Each layer has its own elastic parameters that combine to produce a composite material (thickness h_c), with new elastic parameters.

Lets us suppose a plate composed of two perfectly bonded layers made of different isotropic materials. The lower material has a thickness of h_a, while the upper one is an absorptive materials of thickness δ, as shown in Fig. 3.2. Each material is characterized by the Young's modulus E_i,

the mass density ρ_i and the Poisson's ratio ν_i. Absorption is introduced in the model by adding a complex part in the Young modulus called the loss factor η, such that $\hat{E} = E(1 + i\eta)$. The sub-indices a and ℓ stands for the parameters of the plate and absorbing layer, respectively.

The RKU model states that the binary system can be described as a single layer with a given Young modulus E_c, thickness h_c, Poisson ration ν_c and mass density ρ_c. Then, the wavenumber of the composite material is defined as

$$k_c = \left(\frac{12\omega^2 \rho_a (1 - \nu_a^2)}{E_a h_a^2} \left[\frac{1 + \rho_r h_r}{(1 - i\eta_a) + (1 - i\eta_\ell) h_r E_r \alpha} \right] \right)^{\frac{1}{4}}, \tag{3.1.1}$$

where $\rho_r = \rho_\ell / \rho_a$, $h_r = \delta / h_a$, $E_r = E_\ell / E_a$ and $\alpha = 3 + 6h_r + 4h_r^2$.

The thickness of the composite is simply the total thickness of the two layers

$$h_c = h_a + \delta, \tag{3.1.2}$$

while its density is the volume average of the densities of the two materials

$$\rho_c = \frac{\rho_a h_a + \rho_\ell \delta}{h_c}. \tag{3.1.3}$$

It is assumed that the Poisson ration of the composite is the same as that of the plate,

$$\nu_c = \nu_a. \tag{3.1.4}$$

From Eqs.(3.1.1)-(3.1.4), the flexural stiffness is cast as

$$D_c = \frac{\omega^2 \rho_c h_c}{k_c^4} = \frac{h_a^3}{12(1 - \nu_a^2)} E_a \left[(1 + h_r E_r \alpha) - i(\eta_a + \eta_\ell h_r E_r \alpha) \right]. \tag{3.1.5}$$

Finally, knowing that $E_c = D_c 12(1 - \nu_c^2)/h_c^3$, the Young modulus of the composite is obtained and its loss factor is found as

$$\eta_c = \frac{\Im\{E_c\}}{\Re\{E_c\}} = \frac{\eta_a + \eta_\ell h_r E_r \alpha}{1 + h_r E_r \alpha}. \tag{3.1.6}$$

Notice that neither the mass density nor the Poisson's ratio affect the composite loss factor.

RKU model tests

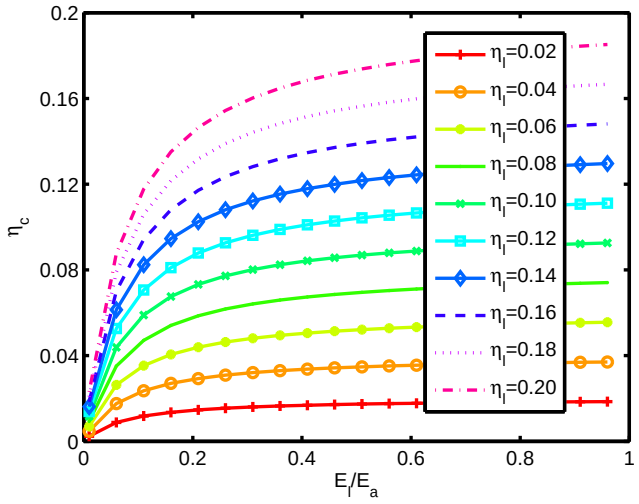

Figure 3.3: Variation of the composite loss factor η_c with the normalized Young's Modulus $E_r = E_\ell/E_a$, for different values of the loss factor of the absorptive layer η_ℓ. ($h_a = 0.5$ mm and $\delta = 0.5$ mm)

To better understand the behavior of the loss factor given by Eq. (3.1.6), some numerical experiments where conducted. Figure 3.3 shows the variation of the composite loss factor with E_r for different values of η_ℓ. The thickness of the aluminum plate is $h_a = 0.5$ mm and the thickness of the layer is $\delta = 0.5$ mm. It is observed that η_c approaches the loss factor of the absorptive layer η_ℓ as the normalized Young's Modulus $E_r >> 0.5$, as expected from Eq. (3.1.6). Figure 3.4 shows how the composite loss factor changes with the h_a and δ. Note that when the thickness of the

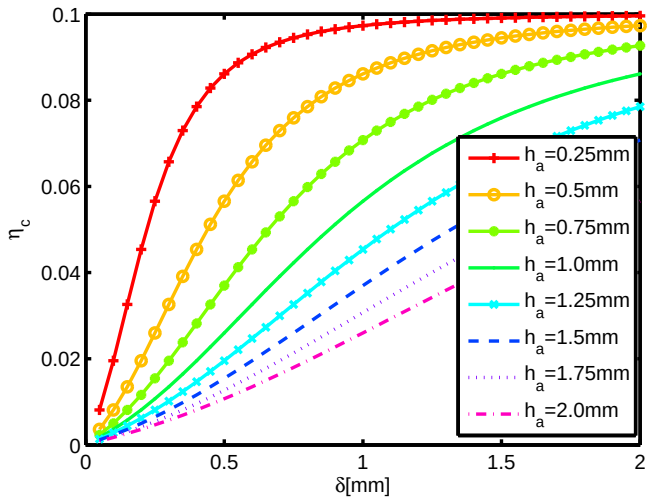

Figure 3.4: Variation of the composite loss factor η_c with the thickness of the layer δ for different plate thickness h_a.

plate decreases, a minor change in the thickness of the layer changes the loss factor greatly.

3.2 Design and Optimization

The insulating device is designed and optimized to obtain maximum transmission between each region, so the geometric and elastic properties are given and the optimization process is described.

The insulating device consists of five regions shown in Fig. 3.5a, i.e. the background (gray), the attractive potential (blue), the absorptive (red), the repulsive potential (green) and, finally, the core region (yellow). Figure 3.5b shows the variation of the thickness of the plate according to the following function

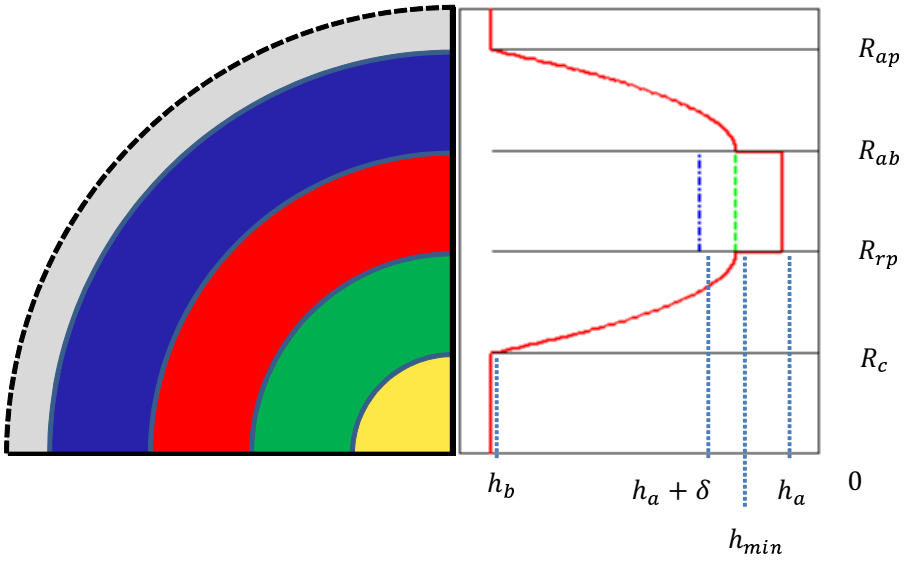

Figure 3.5: (a) Schematic view of the different regions defined in the insulating device and (b) variation of the thickness of the plate. The core is defined by $r < R_c$ (yellow) and corresponds to the area to be isolated from vibrations. Region $R_c < r \leq R_{rp}$ is the repulsive potential shell (green), region $R_{rp} < r \leq R_{ab}$ is the absorbing shell (red) and region $R_{ab} < r \leq R_{ap}$ is the attractive potential shell (blue). The gray region ($r > R_{ap}$) corresponds to the background and it extents towards infinity.

$$h(r) = \begin{cases} h = h_b & r \leq R_c \\ h = \frac{h_b - h_{min}}{(R_c - R_{rp})^2}(r - R_{rp})^2 + h_{min} & R_c < r \leq R_{rp} \\ h = h_{min} & R_{rp} < r \leq R_{ab} \\ h = \frac{h_b - h_{min}}{(R_{ap} - R_{ab})^2}(r - R_{ab})^2 + h_{min} & R_{ab} < r \leq R_{ap} \\ h = h_b & R_{ap} < r \end{cases} \tag{3.2.1}$$

where $h_b = 10mm$ is the thickness of the plate in the background, $h_{min} = 0.5mm$ is the minimum thickness of the plate (prior to the optimization process), $R_c = 15cm$ is the radius of the core, $R_{rp} = 30cm$ is the radius of the "repulsive potential" shell, $R_{ab} = 45cm$ is the radius of the absorptive

shell and $R_{ap} = 60cm$ is the radius of the "attractive potential" shell. Notice that the normalized thickness of the plate is $h_b/R_{ap} = 0.0167$, so the variation in thickness is very smooth.

Table 3.2.1: Elastic parameters of the binary systems materials

	Aluminum	Molded Polyester
Young modulus E	78.97 Gpa	7.8 Gp
Mass density ρ	2700 kg/m^3	1400 kg/m^3
Poisson ratio ν	0.33	0.34
Loss factor η	0.0001	0.1

The background plate is made of aluminum while the absorbing layer is made of molded Polystyrene. The elastic parameters are reported in Table 3.2.1, whose values were obtained from [6]. Given that the thickness of both the absorptive layer and the plate can be tailored, their values are optimized in order to maximize the device's efficiency.

To maximize the energy transfer through all the layers, the system requires a good matching between each interface, so that the reflections of incoming waves be minimum. As explained in chapter 1, the boundary conditions are continuity of the displacement W, its radial derivative $\partial_r W$, the conservation of the bending moment and the generalized Kirchhoff stress, as given by Eqs. (1.3.19). These equations are functions of the flexural stiffness $D(r)$ and the wavenumber $k(r)$ (ν does not change), so that, in order to minimize reflections when changing from one region to the other one, these values have to be continuous.

Although the thickness values given from Eq. (3.2.1) provides this continuity, once the effect of the absorbing layer is added, a mismatch between the layers surrounding the absorptive shell occurs. An optimization process solves this problem. Two parameters have been optimized, the thickness of the absorbing layer (δ) and the thickness of the absorbing plate ($h_a \leq h_{min}$). Figure 3.5b shows, in the absorption region, the original value h_{min} (dashed line), the new thickness value $h_a < h_{min}$ (continuous line) and, finally, and the total thickness after adding the

absorbing layer $h_a + \delta$ (dash-dotted line). The goal is to obtain a relative error lower than 0.1% for the flexural stiffness and the wavenumber, i.e.

$$\epsilon_{D(r)} = |D(r)_{target} - D(r)|/D(r)_{target} \tag{3.2.2a}$$

$$\epsilon_{k(r)} = |k(r)_{target} - k(r)|/k(r)_{target} \tag{3.2.2b}$$

of less than 0.1%. After the optimization, the values for the new thickness of the plate and the layer are $h_a = 0.44 h_{min}$ and $\delta = 0.55mm$, respectively. Also, the composite loss factor achieved was $\eta_c \approx 0.1$.

3.3 Numerical simulations

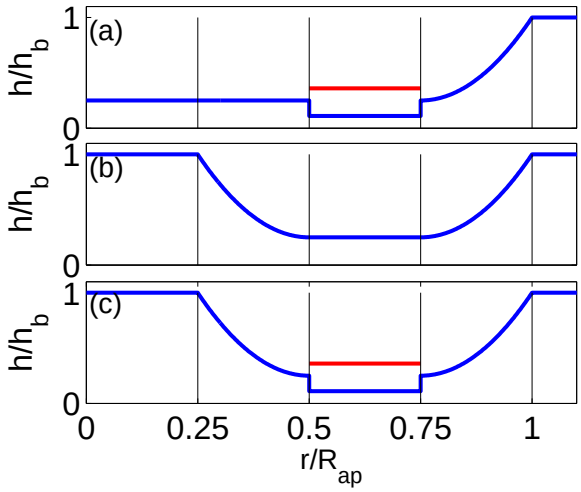

Figure 3.6: Thickness variation as a function of the distance r for the three structures studied in this work. The region wanted to be free of vibration is $r \leq R_{ap}/4$. (a) Attractive potential with the absorptive layer. (b) Attractive and repulsive potentials without the absorptive layer. (c) Full isolating device.

Using this design, numerically simulations were conducted by means of the multiple layer scattering method, described in chapter 1.6. This

method requires the application of the proper boundary conditions at each layer, for which it is necessary to know their physical properties. Note that the only parameter that changes from layer to layer is the plate's thickness, except at the bottom of the well, where a dissipative material is placed. Each region has been discretized into $N = 100$ layers, which has been shown to be a good approximation to the ideal continuous device for the wavelengths of interest.

For comparison purposes, the three configurations shown in Fig. 3.6 have been studied. The first one is a device with the same geometrical characteristics as the designed one, but without the repulsive potential (Fig. 3.6a); the second one is a device with the same geometrical characteristics as the designed one, but without the absorptive layer and the optimization (Fig. 3.6b); and the third one is the designed device (Fig.3.6c).

To further understand what is occurring inside the three configurations, let us consider the displacement fields illustrated in Fig. 3.7. They show the modulus of the displacement in the z-direction when a plane wave with wavenumbers $kR_{ap} = 15$ (upper panels) and $kR_{ap} = 35$ (lower panels), impinges the devices under study. The white circles represent the boundaries defined by Eq. (3.2.1). Plots (a) represent the displacement without the repulsive potential. Notice that, although the system presents absorption, the wave is focused into the core and a high amplitude is achieved. Panels (b) are for the device without the absorptive layer, but adding the repulsive potential shell. It is observed that the wave is expelled from the core and the amplitude decreases in comparison to the previous panels, even though it does not have absorption. Finally, plots (c) correspond to the designed optimum device. By introducing the absorptive layer, the wave amplitude in the core is further reduced. Notice that the panel in the second row has the same pattern as the one in the third row but without the attenuation.

For comparison purposes we have introduced the vibration average in the region i defined as

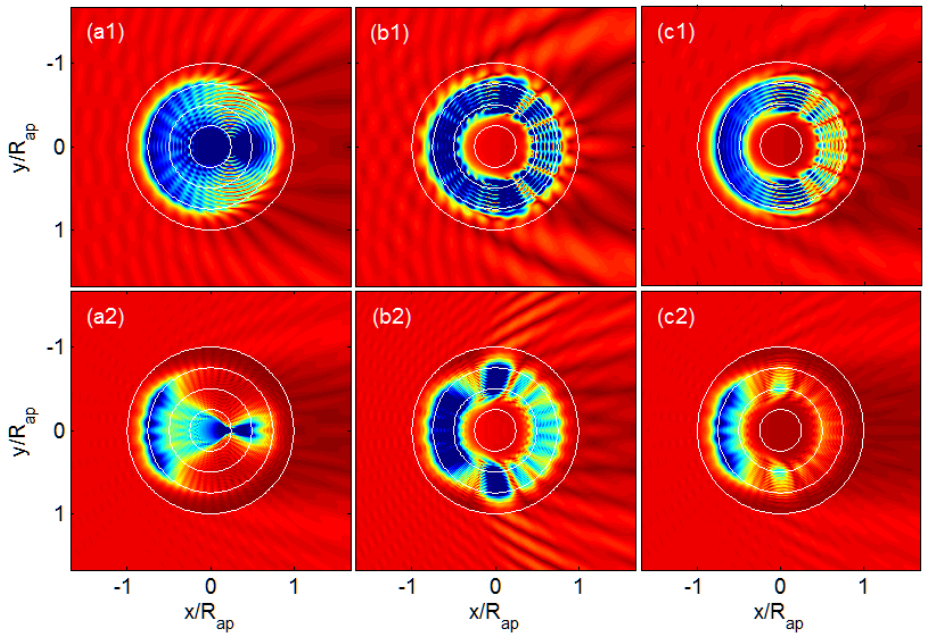

Figure 3.7: Modulus of the displacement in the z-direction when a plane wave with wavenumber $kR_{ap} = 15$ (upper panels) and $kR_{ap} = 35$ (lower panels) impinges on the three devices tested in this work. Displacement produced by (a) the device without the repulsive potential, (b) by the device without absorption and (c) by the designed device.

$$< |W|^2 >_i = \frac{1}{S_i} \iint_{S_i} |W(r,\theta)|^2 dS, \tag{3.3.1}$$

where S_i is the area defined by $R_i < r < R_{i+1}$, with $R_i \in [\infty, R_{ap}, R_{ab}, R_{rp}, R_c, 0]$.

The plots a,b,c and d in Fig 3.8 show the vibration average produced in the four regions defining the device: the attractive potential shell, the absorbing shell, the repulsive shell and the core, respectively. Each figure shows the values of the vibration average for the designed device (continuous line), the device without absorption shell (dashed line) and the device without the repulsive potential shell (dotted line). Notice that in general, the vibration average decreases with increasing frequency, due

to the frequency response of the absorptive layer. Some peaks are observed in the device without the absorption shell due to resonances of the structure, which disappear once dissipation is introduced in the device. Overall, the designed device has the minimum vibration average in all the regions, which shows its efficiency not only for dissipating vibration energy but also for isolating a given region from these vibrations.

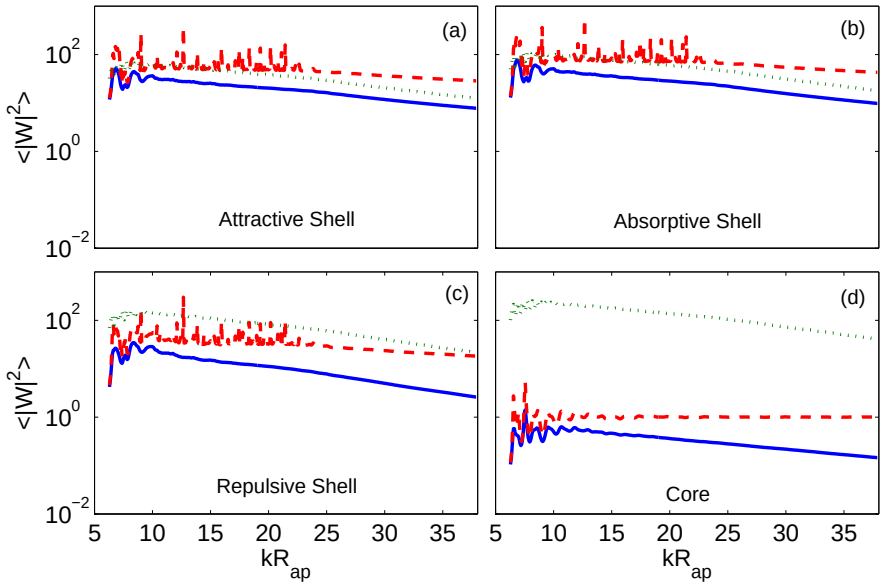

Figure 3.8: Vibration average in (a) the attractive potential shell, (b) the absorptive shell, (c) the repulsive shell and (d) the core. The lines correspond to the designed device (continuous line), the device without absorption (dashed line) and the device without repulsive potential shell (dotted line).

Chapter 4

Flexural resonator

This chapter describes the mathematical analysis of an in-plane flexural resonator. First the problem is described and solved, giving information on how to couple the Euler-Bernoulli beam and the Kirchhoff-Love plate equation of motions. Here the T-matrix is obtained through an impedance method instead of that described in chapter 1. Then, numerical simulations are presented and the results prove the efficiency of the method.

4.1 Introduction

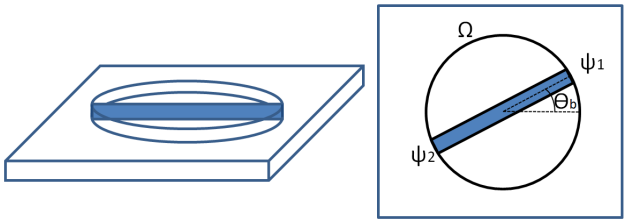

Figure 4.1: 3D Scheme (a) and 2D scheme (b) of a thin plate with a hole (cylindrical boundary Ω) traversed by a beam (oriented at angle of θ_b) connected to the plate at two anchor points (Ψ_i; $i = 1, 2$)

Figure 4.1 shows a 3D scheme (a) and a 2D scheme (b) of the system here analyzed. A flexural wave with linear wavefront is incident in an arbitrary direction on a hole (cylindrical boundary Ω) in the thin plate. Inside, there is a beam connected to the plate at two anchor points (Ψ_i; $i = 1, 2$). The beam is inclined an angle of θ_b. The motion of the flexural wave W interacts with the motion of the beam V and creates a scattered wave.

4.1.1 Coupling Boundary Conditions

To couple the two equations of motion we make use of the boundary conditions. From Eq. (1.3.23), the boundary conditions for a hole in a thin plate are $M_r = 0$ and $V_r = 0$ at the boundary Ω. For the problem considered, the beam introduces additional conditions at the anchor points in Ψ_i requiring that the displacement and the slope are continuous and the sum of the moments and the sum of the stresses are zero. Then, from chapter 1, the displacement W of the plate can be expressed as

$$W = \sum_q W_q(r)e^{iq\theta} = \sum_q \left[W_q^{inc}(r) + W_q^{scat}(r)\right]e^{iq\theta}$$
$$= \sum_q \left[A_q^{(J)}J_q(k_b r) + A_q^{(I)}I_q(k_b r) + B_q^{(H)}H_q(k_b r) + B_q^{(K)}K_q(k_b r)\right]e^{iq\theta}, \tag{4.1.1}$$

and the displacement V of the beam can be expressed as

$$V(x) = C^I e^{+ik_b x} + C^{II}e^{-ik_b x} + D^I e^{+k_b x} + D^{II}e^{-k_b x} \tag{4.1.2}$$

Along this chapter, both displacements are positive in the positive $\hat{z}$-axis. Also, a positive slope is represented as an inclined black line. The moments in a 3D figure are represented using the double-headed arrow notation and the right-hand grip rule. In the case of a 2D figure, $\otimes$ and $\odot$ represent an ingoing and outgoing double arrow, respectively. Finally, the shear stresses are defined with a single-headed arrow.

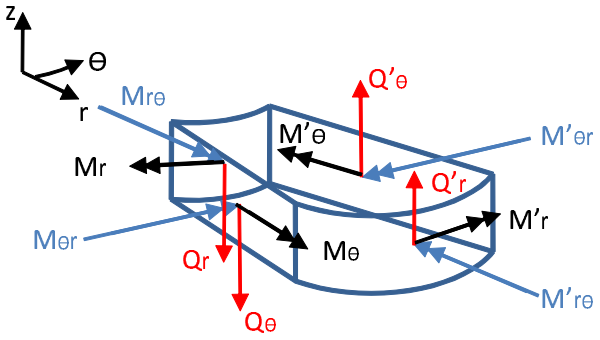

Figure 4.2: Scheme of the direction of all the moments and shear stresses defined by the Kirchhoff-Love plate theory. Notice that $M'_{ij} = M_{ij} + (\partial M_{ij}/\partial x_i)dx_i$ and $Q'_{ij} = Q_{ij} + (\partial Q_{ij}/\partial x_i)dx_i$

Figure 4.2 shows all the moments and shear stresses defined for the Kirchhoff-Love plate theory. Notice that $M'_{ij} = M_{ij} + (\partial M_{ij}/\partial x_i)dx_i$

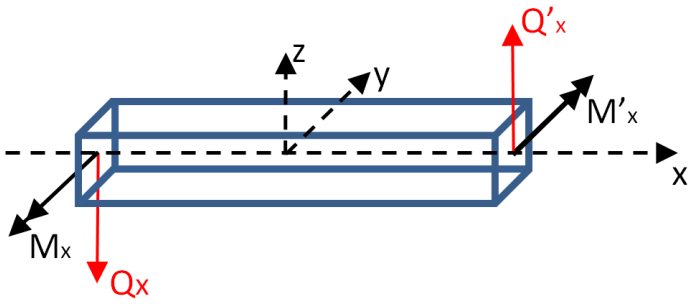

Figure 4.3: Scheme of the direction of all the moments and shear stresses defined by the Euler-Bernoulli beam theory. Notice that $M'_x = M_x + (\partial M_x/\partial x)dx$ and $Q'_x = Q_x + (\partial Q_x/\partial x)dx$

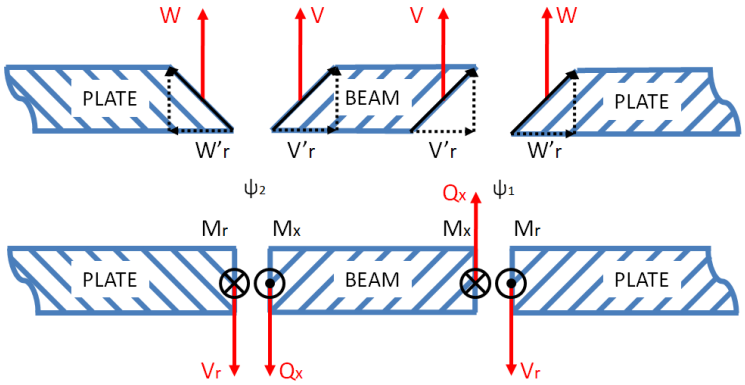

Figure 4.4: Scheme of the boundary conditions, displacements (W, V), slopes (W'_r, V'_r), moments (M_r, M_x) and shear stresses (V_r, Q_x), between the plate and the beam at the two anchor points Ψ_1 and Ψ_2.

and $Q'_{ij} = Q_{ij} + (\partial Q_{ij}/\partial x_i)dx_i$. In a similar way, Fig. 4.3 displays the direction of the moments and shear stresses defined for the Euler-Bernoulli beam theory. Notice that $M'_x = M_x + (\partial M_x/\partial x)dx$ and $Q'_x = Q_x + (\partial Q_x/\partial x)dx$.

Finally, Fig. 4.4 shows the plate and the beam together. Ψ_1 is the right anchor point at $(r, \theta) = (R, 0)$ and $(x) = (+R)$; and Ψ_2 is the left anchor point at $(r, \theta) = (R, \pi)$ and $(x) = (-R)$. The upper panel shows the displacements and the slopes and the lower panel shows the moments

and the shear stresses. Notice that the Kirchhoff Stress is defined as $V_r = Q_r - (1/r)\partial M_{r\theta}/\partial\theta$ so its direction is the same as Q_r.

The boundary conditions require that at the anchor points Ψ_i the displacement and the slope are continuous and the sum of the moments and the sum of the stresses are zero. Looking at the two panels shown in Fig. 4.4 it is easy to obtain them as

$$W(R,0) = V(R) \qquad \text{and} \qquad W(R,\pi) = V(-R), \tag{4.1.3a}$$

$$\left.\frac{\partial W}{\partial r}\right|_{\substack{r=R\\ \theta=0}} = \left.\frac{\partial V}{\partial x}\right|_{x=R} \qquad \text{and} \qquad \left.\frac{\partial W}{\partial r}\right|_{\substack{r=R\\ \theta=\pi}} = -\left.\frac{\partial V}{\partial x}\right|_{x=-R}, \tag{4.1.3b}$$

$$M_r|_{\substack{r=R\\ \theta=0}} = \left.\frac{M_x}{R}\right|_{x=R} \qquad \text{and} \qquad M_r|_{\substack{r=R\\ \theta=\pi}} = \left.\frac{M_x}{R}\right|_{x=-R}, \tag{4.1.3c}$$

$$V_r|_{\substack{r=R\\ \theta=0}} = \left.\frac{Q_x}{R}\right|_{x=R} \qquad \text{and} \qquad V_r|_{\substack{r=R\\ \theta=\pi}} = -\left.\frac{Q_x}{R}\right|_{x=-R}. \tag{4.1.3d}$$

Notice that the moments and the shear stresses of the beam are divided by the radius R of the hole. It is useful to take into account the dimension of each term. The moment of the plate, M_r, has dimensions of $[N]$ while the moment of the beam, M_x, has dimensions of $[Nm]$. At the same time, the Kirchhoff Stress, V_r, has dimension of $[N/m]$ and the shear stress, Q_x, has dimensions of $[N]$. Therefore, if we integrate over a differential element ϵ

$$\int_{0-\epsilon}^{0+\epsilon} M_r(\theta) R d\theta = M_x, \tag{4.1.4a}$$

$$\int_{0-\epsilon}^{0+\epsilon} V_r(\theta) R d\theta = Q_x, \tag{4.1.4b}$$

we see that an additional term $1/R$ has to be added to the moments and the shear stresses of the beam.

4.1.2 T-Matrix Solution: Impedance Method

Once the boundary conditions are known both equations of motion can be coupled. Instead of using the approximation explained in chapter 1, here

an impedance method for flexural waves that is analogous to the one described for acoustic waves by Bobrovnitskii in [7] is here developed. The method consists in obtaining the T-matrix of an interface as the combination of three impedance matrices. Two of them describe the background and the third one describes the internal media.

The T-Matrix is defined as $\mathbf{B} = \mathbf{TA}$, relating the incident wave amplitudes to the scattered amplitudes. Using Einstein notation it becomes $\mathbf{B}_q = \mathbf{T}_{qs}\mathbf{A}_s$ where

$$\mathbf{A}_s = \begin{bmatrix} A_s^{(J)} \\ A_s^{(I)} \end{bmatrix} \; ; \mathbf{B}_q = \begin{bmatrix} B_q^{(H)} \\ B_q^{(K)} \end{bmatrix} \; ; \mathbf{T}_{qs} = \begin{bmatrix} T_{11} & T_{12} \\ T_{21} & T_{22} \end{bmatrix} \tag{4.1.5}$$

.

In [7] the impedance matrices were defined by the relation between the pressure P and the particle velocity v at the boundary Ω. Notice, that the boundary condition for a fluid-rigid interface is $v = 0$ and for a fluid-vacuum interface is $P = 0$. In the case of a thin plate, the boundary conditions for a plate-clamped interface are $W = W_r' = 0$ and for a plate-fluid interface are $M_r = V_r = 0$. By analogy, we can define a new set of impedance matrices as

$$\begin{bmatrix} M_r \\ V_r \end{bmatrix}_q^{(inc)} = -\mathbf{Z}_{qs}^{(inc)} \begin{bmatrix} W \\ W_r' \end{bmatrix}_s^{(inc)} , \qquad \text{at } \Omega \tag{4.1.6a}$$

$$\begin{bmatrix} M_r \\ V_r \end{bmatrix}_q^{(scat)} = \mathbf{Z}_{qs}^{(scat)} \begin{bmatrix} W \\ W_r' \end{bmatrix}_s^{(scat)} , \qquad \text{at } \Omega \tag{4.1.6b}$$

$$\left(\begin{bmatrix} M_r \\ V_r \end{bmatrix}_q^{(inc)} + \begin{bmatrix} M_r \\ V_r \end{bmatrix}_q^{(scat)} \right) = -\mathbf{Z}_{qs} \left(\begin{bmatrix} W \\ W_r' \end{bmatrix}_s^{(inc)} + \begin{bmatrix} W \\ W_r' \end{bmatrix}_s^{(scat)} \right) . \qquad \text{at } \Omega \tag{4.1.6c}$$

where $\mathbf{Z}_{qs}^{inc}$, $\mathbf{Z}_{qs}^{scat}$, and $\mathbf{Z}_{qs}$ are the impedances for the incoming, scattered and internal wave, respectively. Notice that they are defined at

the boundary Ω. Solving from Equations (4.1.6) we obtain the following relationship

$$\begin{bmatrix} W \\ W'_r \end{bmatrix}_q^{(scat)} = \tilde{\mathbf{T}}_{qs} \begin{bmatrix} W \\ W'_r \end{bmatrix}_s^{(inc)}, \tag{4.1.7}$$

where

$$\tilde{\mathbf{T}}_{qs} = [\mathbf{Z}_{qs}^{scat} + \mathbf{Z}_{qs}]^{-1}[\mathbf{Z}_{qs}^{inc} - \mathbf{Z}_{qs}]. \tag{4.1.8}$$

It is noticed that $\tilde{\mathbf{T}}$ relates the displacement and the slope of the incoming and scattered wave at the boundary between the two media. In the case of a circular region in a plate, these are given by

$$\begin{bmatrix} W \\ W'_r \end{bmatrix}_q^{(inc)} = \begin{bmatrix} J_q(k_pR) & I_q(k_pR) \\ k_pJ'_q(k_pR) & k_pI'_q(k_pR) \end{bmatrix} \begin{bmatrix} A_q^{(J)} \\ A_q^{(I)} \end{bmatrix} e^{iq\theta} = \begin{bmatrix} \tilde{A}_q^{(J)} \\ \tilde{A}_q^{(I)} \end{bmatrix} e^{iq\theta}, \tag{4.1.9a}$$

$$\begin{bmatrix} W \\ W'_r \end{bmatrix}_q^{(scat)} = \begin{bmatrix} H_q(k_pR) & K_q(k_pR) \\ k_pH'_q(k_pR) & k_pK'_q(k_pR) \end{bmatrix} \begin{bmatrix} B_q^{(H)} \\ B_q^{(K)} \end{bmatrix} e^{iq\theta} = \begin{bmatrix} \tilde{B}_q^{J} \\ \tilde{B}_q^{(I)} \end{bmatrix} e^{iq\theta}. \tag{4.1.9b}$$

Notice that $\tilde{B} = \tilde{\mathbf{T}}\tilde{A}$, from which it is easy to obtain the matrix $\mathbf{T}$ as a function of $\tilde{\mathbf{T}}$,

$$\mathbf{T}_{qs} = [\mathbf{M}_{qq}^{HK}(k_p)]^{-1} \quad [\mathbf{Z}_{qs}^{scat} + \mathbf{Z}_{qs}]^{-1}[\mathbf{Z}_{qs}^{inc} - \mathbf{Z}_{qs}] \quad [\mathbf{M}_{ss}^{JI}(k_p)], \tag{4.1.10}$$

where $\mathbf{M}$ is a quasi-diagonal matrix defined as

$$\mathbf{M}_{qq}^{\Upsilon\Phi}(k_i) = \begin{bmatrix} \Upsilon_q(k_iR) & \Phi_q(k_iR) \\ k_i\Upsilon'_q(k_iR) & k_i\Phi'_q(k_iR) \end{bmatrix}. \tag{4.1.11}$$

Background Impedances

Based on the definitions of Eq. (4.1.6a) and (4.1.6b), the background impedances are obtained as

$$\mathbf{Z}_{qq}^{(inc)} = -\mathbf{N}_{qq}^{JI}(k_p)\,[\mathbf{M}_{qq}^{JI}(k_p)]^{-1}, \tag{4.1.12a}$$

$$\mathbf{Z}_{qq}^{(scat)} = \mathbf{N}_{qq}^{HK}(k_p)\,[\mathbf{M}_{qq}^{HK}(k_p)]^{-1}, \tag{4.1.12b}$$

where

$$\mathbf{N}_{qq}^{\Upsilon\Phi}(k_i) = \begin{bmatrix} S_q^{\Upsilon}(k_i) & S_q^{\Phi}(k_i) \\ \\ T_q^{\Upsilon}(k_i) & T_q^{\Phi}(k_i) \end{bmatrix}, \tag{4.1.13}$$

and $S_q^{\xi}(k_i) \equiv S_q^{\xi}(k_r, R)$ and $T_q^{\xi}(k_i) \equiv T_q^{\xi}(k_r, R)$ are defined in Eq. (1.4.9) and (1.4.10), respectively.

Internal Impedance

The following procedure is used to obtain the third impedance matrix required for the solution, which is associated with the internal beam. On the circular boundary Ω we have, $(M_r = 0, V_r = 0)\ \forall\theta$ except for ($\theta = 0$, $\theta = \pi$), hence the two boundary conditions (4.1.3c) and (4.1.3d) can be rewritten as

$$M_r(\theta)|_{r=R} \equiv M_x(\theta) = \frac{1}{R}\left[M_x(R)\delta(\theta - \theta_{\Psi_1}) + M_x(-R)\delta(\theta - \theta_{\Psi_2})\right], \tag{4.1.14a}$$

$$V_r(\theta)|_{r=R} \equiv Q_x(\theta) = \frac{1}{R}\left[Q_x(R)\delta(\theta - \theta_{\Psi_1}) - Q_x(-R)\delta(\theta - \theta_{\Psi_2})\right]. \tag{4.1.14b}$$

Knowing that $\theta_{\Psi_1} = \theta_b$ and $\theta_{\Psi_2} = \theta_b + \pi$ and expanding Eqs. (4.1.14a) and (4.1.14b) in azimuthal orders, using $\delta(\theta - \theta_i) = \frac{1}{2\pi}\sum_q e^{iq(\theta-\theta_i)}$, we obtain

$$M_x(\theta) = \sum_q M_q e^{iq\theta} = \frac{1}{2\pi R} \sum_q \left[M_x(R) + (-1)^q M_x(-R) \right] e^{iq(\theta-\theta_b)}, \tag{4.1.15a}$$

$$Q_x(\theta) = \sum_q Q_q e^{iq\theta} = \frac{1}{2\pi R} \sum_q \left[Q_x(R) - (-1)^q Q_x(-R) \right] e^{iq(\theta-\theta_b)}. \tag{4.1.15b}$$

These equations can be combined and rewritten in matrix form as

$$\begin{bmatrix} M_x \\ Q_x \end{bmatrix}_q = \frac{e^{-iq\theta_b}}{2\pi R} \left(\begin{bmatrix} M_R \\ Q_R \end{bmatrix} + (-1)^q \begin{bmatrix} M_{-R} \\ -Q_{-R} \end{bmatrix} \right). \tag{4.1.16}$$

The two unused boundary condition, state that the displacement and the slope have to be continuous in the anchor points, so it is necessary to express the moment and shear forces in the anchor points as a combination of the displacements and the slopes at both sides of the beam.

From the definition of the displacement of the beam, Eq. (4.1.2), we can write the following matrix

$$\begin{bmatrix} V(x) \\ V'(x) \\ V''(x) \\ V'''(x) \end{bmatrix} = \begin{bmatrix} (ik_b)^0 e^{ik_b x} & (-ik_b)^0 e^{-ik_b x} & (k_b)^0 e^{k_b x} & (-k_b)^0 e^{-k_b x} \\ (ik_b)^1 e^{ik_b x} & (-ik_b)^1 e^{-ik_b x} & (k_b)^1 e^{k_b x} & (-k_b)^1 e^{-k_b x} \\ (ik_b)^2 e^{ik_b x} & (-ik_b)^2 e^{-ik_b x} & (k_b)^2 e^{k_b x} & (-k_b)^2 e^{-k_b x} \\ (ik_b)^3 e^{ik_b x} & (-ik_b)^3 e^{-ik_b x} & (k_b)^3 e^{k_b x} & (-k_b)^3 e^{-k_b x} \end{bmatrix} \begin{bmatrix} C^I \\ C^{II} \\ D^I \\ D^{II} \end{bmatrix}. \tag{4.1.17}$$

Evaluating this at the end points $x = \pm R$, simplifying and ordering terms we obtain

$$\begin{bmatrix} V(-R) \\ V'(-R) \\ V(R) \\ V'(R) \end{bmatrix} = \mathbf{L}_1 \begin{bmatrix} C^I \\ C^{II} \\ D^I \\ D^{II} \end{bmatrix} \quad \text{and} \quad \begin{bmatrix} V''(-R) \\ V'''(-R) \\ V''(R) \\ V'''(R) \end{bmatrix} = k_b^2 \mathbf{L}_2 \begin{bmatrix} C^I \\ C^{II} \\ D^I \\ D^{II} \end{bmatrix}, \tag{4.1.18}$$

where

$$\mathbf{L}_1 = \begin{bmatrix} e^{-ik_bR} & e^{ik_bR} & e^{-k_bR} & e^{k_bR} \\ ik_be^{-ik_bR} & -ik_be^{ik_bR} & k_be^{-k_bR} & -k_be^{k_bR} \\ e^{ik_bR} & e^{-ik_bR} & e^{k_bR} & e^{-k_bR} \\ ik_be^{ik_bR} & -ik_be^{-ik_bR} & k_be^{k_bR} & -k_be^{-k_bR} \end{bmatrix}, \tag{4.1.19a}$$

$$\mathbf{L}_2 = \begin{bmatrix} -e^{-ik_bR} & -e^{ik_bR} & e^{-k_bR} & e^{k_bR} \\ -ik_be^{-ik_bR} & ik_be^{ik_bR} & k_be^{-k_bR} & -k_be^{k_bR} \\ -e^{ik_bR} & -e^{-ik_bR} & e^{k_bR} & e^{-k_bR} \\ -ik_be^{ik_bR} & ik_be^{-ik_bR} & k_be^{k_bR} & -k_be^{-k_bR}. \end{bmatrix} \tag{4.1.19b}$$

Taking into account the required boundary conditions Eqs. (4.1.3), the sign of some rows has to change. Therefore

$$\mathbf{L}_1' = \begin{bmatrix} 1 & & & \\ & -1 & & \\ & & 1 & \\ & & & 1 \end{bmatrix} \mathbf{L}_1 \quad ; \quad \mathbf{L}_2' = \begin{bmatrix} 1 & & & \\ & -1 & & \\ & & 1 & \\ & & & 1 \end{bmatrix} \mathbf{L}_2. \tag{4.1.20}$$

By combining the three previous equations, we obtain the moment and the shear stress as function of the displacement and the slope as

$$\begin{bmatrix} M_{-R} \\ -Q_{-R} \\ M_R \\ Q_R \end{bmatrix} = -EIk_b^2[\mathbf{L}_2'][\mathbf{L}_1']^{-1} \begin{bmatrix} V_{-R} \\ -V_{-R}' \\ V_R \\ V_R' \end{bmatrix} = \mathbf{K} \begin{bmatrix} V_{-R} \\ -V_{-R}' \\ V_R \\ V_R' \end{bmatrix} \tag{4.1.21}$$

where the 4×4 Stiffness Matrix $\mathbf{K}$ is simplified and has the following final form

$$\mathbf{K} = \begin{bmatrix} \mathbf{K}_1 & \mathbf{K}_2 \\ \\ \mathbf{K}_2 & \mathbf{K}_1 \end{bmatrix} = \frac{-EIk_b^2}{1-cc_h} \times$$
$$\left[\begin{array}{cc|cc} -ss_h & k_b^{-1}(sc_h - cs_h) & c_h - c & -k_b^{-1}(s_h - s) \\ -k_b(cs_h + sc_h) & ss_h & k_b(s + s_h) & c - c_h \\ \hline c_h - c & -k_b^{-1}(s_h - s) & -ss_h & k_b^{-1}(sc_h - cs_h) \\ k_b(s + s_h) & c - c_h & -k_b(cs_h + sc_h) & ss_h \end{array}\right], \tag{4.1.22}$$

with $c = \cos(2k_bR)$, $s = \sin(2k_bR)$, $c_h = \cosh(2k_bR)$ and $s_h = \sinh(2k_bR)$.

For the purpose of this work it is useful to rewrite Eq. (4.1.21) as two separate relations

$$\begin{bmatrix} M_{-R} \\ -Q_{-R} \end{bmatrix} = \mathbf{K}_1 \begin{bmatrix} V_{-R} \\ -V'_{-R} \end{bmatrix} + \mathbf{K}_2 \begin{bmatrix} V_R \\ V'_R \end{bmatrix}, \tag{4.1.23a}$$

$$\begin{bmatrix} M_R \\ Q_R \end{bmatrix} = \mathbf{K}_2 \begin{bmatrix} V_{-R} \\ -V'_{-R} \end{bmatrix} + \mathbf{K}_1 \begin{bmatrix} V_R \\ V'_R \end{bmatrix}. \tag{4.1.23b}$$

Combining Eqs. (4.1.16) and (4.1.23) yields the following result

$$\begin{bmatrix} M_x \\ Q_x \end{bmatrix}_q = \frac{e^{-iq\theta_b}}{2\pi R} \left[\mathbf{K}_1 + (-1)^q \mathbf{K}_2\right] \left(\begin{bmatrix} V_R \\ V'_R \end{bmatrix} + (-1)^q \begin{bmatrix} V_{-R} \\ -V'_{-R} \end{bmatrix} \right). \tag{4.1.24}$$

The two remaining boundary conditions (4.1.3a) and (4.1.3b) may be written in terms of Fourier coefficients as

$$\begin{bmatrix} V_R \\ V'_R \end{bmatrix} = \sum_s \begin{bmatrix} W_R \\ W'_R \end{bmatrix}_s e^{is\theta_b}, \quad \begin{bmatrix} V_{-R} \\ -V'_{-R} \end{bmatrix} = \sum_s (-1)^s \begin{bmatrix} W_R \\ W'_R \end{bmatrix}_s e^{is\theta_b}. \tag{4.1.25}$$

Combining these boundary conditions with Eq. (4.1.24) we obtain

$$\begin{bmatrix} M_r \\ V_r \end{bmatrix}_q = -\sum_s \mathbf{Z}_{qs} \begin{bmatrix} W_R \\ W'_R \end{bmatrix}_s , \tag{4.1.26}$$

where the 2×2 blocks of the internal impedance matrix are given by

$$\mathbf{Z}_{qs} = -\frac{e^{i(s-q)\theta_b}}{2\pi R}\big(1 + (-1)^{q+s}\big)\big[\mathbf{K}_1 + (-1)^q \mathbf{K}_2\big] \tag{4.1.27}$$

4.2 Scattering and internal coefficients

The results of the previous section are summarized here. This provides in one place simple formulas for the coefficients of the incoming, the scattered and the beam solution.

Incident Wave Coefficients

While the general solution can handle arbitrary incidence here we focus on plane wave or a point source, which will be used in the numerical examples later. The coefficients of an incoming wave, which where described in Chapter 1, for these two possible cases are as follows

$$\mathbf{A}_q = \begin{bmatrix} i^q \\ 0 \end{bmatrix} e^{-iq\theta_s} \qquad \text{for a plane wave in direction } \theta_s, \tag{4.2.1a}$$

$$\mathbf{A}_q = \begin{bmatrix} H_q(k_p R_s) \\ \frac{2i}{\pi} K_q(k_p R_s) \end{bmatrix} e^{-iq\theta_s} \qquad \text{for a point source at } (R_s, \theta_s). \tag{4.2.1b}$$

Scattered Coefficients

The coefficients defining the scattered wave are obtained from $\mathbf{B}_q = \mathbf{T}_{qs}\mathbf{A}_s$ where the T-matrix has 2×2 block elements

$$\mathbf{T}_{qs} = [\mathbf{M}_{qq}^{HK}(k_p)]^{-1} \quad [\mathbf{Z}_{qs}^{scat} + \mathbf{Z}_{qs}]^{-1}[\mathbf{Z}_{qs}^{inc} - \mathbf{Z}_{qs}] \quad [\mathbf{M}_{ss}^{JI}(k_p)], \tag{(4.1.10) revisited}$$

with

$$\begin{aligned}
\mathbf{Z}_{qq}^{(inc)} &= -\mathbf{N}_{qq}^{JI}(k_p)\mathbf{M}_{qq}^{JI}(k_p)^{-1}, && \text{((4.1.12a) revisited)}\\
\mathbf{Z}_{qq}^{(scat)} &= \mathbf{N}_{qq}^{HK}(k_p)\mathbf{M}_{qq}^{HK}(k_p)^{-1}, && \text{((4.1.12b) revisited)}\\
\mathbf{Z}_{qs} &= -\frac{e^{i(s-q)\theta_b}}{2\pi R}\big(1+(-1)^{q+s}\big)\big[\mathbf{K}_1+(-1)^q\mathbf{K}_2\big] && \text{((4.1.27) revisited)}
\end{aligned}$$

where Eqs. (4.1.11), (4.1.13) and (4.1.22) were used in simplifying terms.

Beam Coefficients

The coefficients for the flexural waves in the internal beam are, see Eq. (4.1.2),

$$\begin{bmatrix} C^I \\ C^{II} \\ D^I \\ D^{II} \end{bmatrix} = [\mathbf{L}_1']^{-1} \sum_q \begin{bmatrix} (-1)^q\mathbf{M}_{qq}^{JI}(k_p) & (-1)^q\mathbf{M}_{qq}^{HK}(k_p) \\ \\ \mathbf{M}_{qq}^{JI}(k_p) & \mathbf{M}_{qq}^{HK}(k_p) \end{bmatrix} \begin{bmatrix} A_q^{(J)} \\ A_q^{(I)} \\ B_q^{(H)} \\ B_q^{(K)} \end{bmatrix} e^{iq\theta_b}. \tag{4.2.2}$$

These follow from Eqs. (4.1.9) and (4.1.18).

4.3 Numerical simulations

In this section the theory developed previously is tested to prove its efficiency. Conservation of energy is used as one measure of the accuracy of the method. The results are visually compared against a commercial finite element method (FEM) simulator and the SCS obtained by the analytical simulator are presented over a wide bandwidth.

4.3.1 Energy Flux

The principle of conservation of energy has to be met, so if the system is not capable of absorbing or creating waves, the result of calculating

the energy flux crossing a circle around the system has to be zero. The energy conservation relation is known from a previous result in Chapter 1 as

$$\omega \frac{D}{2} \Im \oint_{\Omega} \left(W \frac{\partial}{\partial r} \Delta W^* - \Delta W^* \frac{\partial W}{\partial r} \right) R d\theta = 0. \tag{4.3.1}$$

Applying this result to our work yields the following relationship which has to be fulfilled by the coefficients $\mathbf{A}_q$ and $\mathbf{B}_q$ if there is no absorption in the medium:

$$4\omega D k_p^2 \sum_q \left(|B_q^{(H)}|^2 + \Re \left\{ (A_q^{(J)})^* B_q^{(H)} \right\} + \frac{\pi}{2} \Im \left\{ (A_q^{(I)})^* B_q^{(K)} \right\} \right) = 0. \tag{4.3.2}$$

Equation (4.3.2) was used to verify all of the numerical calculations.

4.3.2 Commercial FEM Simulator

A commercial finite element simulator has been used to calculate the behavior of the system. This simulator solves the full elastic equation (including longitudinal, shear vertical and shear horizontal waves) to calculate the displacement field in a 3D model of the system. As incoming wave we have selected a plane wave ($\theta_s = 0$) at three values of the non-dimensional frequency, $k_p R = [\pi, 2\pi, 5\pi]$. The system is also considered for three possible orientations of the internal beam: $\theta_b = [0°, -45°, -90°]$, see Fig. 4.1. The data is subsequently exported and compared visually against the analytical simulator coded using the theory described in the previous section.

The FEM simulator runs in an Intel Core i7-3930K @ 3.2Ghz machine with 32GB of RAM. Each simulation shown in Figs. 4.5 and 4.6 required 192.000 free tetrahedral elements to mesh the whole 3D volume and took approximately one hour to finish. The ones in Fig. 4.7 took 7 hours to be completed due to the huge number of elements needed (over 1 million) to perform an accurate calculation.

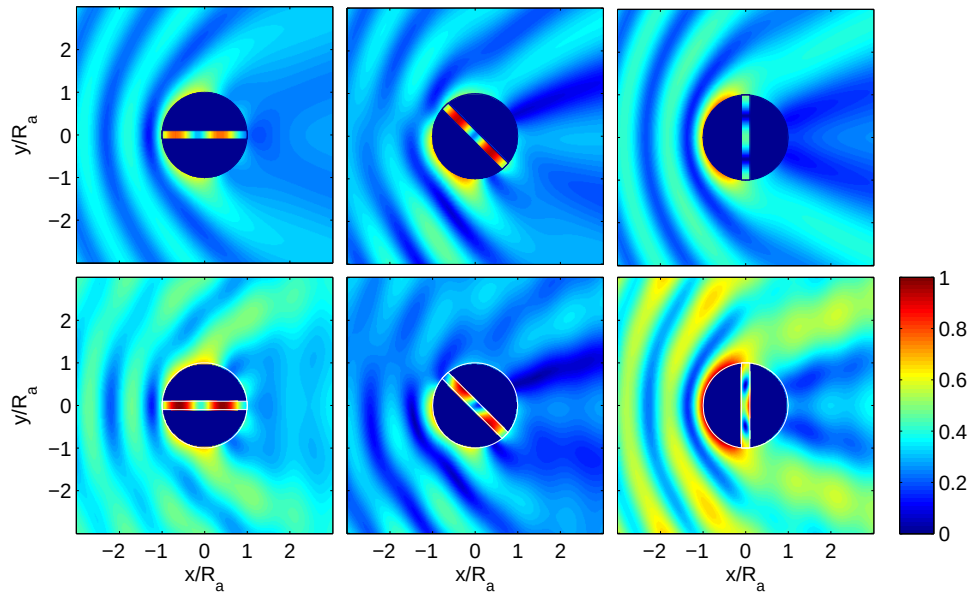

Figure 4.5: Absolute value of the displacement field produced when a plane wave ($\theta_s = 0$) with a reduced frequency $k_pR = \pi$ impinges on the system for three different beam orientations $\theta_b = [0°, -45°, -90°]$. The upper panels shows the results obtained by the analytical simulator and the lower panels show the ones obtained from the commercial finite element simulator.

Figure 4.5 shows the absolute value of the displacement obtained from the analytical simulator (left panels) and the FEM simulator (right panels) when a plane wave ($\theta_s = 0$) of non-dimensional frequency $k_pR = \pi$ impinges on the system. In a similar way, Fig. 4.6 and Fig. 4.7 show the results obtained from the analytical simulator (left panels) and the FEM simulator (right panels) for a non-dimensional frequency of $k_pR = 2\pi$ and $k_pR = 5\pi$, respectively. Notice that the scattering pattern created by the two simulator are very similar for all combinations of frequency and beam angle considered. Note particularly the case when the beam is tilted at $\theta_b = -45°$ where the discontinuities of the non-symmetric scattering pattern has been perfectly reproduced by the analytical simulator. It

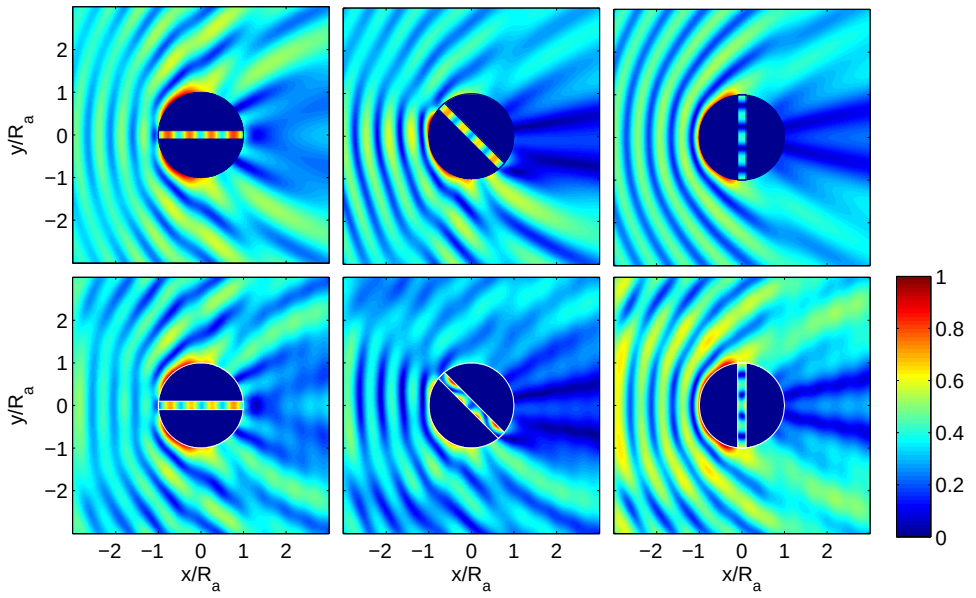

Figure 4.6: The same as for Fig. 4.5 except that the non-dimensional frequency is $k_p R = 2\pi$.

is evident from the three simulations that the flexural wavelength in the internal beam are the same in both simulations, although the FEM simulator shows some 2D wave effects within the beam that are not modeled by the 1D beam theory.

From the comparison shown in Figs. 4.5-4.7 we can conclude that our semi-analytical modeling is stable and accurate in a broad band of frequencies, at least until $k_p R = 5\pi$ which is the maximum value considered here. We note that there are clearly some restrictions to our model: (i) it has the same limitations implicit in the Kirchhoff-Love and Euler-Bernoulli theories, which have been employed in the modeling; and (ii) the present analysis only applies to objects with axial symmetry. Restriction (i) could be relaxed using higher order plate and beam theories, although the analysis and matrix algebra will be more complicated. Regarding (ii), more general shapes could be considered following the methods described in [73].

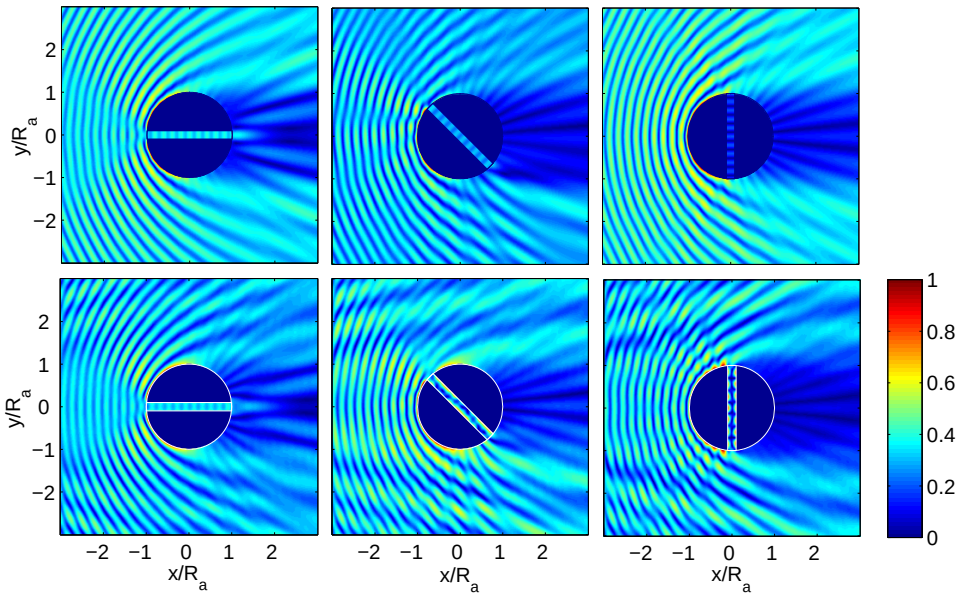

Figure 4.7: The same as for Fig. 4.5 except that the non-dimensional frequency is $k_pR = 5\pi$.

4.3.3 Scattering Cross Section

The amplitude of the scattering cross section (SCS) of a flexural waves is calculated as explained in Chapter 1

$$\sigma_{sc}(k_p, \theta) = \left| \sqrt{\frac{2}{\pi k_p}} \sum_q (-i)^q B_q^{(H)} e^{iq\theta} \right|. \tag{4.3.3}$$

Figure 4.8 shows the SCS produced when a plane wave ($\theta_s = 0$) with non-dimensional frequencies ranging from $k_pR = 0.5\pi$ to $k_pR = 5\pi$ impinges on the system. Figure 4.8a is the SCS produced by a hole in the plate. Notice that for the beam oriented at $\theta_b = 0°$ (Fig. 4.8b) the SCS around $\theta = \pi$ is lower than on Fig. 4.8a because the wave can enter the beam easily and propagate across it. On the other hand, in the position at $\theta_b = -90°$ (Fig. 4.8d), the wave encounters a hole and so it is reflected producing more back-scattering. In the case of the position at $\theta_b = -45°$

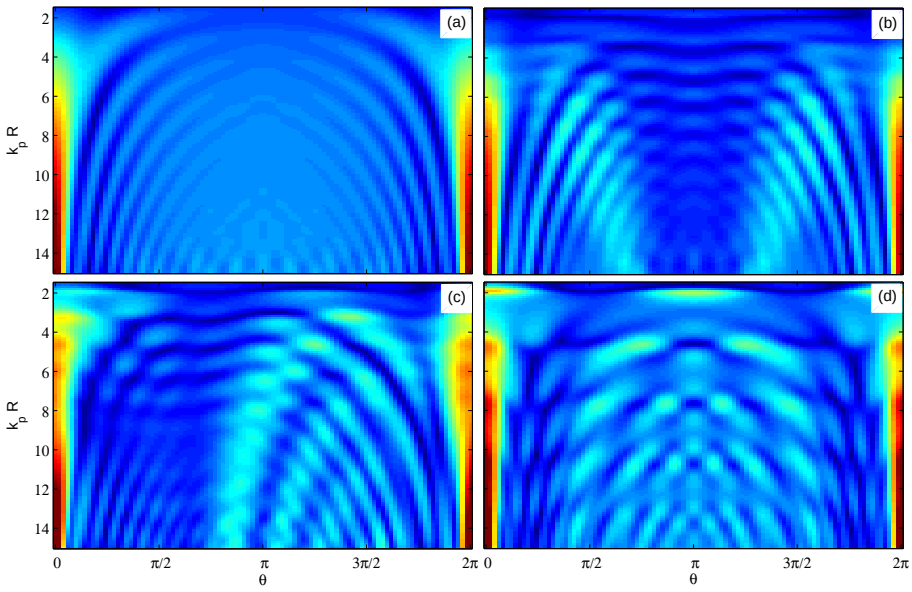

Figure 4.8: SCS produced when a plane wave ($\theta_s = 0$) with reduced frequencies ranging from $k_pR = 0.5\pi$ to $k_pR = 5\pi$ impinges a hole in a plate (a) and a hole with a crossing beam at three different orientations: $\theta_b = 0°$ (b), $\theta_b = -45°$ (c) and $\theta_b = -90°$ (d).

(Fig. 4.8c) there less back-scattering in $[0, \pi]$ than in $[\pi, 2\pi]$ because the entrance to the beam is located at $\theta_b + \pi = 3\pi/4$.

Concluding remarks

Conclusions

Throughout this manuscript new theoretical and experimental results have been reported for acoustic and flexural metamaterials. This manuscript was splited in two major parts. One covered the experimental demonstrations of two acoustic refractive devices based on sonic crystals, while the other presented three theoretical contributions showing the potential application of flexural metamaterials known as "platonic crystals".

Part I: Sound Waves

In *Chapter 2*, the focusing properties of a 2D GRIN sonic lens made of aluminum rods was presented. This lens proved to obtain good focal spot and broadband performance below the homogenization limit. Additionally, an analytical model to predict the focal spot position has been fully explained and can be replicated with other gradient index profiles. This types of devices are feasible and reliable for possible applications not only in the audible range, but also for ultrasonics and even for acoustic surface waves.

Chapter 3 reported the design, fabrication, and characterization of the acoustic analogue of the photonic black-hole. The structure consists of an outer shell that guides acoustic energy to the core center that dissipates the incoming energy by friction. Both parts were designed using metamaterials based on sonic crystals. Experimental results proved that the constructed sample acts like a broadband omnidirectional acoustic absorber. Structures like the one studied here are potentially applicable as acoustic invisibility devices based on total absorption as well as practical structures to attenuate environmental noise.

Part II: Vibrations

In *Chapter 2*, a method to locally modify the refractive index by adjusting the plate's thickness was reported. Five different refractive lenses for flexural waves in thin plates were studied. Numerical simulations, based on a multilayer scattering algorithm, confirmed the expected behavior of the five lenses analyzed and support the refractive index model

employed. It has also been demonstrated their broadband performance. This method provides the tools to obtain quasi-continuous variation of the refractive index, which obviously cannot be done with discrete lattices.

Chapter 3 showed the theoretical demonstration of an omnidirectional and broadband isolating device, used to stop the propagation of flexural waves in a given circular region of a thin plate. It is based on a circular gradient index lens that guides flexural waves to an annular region where the vibrations are dissipated via an absorptive lamina placed on top of the plate. The gradient index is also achieved by locally modifying the plate thickness. Finally, we presented numerical simulations done with a multilayer scattering algorithm, to proof its efficiency. Since the properties of the employed materials are existent in nature, the proposed device is feasible and, then, an experimental verification is expected in the near future.

In *Chapter 4*, we presented an analytical solution to obtain the T-Matrix of a thin plate with a hole traversed by a beam. The theoretical model is based on an impedance method developed for acoustic waves. We fully explained the coupling of the Kirchhoff-Love and the Euler-Bernoulli theories and the solution has been given in isolated parts that can be replaced easily. To verify the theory the principle of conservation of energy has been used. Additionally, an analytical simulator has been developed and the results have been tested against a commercial finite element simulator. Finally, the far-field behavior of the system has been presented for a wide bandwidth and different beam orientations, indicating a strong variability in the scattered field depending on the relative alignment of the beam with the incident wave.

Future Work

The present work concentrated on two research topics: acoustic and flexural metamaterials. Further, for both of them, major contributions were made there is room for improvement. Additionally, the results detailed in the previous chapters, opened new research topics. Listed below as future work.

An analytical model was used to predict the focal spot position of the gradient index lens as a function of the dimension of the lens. The equation was derived using a ray trajectory approximation, Fermat's principe and Snell's law. These are commonly theorema used in optics, but they provided good results predicting the propagation of acoustic waves. However, it could be possible to refine these results by using Chapman's law, which is more suitable for sound propagation in fluids [23].

In the case of the acoustic black hole, the energy is dissipated by friction. The sound wave is forced to propagate through a sonic crystal with a high filing fraction. To further understand this mechanism, the multiple scattering method could be improved to take into account a viscous medium by introducing the simplified version of the Navier-Stokes equation. Thus, we could not only tune the acoustic properties of the metamaterial, but also its absorption.

Both the flexural lenses and the isolation device have been theoretically studied, but not experimental demonstrated. The measuring system needed for this purpose is still under development in our group. It consists of a Doppler laser vibrometer mounted on a 2D moving platform that measures the vertical displacement of a thin plate excited by a piezoelectric. The whole system is controlled by LabView and signal processing tools are used to process the measured signal. We expect to obtain results soon.

The analytical model used to describe the behavior of a thin plate with a hole crossed by a beam is itself an achievement, but it is not the final goal. The idea behind the theoretical model is to reproduce the theoretical elastic graphene proposed by Torrent et al. [75]. In this

work Torrent used punctual resonators, so a direct implementation is not feasible. Thus, it is necessary to model and design "actual" resonators to recreate the results in an experiment. In 2014, Andreassen et al. [2], proposed an in-plate resonator which consisted of a circular hole with a centered circular island connected by two beams to the plate. Based on this design and the theory developed in this manuscript we expect to numerically and experimentally demonstrate the predictions from Torrent et al [75] who used punctual resonators.

Publications

International Journals

1. Alfonso Climente, Daniel Torrent and José Sánchez-Dehesa
   Sound focusing by gradient index sonic lenses.
   Applied Physics Letters, 97(10):104103–,pp.1-4, 2010.

2. Alfonso Climente, Daniel Torrent and José Sánchez-Dehesa
   Omnidirectional broadband acoustic absorber based on metamaterials.
   Applied Physics Letters, 100(14):144103–,pp.1-4, 2012.

3. Alfonso Climente, Daniel Torrent and José Sánchez-Dehesa
   Gradient index lenses for flexural waves based on thickness variations.
   Applied Physics Letters, 105(6):064101–,pp.1-4, 2014.

4. Alfonso Climente, Daniel Torrent and José Sánchez-Dehesa
   Omnidirectional broadband insulating device for flexural waves in thin plates.
   Journal of Applied Physics, 114(21):214903–,pp.1-8, 2013.

5. Alfonso Climente, Andrew N. Norris and José Sánchez-Dehesa
   Scattering of flexural waves from a hole in a thin plate with an internal beam.
   The Journal of the Acoustical Society of America, 137(1),pp.293-302, 2015.

International Meetings and Conferences

1. Alfonso Climente, Daniel Torrent and José Sánchez-Dehesa
   Noise reduction by perfect absorbers based on acoustic metamaterials.
   ASME 2010 International Mechanical Engineering Congress and Exposition, IMECE 2010, Denver (USA), 2010.

2. Alfonso Climente, Daniel Torrent and José Sánchez-Dehesa
   Omnidirectional broadband concentrator for flexural waves
   XXXIV Bienal de la Real Sociedad Española de Física, 34th BIENAL, Valencia (Spain), 2013

3. Alfonso Climente, Daniel Torrent and José Sánchez-Dehesa
   Omnidirectional broadband concentrator for flexural waves
   7th International Congress on Advanced Electromagnetic Materials in Microwaves and Optics, Metamaterials 2013, Burdeos (France), 2013

Appendix

Appendix A

Bessel functions

A.1 Bessel's differential equation

The Helmholtz equation in polar coordinates (r, θ) is

$$\left(\frac{\partial^2}{\partial r^2} + \frac{1}{r}\frac{\partial}{\partial r} + \frac{1}{r^2}\frac{\partial^2}{\partial \theta^2} + k^2\right)\Psi(r,\theta) = 0, \tag{A.1.1}$$

and has the solution

$$\Psi(r,\theta) = \sum_q \Upsilon_q(kr)e^{iq\theta}, \tag{A.1.2}$$

where q is an integer, k is the wave number and the function $\Upsilon_q(kr)$ has to satisfy the Bessel differential equation

$$r^2\frac{d^2\Upsilon}{dr^2} + r\frac{d\Upsilon}{dr} + ((kr)^2 - q^2)\Upsilon = 0, \tag{A.1.3}$$

being $z = kr$ a complex number. Because this is a second-order differential equation, there must be two linearly independent solutions. The two different families of functions are called the Bessel functions of the first and second kind.

The Bessel functions of the first kind, denoted as $J_q(z)$, are finite at the origin $(z = 0)$ and oscillate towards infinity with a decay proportion-

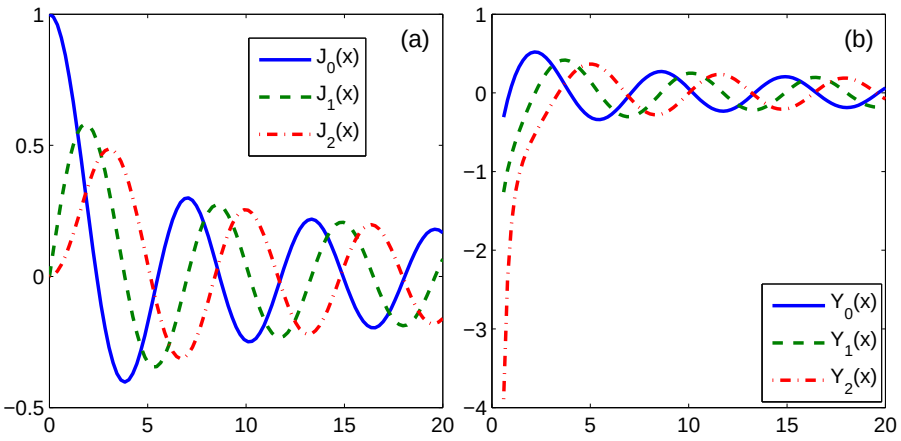

Figure A.1: Bessel functions of (a) the first and (b) second kind.

ally of $1/\sqrt{z}$, see Fig. A.1(a). The function can be defined by its Taylor series expansion as

$$J_q(z) = \sum_n \frac{(-1)^n}{n!(n+q)!}\left(\frac{z}{2}\right)^{q+2n} \qquad q > 0. \tag{A.1.4}$$

The Bessel functions of the second kind, denoted as $Y_q(z)$, have a singularity around $(z = 0)$ that tends towards negative infinite values. For increasing values of $|z|$, the functions oscillate towards infinity with a decay, see Fig. A.1(b). Being α a real number, then the functions are defined as

$$Y_q(z) = \lim_{\alpha \to q} \frac{J_\alpha(z)\cos(\alpha\pi) - J_{-\alpha}(z)}{\sin(\alpha z)}. \tag{A.1.5}$$

There exist a third solution to Bessel's differential equation, which is a linear combination of the two previous ones. They are know as the Hankel functions $H_q^{(1)}(z)$ and $H_q^{(2)}(z)$, defined as

$$H_q^{(1)}(z) = J_q(z) + iY_q(z), \tag{A.1.6a}$$
$$H_q^{(s)}(z) = J_q(z) - iY_q(z), \tag{A.1.6b}$$

where i is the imaginary unit. The importance of Hankel functions lies more in theoretical development rather than in application. These forms of linear combination satisfy numerous simple-looking properties, like asymptotic behavior or integral representations. For time harmonic solution of the form $e^{-i\omega t}$, they are useful to express outgoing ($H^{(1)}$) and incoming ($H^{(2)}$) propagating cylindrical waves (or vice versa, for solutions of the form $e^{i\omega t}$).

A.1.1 Properties

For integer values of q, the solution of the Bessel's differential equation are entire and derivable functions. To simplify the notation, lets introduce the following relationship

$$\frac{\partial \Upsilon_q(kr)}{\partial r} \equiv k\Upsilon'_q(kr), \tag{A.1.7}$$

where $\Upsilon = J, Y, H$. Then the solutions of the Bessel's differential equations satisfy the following relations and properties

$$\Upsilon_{-q}(kr) = (-1)^q \Upsilon_q(kr), \tag{A.1.8a}$$

$$\frac{2q}{kr}\Upsilon_q(kr) = \Upsilon_{q-1}(kr) + \Upsilon_{q+1}(kr), \tag{A.1.8b}$$

$$2k\Upsilon'_q(kr) = \Upsilon_{q-1}(kr) - \Upsilon_{q+1}(kr). \tag{A.1.8c}$$

The Wronskian identities are

$$k\left[J_q(kr)Y'_q(kr) - J'_q(kr)Y_q(kr)\right] = \frac{2k}{\pi r}, \tag{A.1.9a}$$

$$k\left[J_q(kr)H'_q(kr) - J'_q(kr)H_q(kr)\right] = \frac{2ik}{\pi r}. \tag{A.1.9b}$$

A.1.2 Asymptotic Forms

When $x \to 1$, being x a real value,

$$J_q(x) \approx \sqrt{\frac{2}{\pi x}} \cos\left(x - \frac{q\pi}{2} - \frac{\pi}{4}\right) \tag{A.1.10a}$$

$$Y_q(x) \approx \sqrt{\frac{2}{\pi x}} \sin\left(x - \frac{q\pi}{2} - \frac{\pi}{4}\right) \tag{A.1.10b}$$

$$H_q(x) \approx \sqrt{\frac{2}{\pi x}} (-i)^q e^{-i\pi/4} e^{ix} \tag{A.1.10c}$$

A.2 Modified Bessel's differential equation

The Helmholtz modified equation in polar coordinates (r, θ) is

$$\left(\frac{\partial^2}{\partial r^2} + \frac{1}{r}\frac{\partial}{\partial r} + \frac{1}{r^2}\frac{\partial^2}{\partial \theta^2} - k^2\right) \Psi(r, \theta) = 0, \tag{A.2.1}$$

and has the solution

$$\Psi(r, \theta) = \sum_q \Upsilon_q(kr) e^{iq\theta}, \tag{A.2.2}$$

where q is an integer, k is the wave number and the function $\Upsilon_q(kr)$ has to satisfy the modified Bessel differential equation

$$r^2 \frac{d^2\Upsilon}{dr^2} + r\frac{d\Upsilon}{dr} - ((kr)^2 + q^2)\Upsilon = 0. \tag{A.2.3}$$

being $z = kr$ a complex number. This differential equation appears during the resolution of the equation of motion of thin plates. As in the case of Bessel's differential equation, this is also a second-order differential equation, and therefore there must be two linearly independent solutions. The two different families of functions are called the modified Bessel functions of the first and second kind.

The modified Bessel functions of the first kind, denoted as $I_q(z)$, grow exponentially with increasing argument $|z|$, see Fig. A.2(a). They are useful to describe evanescent waves coming towards the origin. The function is defined in terms of Bessel function of the first kind as

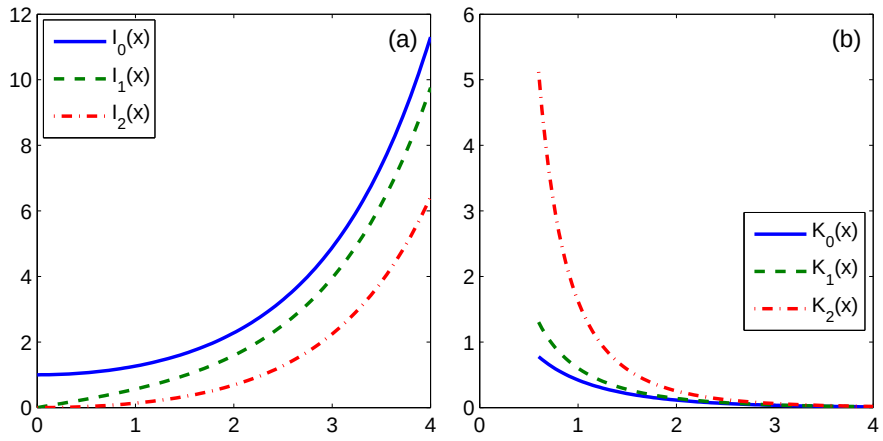

Figure A.2: Modified Bessel functions of (a) the first and (b) second kind.

$$I_q(z) = (-i)^q J_q(iz). \tag{A.2.4}$$

The modified Bessel functions of the second kind, denoted as $K_q(z)$, decay exponentially with increasing argument $|z|$, see Fig. A.1(b). They are use to describe evanescent scattering waves. Being α a real number, then the functions are defined as

$$K_q(z) = \lim_{\alpha \to q} \frac{\pi}{2} \frac{I_{-\alpha}(z) - I_\alpha(z)}{\sin(\alpha\pi)}. \tag{A.2.5}$$

A.2.1 Properties

For integer values of q, the solution of the modified Bessel's differential equation are entire and derivable functions. To simplify the notation, lets introduce the following relationship

$$\frac{\partial \Upsilon_q(kr)}{\partial r} \equiv k\Upsilon'_q(kr), \tag{A.2.6}$$

where $\Upsilon = I, K$. Then the solutions of the modified Bessel's differential equations satisfy the following relations and properties

$$\Upsilon_{-q}(kr) = \Upsilon_q(kr), \tag{A.2.7}$$

for $\Upsilon = I, K$ and

$$\frac{2q}{kr}\Upsilon_q(kr) = \Upsilon_{q-1}(kr) - \Upsilon_{q+1}(kr), \tag{A.2.8a}$$

$$2k\Upsilon'_q(kr) = \Upsilon_{q-1}(kr) + \Upsilon_{q+1}(kr), \tag{A.2.8b}$$

for $\Upsilon = I, (-1)^q K$. Finally, the Wronskian identity is

$$k\left[I_q(kr)K'_q(kr) - I'_q(kr)K_q(kr)\right] = -\frac{k}{r}. \tag{A.2.9}$$

A.2.2 Asymptotic Forms

When $x \to 1$, being x a real value,

$$I_q(x) \approx \frac{e^x}{\sqrt{2\pi x}}\left(1 + \sum_{n=1}(-1)^n \frac{\prod_{i_1}^n (4q^2 - (2i-1)^2)}{n!(8x)^n}\right), \tag{A.2.10a}$$

$$K_q(x) \approx \frac{\pi e^{-x}}{\sqrt{2x}}\left(1 + \sum_{n=1} \frac{\prod_{i_1}^n (4q^2 - (2i-1)^2)}{n!(8x)^n}\right) \to 0. \tag{A.2.10b}$$

A.3 Graf's addition theorem

Graf's addition theorem for Bessel functions is given in Abramowitz and Stegun Handbook of Mathematical Functions [52]. It is a special case of Neumann's addition theorem. Let's consider the vectors and angles shown in Fig. A.3, then the theorem can be expressed in the following form, for the solutions of Bessel's differential equations,

$$\Upsilon_r(w)e^{ir\theta_{wu}} = \sum_s \Upsilon_{r+s}(u)J_s(v)e^{is\theta_{uv}} \qquad v < u, \tag{A.3.1}$$

where $\Upsilon = J, Y, H$; or, for the solutions of the modified Bessel's differential equations,

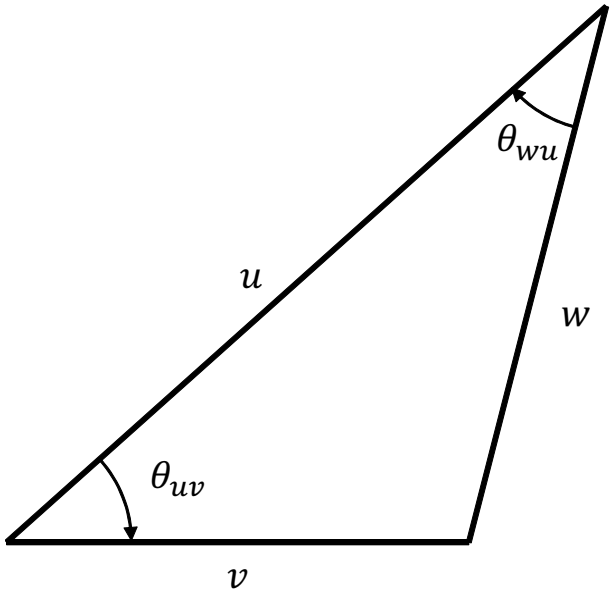

Figure A.3: Variables of Graf's addition theorem.

$$\Upsilon_r(w)e^{ir\theta_{wu}} = \sum_s \Upsilon_{r+s}(u)I_s(v)e^{is\theta_{uv}} \qquad v < u, \tag{A.3.2}$$

where $\Upsilon = I, K$. Notice that the condition $v < u$ gives two possible ways of applying it.

Throught out thiw work, Graf's addition theorem has been applied to change the reference frame in three different situations:

1. Expressing an incoming wave or point source in a different frame.

2. Expressing the scattering field produced by the β-cylinder as a wave centered into the α-cylinder.

3. Expressing the total scattering field of a cluster as an effective field scattered by one cylinder.

Here, to illustrate the process, the second case used during the demonstration of the multiple scattering method is presented. A similar ap-

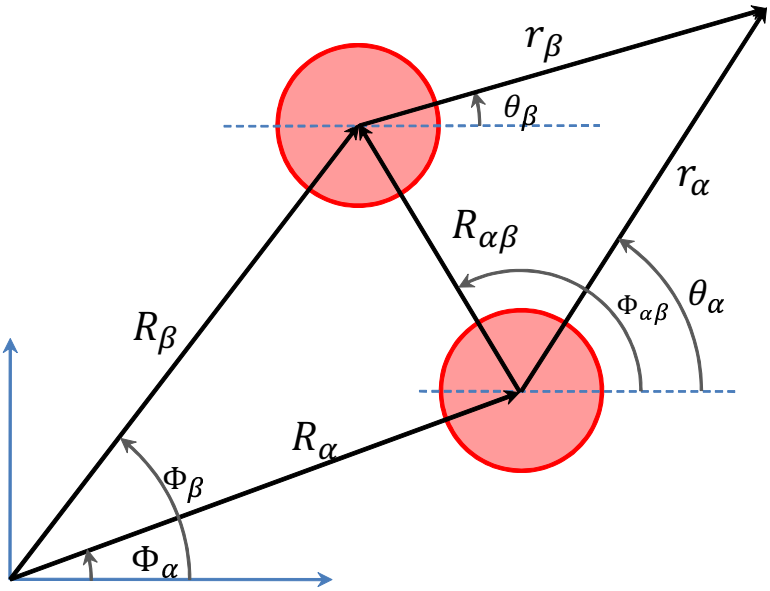

Figure A.4: Example of application of Graf's addition theorem.

proach is used to solve the other cases. The objective is to express the quantity [see Eq. (1.3.3)]

$$H_r(k_b r_\beta)e^{ir\theta_\beta} \tag{A.3.3}$$

in the reference frame of the α-cylinder. Let's consider the system described in Fig. A.4. We want to express $\mathbf{r}_\beta$ in the α frame, so $w = r_\beta$ and $v = r_\alpha$.Then the angles are

$$\begin{aligned} w &= r_\beta, & \theta_{wu} &= \Phi_{\beta\alpha} - \theta_\beta, \\ v &= r_\alpha, & \theta_{uv} &= (2\pi - \Phi_{\alpha\beta}) + \theta_\alpha, \\ u &= R_{\alpha\beta}, & \Phi_{\beta\alpha} &= \Phi_{\alpha\beta} - \pi. \end{aligned}$$

Then, Eq. (A.3.1) is rewritten as

$$H_r(k_b r_\beta)e^{ir\Phi_{\alpha\beta}}e^{-ir\pi}e^{-ir\theta_\beta} = \sum_s H_{r+s}(k_b R_{\alpha\beta})J_s(k_b r_\alpha)e^{is2\pi}e^{-is\Phi_{\alpha\beta}}e^{is\theta_\alpha}. \tag{A.3.4}$$

Simplifying and reorganizing terms

$$H_r(k_b r_\beta)(-1)^{-r}e^{-ir\theta_\beta} = \sum_s \left[H_{r+s}(k_b R_{\alpha\beta})e^{i(-s-r)\Phi_{\alpha\beta}}\right] J_s(k_b r_\alpha)e^{is\theta_\alpha}, \tag{A.3.5}$$

then, by changing $r \to -r$,

$$H_{-r}(k_b r_\beta)(-1)^{r}e^{ir\theta_\beta} = \sum_s \left[H_{s-r}(k_b R_{\alpha\beta})e^{i(r-s)\Phi_{\alpha\beta}}\right] J_s(k_b r_\alpha)e^{is\theta_\alpha}, \tag{A.3.6}$$

and by applying the Bessel property of Eq. (A.1.8a) we obtain the final form

$$H_r(k_b r_\beta)e^{ir\theta_\beta} = \sum_s \left[H_{s-r}(k_b R_{\alpha\beta})e^{i(r-s)\Phi_{\alpha\beta}}\right] J_s(k_b r_\alpha)e^{is\theta_\alpha}. \tag{A.3.7}$$

Appendix B

Four microphones method

To obtain the complex acoustic properties of materials, several methods have been proposed in the literature. Salissou and Panneton made a full review on this topic in [66]. The method that is here described is the four microphone method developed for impedance tubes by Song and Bolton [69].

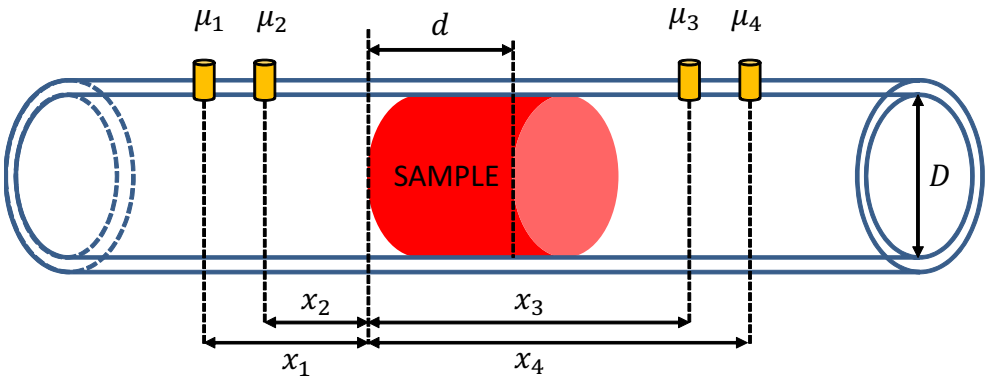

Figure B.1: Scheme of the impedance tube

Lets consider the impedance tube shown in Fig. B.1. The sample of length d is place between four microphones located at the points x_i. The first cut-off frequency of the tube established the range that this method is valid for. It is calculated as

$$f_c = \eta \frac{c_b}{\pi D}, \tag{B.0.1}$$

where η is the first root of $J_1'(\eta) = 0$, D is the inner diameter of the tube and c_b is the speed of the fluid inside the tube. Then, in case of mono mode propagation, the acoustic pressure wave $P(x)$ inside the tube can be expressed as

$$P(x) = \begin{cases} Ae^{jk_b x} + Be^{-jk_b x} & \text{for} \quad x \leq 0 \\ Ce^{jk_b x} + De^{-jk_b x} & \text{for} \quad x \geq d \end{cases}, \tag{B.0.2}$$

where $k_b = \omega / c_b$ is the wavenumber and A, B, C, D are constants to be determined using the measurements done with the microphones in the points x_i.

Once the pressure wave is determined, the complex wavenumber and the acoustic impedance of the sample can be obtained from

$$k = \frac{1}{d} \cos^{-1}(T_{11}), \tag{B.0.3}$$

$$Z = \sqrt{\frac{T_{12}}{T_{21}}}, \tag{B.0.4}$$

where

$$T_{11} = T_{22} = \frac{P(d)\mathbf{v}(d) + P(0)\mathbf{v}(0)}{P(0)\mathbf{v}(d) + P(d)\mathbf{v}(0)}, \tag{B.0.5}$$

$$T_{12} = \frac{P(0)^2 - P(d)^2}{P(0)\mathbf{v}(d) + P(d)\mathbf{v}(0)}, \tag{B.0.6}$$

$$T_{21} = \frac{\mathbf{v}(0)^2 - \mathbf{v}(d)^2}{P(0)\mathbf{v}(d) + P(d)\mathbf{v}(0)}, \tag{B.0.7}$$

where $\mathbf{v}$ is the particle velocity calculated from the pressure using Eq. (1.1.5). Notice that the wavenumber k in Eq. (B.0.3) is calculated with the inverse-cosine function. As it is known the cosine function is non-bijective, because it is not cyclic. Therefore the resulting wavenumber is not linear and continuous. To solve this issue the procedure followed by Baccigalupi [4] has been applied.

Appendix C

Delta Parameter

Figure C.1 and Table C.0.1 show the behavior of the Delta Parameter (Δ) in function of the filling fraction (ff), for the case of rigid cylinders arranged in any type of lattice. Although $\Delta(ff) \approx 1$, it is important to remark that at high filling fractions, not considering the parameter affects the effective parameters greatly.

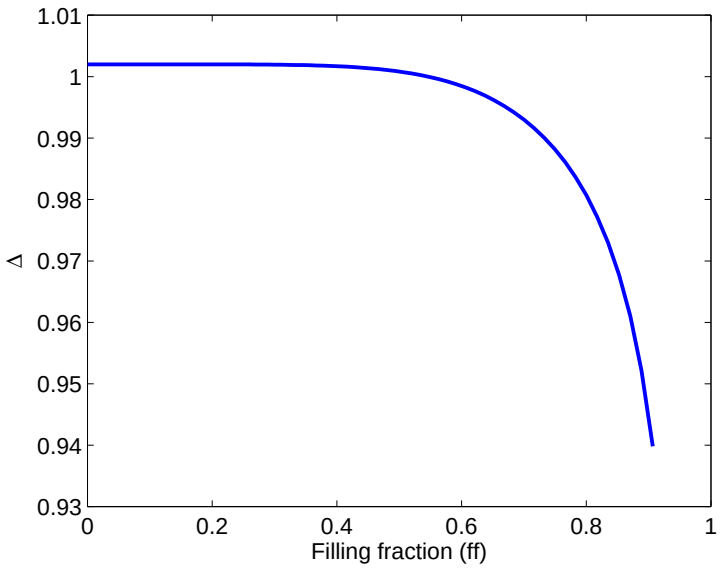

Figure C.1: Delta Parameter (Δ) in function of the filling fraction (ff).

Table C.0.1: Delta Parameter Δ as a function of the filling fraction (ff).

ff	Δ	ff	Δ	ff	Δ	ff	Δ
0.01	1.0020	0.24	1.0020	0.47	1.0012	0.70	0.9930
0.02	1.0020	0.25	1.0020	0.48	1.0011	0.71	0.9922
0.03	1.0020	0.26	1.0020	0.49	1.0010	0.72	0.9913
0.04	1.0020	0.27	1.0020	0.50	1.0008	0.73	0.9903
0.05	1.0020	0.28	1.0020	0.51	1.0007	0.74	0.9893
0.06	1.0020	0.29	1.0020	0.52	1.0005	0.75	0.9881
0.07	1.0020	0.30	1.0019	0.53	1.0003	0.76	0.9869
0.08	1.0020	0.31	1.0019	0.54	1.0001	0.77	0.9856
0.09	1.0020	0.32	1.0019	0.55	0.9999	0.78	0.9841
0.10	1.0020	0.33	1.0019	0.56	0.9997	0.79	0.9825
0.11	1.0020	0.34	1.0019	0.57	0.9994	0.80	0.9807
0.12	1.0020	0.35	1.0019	0.58	0.9991	0.81	0.9788
0.13	1.0020	0.36	1.0018	0.59	0.9988	0.82	0.9766
0.14	1.0020	0.37	1.0018	0.60	0.9985	0.83	0.9743
0.15	1.0020	0.38	1.0018	0.61	0.9981	0.84	0.9716
0.16	1.0020	0.39	1.0017	0.62	0.9977	0.85	0.9686
0.17	1.0020	0.40	1.0017	0.63	0.9973	0.86	0.9652
0.18	1.0020	0.41	1.0016	0.64	0.9968	0.87	0.9613
0.19	1.0020	0.42	1.0016	0.65	0.9963	0.88	0.9568
0.20	1.0020	0.43	1.0015	0.66	0.9957	0.89	0.9514
0.21	1.0020	0.44	1.0015	0.67	0.9951	0.90	0.9449
0.22	1.0020	0.45	1.0014	0.68	0.9945		
0.23	1.0020	0.46	1.0013	0.69	0.9938		

Bibliography

[1] M. Abramowitz and I. Stegun. *Handbook of Mathematical Functions*. Dover Publications, 1965.

[2] E. Andreassen, K. Manktelow, and M. Ruzzene. Directional bending wave propagation in periodically perforated plates. *Journal of Sound and Vibration*, 335:187 – 203, 2015.

[3] O. Atak. *Phd Thesis: Wave based modeling method for acoustic inclusion and multiple scattering problems in the mid-frequency range*. ku Leuven Unv., 2014.

[4] A. Baccigalupi. Adc testing methods. *Measurement*, 26(3):199–205, 1999.

[5] M. Badreddine Assouar, M. Senesi, M. Oudich, M. Ruzzene, and Z. Hou. Broadband plate-type acoustic metamaterial for low-frequency sound attenuation. *Applied Physics Letters*, 101(17):173505, 2012.

[6] D. Bies and C. Hansen. *Engineering Noise Control: Theory and Practice*. Taylor & Francis, 2009.

[7] Y. Bobrovnitskii. Impedance theory of sound scattering: General relations. *Acoustical Physics*, 52(5):513–517, 2006.

[8] M. Born and E. Wolf. *Principles of optics: electromagnetic theory of propagation, interference and diffraction of light*. Pergamon Press, 1970.

[9] S. Bramhavar, C. Prada, A. A. Maznev, A. G. Every, T. B. Norris, and T. W. Murray. Negative refraction and focusing of elastic lamb waves at an interface. *Physical Review B*, 83(1):014106, 2011.

[10] F. Casadei, M. Ruzzene, L. Dozio, and K. A. Cunefare. Broadband vibration control through periodic arrays of resonant shunts: experimental investigation on plates. *Smart materials and structures*, 19(1):015002, 2010.

[11] F. Cervera, L. Sanchis, J. Sanchez-Perez, R. Martinez-Sala, C. Rubio, F. Meseguer, C. López, D. Caballero, and J. Sánchez-Dehesa. Refractive acoustic devices for airborne sound. *Physical Review Letters*, 88(2):023902, 2001.

[12] Z. Chang and G. Hu. Elastic wave omnidirectional absorbers designed by transformation method. *Applied Physics Letters*, 101(5):054102, 2012.

[13] Q. Cheng, T. J. Cui, W. X. Jiang, and B. G. Cai. An omnidirectional electromagnetic absorber made of metamaterials. *New Journal of Physics*, 12(6):063006, June 2010.

[14] C. C. Claeys, P. Sas, and W. Desmet. On the acoustic radiation efficiency of local resonance based stop band materials. *Journal of Sound and Vibration*, 333(14):3203–3213, 2014.

[15] C. C. Claeys, K. Vergote, P. Sas, and W. Desmet. On the potential of tuned resonators to obtain low-frequency vibrational stop bands in periodic panels. *Journal of Sound and Vibration*, 332(6):1418–1436, 2013.

[16] J. Eaton. On spherically symmetric lenses. *Antennas and Propagation, Transactions of the IRE Professional Group on*, 4(1):66–71, 1952.

[17] N. Fang, D. Xi, J. Xu, M. Ambati, W. Srituravanich, C. Sun, and X. Zhang. Ultrasonic metamaterials with negative modulus. *Nature materials*, 5(6):452–456, 2006.

[18] M. Farhat, S. Guenneau, and S. Enoch. High directivity and confinement of flexural waves through ultra-refraction in thin perforated plates. *Europhysics Letters*, 91(5):54003, sep 2010.

[19] M. Farhat, S. Guenneau, S. Enoch, A. B. Movchan, and G. G. Petursson. Focusing bending waves via negative refraction in perforated thin plates. *Applied Physics Letters*, 96(8):081909, 2010.

[20] P. Fromme, P. D. Wilcox, M. J. Lowe, and P. Cawley. On the development and testing of a guided ultrasonic wave array for structural integrity monitoring. *Ultrasonics, Ferroelectrics and Frequency Control, IEEE Transactions on*, 53(4):777–785, 2006.

[21] D. A. Genov, S. Zhang, and X. Zhang. Mimicking celestial mechanics in metamaterials. *Nature Physics*, 5(9):687–692, 2009.

[22] V. Georgiev, J. Cuenca, F. Gautier, L. Simon, and V. V. Krylov. Damping of structural vibrations in beams and elliptical plates using the acoustic black hole effect. *Journal of Sound and Vibration*, 330(11):2497–2508, 2011.

[23] O. A. Godin. Wave refraction at an interface: Snells law versus chapmans law. *The Journal of the Acoustical Society of America*, 125(4):EL117–EL122, 2009.

[24] K. F. Graff. *Wave Motion in elastic solids, 2nd Ed.* Dover, 1991.

[25] B. C. Gupta and Z. Ye. Theoretical analysis of the focusing of acoustic waves by two-dimensional sonic crystals. *Physical Review E*, 67(3):036603, 2003.

[26] J.-C. Hsu and T.-T. Wu. Efficient formulation for band-structure calculations of two-dimensional phononic-crystal plates. *Physical Review B*, 74(14):144303, 2006.

[27] C.-Y. Huang, J.-H. Sun, and T.-T. Wu. A two-port zno/silicon lamb wave resonator using phononic crystals. *Applied Physics Letters*, 97(3):–, 2010.

[28] M. I. Hussein, M. J. Leamy, and M. Ruzzene. Dynamics of phononic materials and structures: Historical origins, recent progress, and future outlook. *American Society of Mechanical Engineers*, 66(4):040802+, 2014.

[29] A. Khelif, Y. Achaoui, S. Benchabane, V. Laude, and B. Aoubiza. Locally resonant surface acoustic wave band gaps in a two-dimensional phononic crystal of pillars on a surface. *Physical Review B*, 81:214303, Jun 2010.

[30] A. V. Kildishev, L. J. Prokopeva, O. V. Shtyrina, M. P. Fedoruk, and E. E. Narimanov. Optical black hole: Design and performance. In *2010 Conference on Laser and Electro-Optics (CLEO) and quantum electronics and laser science conference (QELS)*, 2010.

[31] G. Krishnappa. Cross-spectral method of measuring acoustic intensity by correcting phase and gain mismatch errors by microphone calibration. *The Journal of the Acoustical Society of America*, 69(1):307–310, 1981.

[32] A. Krokhin, J. Arriaga, and L. Gumen. Speed of sound in periodic elastic composites. *Physical Review Letters*, 91(26):264302, Dec 2003.

[33] V. V. Krylov. Acoustic black holes and their applications for vibration damping and sound absorption. In *Proceedings of the International Conference on Noise and Vibration Engineering (ISMA 2012)*, pages 933–944. Sas, P., Moens, D. and Jonckheer, S. (eds.)., Sept 2012.

[34] V. V. Krylov and F. Tilman. Acoustic black holes for flexural waves as effective vibration dampers. *Journal of Sound and Vibration*, 274(3):605–619, 2004.

[35] V. V. Krylov and R. Winward. Experimental investigation of the acoustic black hole effect for flexural waves in tapered plates. *Journal of Sound and Vibration*, 300(1):43–49, 2007.

[36] W.-M. Lee and J.-T. Chen. Scattering of flexural wave in a thin plate with multiple circular holes by using the multipole trefftz method. *International Journal of Solids and Structures*, 47(9):1118 – 1129, 2010.

[37] A. W. Leissa. *Vibration of Plates, 2nd Ed.* NASA, 1969.

[38] R.-Q. Li, X.-F. Zhu, B. Liang, Y. Li, X.-Y. Zou, and J.-C. Cheng. A broadband acoustic omnidirectional absorber comprising positive-index materials. *Applied Physics Letters*, 99(19):193507, Nov 2011.

[39] S.-C. S. Lin, T. J. Huang, J.-H. Sun, and T.-T. Wu. Gradient-index phononic crystals. *Physical Review B*, 79(9):094302, Mar 2009.

[40] S. Liu, L. Li, Z. Lin, H. Y. Chen, J. Zi, and C. T. Chan. Graded index photonic hole: Analytical and rigorous full wave solution. *Physical Review B*, 82(5):054204, Aug 2010.

[41] X. Liu, G. Hu, G. Huang, and C. Sun. An elastic metamaterial with simultaneously negative mass density and bulk modulus. *Applied Physics Letters*, 98(25):251907, 2011.

[42] Z. Liu, X. Zhang, Y. Mao, Y. Zhu, Z. Yang, C. Chan, and P. Sheng. Locally resonant sonic materials. *Science*, 289(5485):1734–1736, 2000.

[43] W. Lu, J. Jin, Z. Lin, and H. Chen. A simple design of an artificial electromagnetic black hole. *Journal of Applied Physics*, 108(6):064517, Sept 2010.

[44] R. K. Luneburg. *Mathematical theory of optics*. Univ of California Press, 1964.

[45] B. Mace. Discussion: "dynamics of phononic materials and structures: Historical origins, recent progress and future outlook," (hussein, m.i., leamy, m.j. and ruzzene, m.). *American Society of Mechanical Engineers*, 66:045502+, may 2014.

[46] T. P. Martin, M. Nicholas, G. Orris, L. Cai, D. Torrent, and J. Sánchez-Dehesa. Sonic gradient index lens for aqueous applications. *Applied Physics Letters*, 97(10):113503, Sep 2010.

[47] R. McPhedran, A. Movchan, and N. Movchan. Platonic crystals: Bloch bands, neutrality and defects. *Mechanics of Materials*, 41(4):356–363, 2009.

[48] J. Mei, Z. Liu, W. Wen, and P. Sheng. Effective mass density of fluid-solid composites. *Physical Review Letters*, 96(2):024301, 2006.

[49] E. Meyer. *Physical and Applied Acoustics*. Academic Press, 1967.

[50] A. Movchan, N. Movchan, and R. McPhedran. Blochfloquet bending waves in perforated thin plates. *Proceedings of the Royal Society A: Mathematical, Physical and Engineering Science*, 463(2086):2505–2518, 2007.

[51] C. J. Naify, T. P. Martin, C. N. Layman, M. Nicholas, A. L. Thangawng, D. C. Calvo, and G. J. Orris. Underwater acoustic omnidirectional absorber. *Applied Physics Letters*, 104(7):–, 2014.

[52] E. Narimanov and A. Kildishev. Optical black hole: Broadband omnidirectional light absorber. *Applied Physics Letters*, 95(4):041106, July 2009.

[53] A. Norris and A. Shuvalov. Elastic cloaking theory. *Wave Motion*, 48(6):525 – 538, 2011. Special Issue on Cloaking of Wave Motion.

[54] A. Norris and C. Vemula. Scattering of flexural waves on thin plates. *Journal of Sound and Vibration*, 181(1):115 – 125, 1995.

[55] D. O'Boy, V. V. Krylov, and V. Kralovic. Damping of flexural vibrations in rectangular plates using the acoustic black hole effect. *Journal of Sound and Vibration*, 329(22):4672–4688, 2010.

[56] H. Odabasi, F. L. Teixeira, and W. C. Chew. Impedance-matched absorbers and optical pseudo black holes. *Journal of the Optical Society of America B*, 28(5):1317–1323, May 2011.

[57] M. Oudich, Y. Li, B. M. Assouar, and Z. Hou. A sonic band gap based on the locally resonant phononic plates with stubs. *New Journal of Physics*, 12(8):083049, 2010.

[58] M. Oudich, M. Senesi, M. B. Assouar, M. Ruzenne, J.-H. Sun, B. Vincent, Z. Hou, and T.-T. Wu. Experimental evidence of locally resonant sonic band gap in two-dimensional phononic stubbed plates. *Physical Review B*, 84:165136, Oct 2011.

[59] W. Parnell and P. Martin. Multiple scattering of flexural waves by random configurations of inclusions in thin plates. *Wave Motion*, 48(2):161 – 175, 2011.

[60] J. Pendry, A. Holden, W. Stewart, and I. Youngs. Extremely low frequency plasmons in metallic mesostructures. *Physical review letters*, 76(25):4773, 1996.

[61] S. Peng, Z. He, H. Jia, A. Zhang, C. Qiu, M. Ke, and Z. Liu. Acoustic far-field focusing effect for two-dimensional graded negative refractive-index sonic crystals. *Applied Physics Letters*, 96(26):263502, 2010.

[62] Y. Pennec, B. Djafari-Rouhani, H. Larabi, J. O. Vasseur, and A. C. Hladky-Hennion. Low-frequency gaps in a phononic crystal constituted of cylindrical dots deposited on a thin homogeneous plate. *Physical Review B*, 78:104105, Sep 2008.

[63] J. Pierre, O. Boyko, L. Belliard, J. Vasseur, and B. Bonello. Negative refraction of zero order flexural lamb waves through a two-dimensional phononic crystal. *Applied Physics Letters*, 97(12):121919–121919, 2010.

[64] D. Ross, E. E. Ungar, and E. Kerwin. Damping of plate flexural vibrations by means of viscoelastic laminae. *Structural damping*, 3:44–87, 1959.

[65] R. Sainidou, B. Djafari-Rouhani, Y. Pennec, and J. O. Vasseur. Locally resonant phononic crystals made of hollow spheres or cylinders. *Physical Review B*, 73:024302, Jan 2006.

[66] Y. Salissou and R. Panneton. Wideband characterization of the complex wave number and characteristic impedance of sound absorbers. *The Journal of the Acoustical Society of America*, 128(5):2868–2876, 2010.

[67] J. Sánchez-Pérez, D. Caballero, R. Martinez-Sala, C. Rubio, J. Sánchez-Dehesa, F. Meseguer, J. Llinares, and F. Gálvez. Sound attenuation by a two-dimensional array of rigid cylinders. *Physical Review Letters*, 80(24):5325, 1998.

[68] L. Sanchis, A. Håkansson, F. Cervera, and J. Sánchez-Dehesa. Acoustic interferometers based on two-dimensional arrays of rigid cylinders in air. *Physical Review B*, 67(3):035422, 2003.

[69] B. H. Song and J. S. Bolton. A transfer-matrix approach for estimating the characteristic impedance and wave numbers of limp and rigid porous materials. *The Journal of the Acoustical Society of America*, 107(3):1131–1152, 2000.

[70] V. Squire and T. Dixon. Scattering of flexural waves from a coated cylindrical anomaly in a thin plate. *Journal of Sound and Vibration*, 236(2):367–373, 2000.

[71] N. Stenger, M. Wilhelm, and M. Wegener. Experiments on elastic cloaking in thin plates. *Physical Review Letters*, 108(1):014301, jan 2012.

[72] S. Timoshenko, S. Woinowsky-Krieger, and K. (Firm). *Theory of plates and shells*. New York : McGraw-Hill, 2nd ed edition, 1959. Includes bibliographical footnote references and indexes.

[73] A. S. Titovich and A. N. Norris. Tunable cylindrical shell as an element in acoustic metamaterial. *The Journal of the Acoustical Society of America*, 136(4):1601–1609, 2014.

[74] D. Torrent, A. Håkansson, F. Cervera, and J. Sánchez-Dehesa. Homogenization of two-dimensional clusters of rigid rods in air. *Physical Review Letters*, 96(20):204302, 2006.

[75] D. Torrent, D. Mayou, and J. Sánchez-Dehesa. Elastic analog of graphene: Dirac cones and edge states for flexural waves in thin plates. *Physical Review B*, 87(11):115143, 2013.

[76] D. Torrent and J. Sánchez-Dehesa. Effective parameters of clusters of cylinders embedded in a nonviscous fluid or gas. *Physical Review B*, 74(22):224305, 2006.

[77] D. Torrent and J. Sánchez-Dehesa. Acoustic metamaterials for new two-dimensional sonic devices. *New journal of Physics*, 9(9):323, 2007.

[78] F. Träger. *Springer handbook of lasers and optics*. Springer, 2007.

[79] O. Umnova, A. S. Elliott, and R. Venegas. Omnidirectional acoustic absorber with a porous core-theory and measurements. In *Proceedings of Meetings on Acoustics*, volume 19, page 065018. Acoustical Society of America, 2013.

[80] C. Wang and L. Rose. Plate-wave diffraction tomography for structural health monitoring. In *AIP Conference Proceedings*, volume 657, page 1615, 2003.

[81] H.-W. Wang and L.-W. Chen. A cylindrical optical black hole using graded index photonic crystals. *Journal of Applied Physics*, 109(10):103104, May 2011.

[82] T.-T. Wu, Y.-T. Chen, J.-H. Sun, S.-C. S. Lin, and T. J. Huang. Focusing of the lowest antisymmetric lamb wave in a gradient-index phononic crystal plate. *Applied Physics Letters*, 98(17):171911, 2011.

[83] T.-T. Wu, J.-C. Hsu, and J.-H. Sun. Phononic plate waves. *ieetuffc*, 58(10):2146–2161, October 2011.

[84] T.-T. Wu, Z.-G. Huang, T.-C. Tsai, and T.-C. Wu. Evidence of complete band gap and resonances in a plate with periodic stubbed surface. *Applied Physics Letters*, 93(11):111902, 2008.

[85] Y. Xiao, B. R. Mace, J. Wen, and X. Wen. Formation and coupling of band gaps in a locally resonant elastic system comprising a string with attached resonators. *Physics Letters A*, 375(12):1485 – 1491, 2011.

[86] Y. Xiao, J. Wen, and X. Wen. Flexural wave band gaps in locally resonant thin plates with periodically attached springmass resonators. *Journal of Physics D: Applied Physics*, 45(19):195401, 2012.

[87] D. Yu, Y. Liu, G. Wang, H. Zhao, and J. Qiu. Flexural vibration band gaps in timoshenko beams with locally resonant structures. *Journal of Applied Physics*, 100(12), 2006.

[88] D. Yu, Y. Liu, H. Zhao, G. Wang, and J. Qiu. Flexural vibration band gaps in euler-bernoulli beams with locally resonant structures with two degrees of freedom. *Physical Review B*, 73:064301, Feb 2006.

[89] J. Zhou, X. Cai, Z. Chang, and G. Hu. Experimental study on a broadband omnidirectional electromagnetic absorber. *Journal of Optics*, 13(8):085103, 2011.

[90] L. Zigoneanu, B.-I. Popa, and S. A. Cummer. Design and measurements of a broadband two-dimensional acoustic lens. *Physical Review B*, 84(2):024305, 2011.

Printed with LaTeX